

P69-280
CR 73337

VELLUMS

5034

NASA CR-73337
AVAILABLE TO THE PUBLIC

STUDY OF COLOR CENTER FORMATION IN WHITE
POWDER COMPOUNDS

by

Herman Levin
Vincent R. Honnold
Cedric C. Berggren

July 1969

Distribution of this report is provided in the interest of information exchange. Responsibility for the contents resides in the author or organization that prepared it.

Prepared under Contract No. NAS 2-5034 by
HUGHES AIRCRAFT COMPANY
Culver City, California

for

AMES RESEARCH CENTER
NATIONAL AERONAUTICAL AND SPACE ADMINISTRATION

FOREWORD

This report was prepared by the Hughes Aircraft Company, Research and Development Division, Aerospace Group for the National Aeronautics and Space Administration. The work was administered by the Ames Research Center. Mr. E.R. Streed was project monitor.

This summary report covers work accomplished during the period July 1, 1968 through May 31, 1969.

Mr. Herman Levin, Dr. Vincent R. Honnold, and Mr. Cedric C. Berggren were principal investigators. Mr. Paul M. Blair, Jr. was project engineer. The work was conducted within the Materials Technology Department under the direction of Mr. E.F. Smith. Dr. Ferdinand A. Kröger, Professor of Electrical Engineering, Materials Science, and Chemistry, University of Southern California, contributed as a consultant.

The authors wish to express their appreciation to Dr. A. L. Gentile, Dr. R. Kikuchi, and Dr. O.M. Stafsudd for helpful discussions during the work. They also gratefully acknowledge the machine computations carried out with the coloration model by Mr. W.M. Peffley.

ABSTRACT

A theoretical study has been performed of the mechanism by which wide band gap, crystalline, white oxide powders discolor when subjected to radiation typical of interplanetary space. Members selected from this group of solids, such as MgO and Al_2O_3 , should offer real potential as useful pigments in thermal control coatings for spacecraft. Formulation of a basis for selection constitutes the real problem, and this can be provided by a basic understanding of the kinetics of radiative coloration of white pigments in this potentially attractive group. Such kinetics have been studied in terms of the pertinent energy transfer mechanisms involved and then organized into a photochemical model. While necessarily tentative, this accomplished model is predictive of pigment reflectance attenuation induced in the proton-affected range by combined solar (wind) proton and photon radiation. Such initial predictive capability provides a necessary tool in arranging the proposed experimental program. The ultimate objective of such experimentation, controlled by iterative exchange of results with a continuously improved photochemical model, is the development of a superior pigment for spacecraft thermal control coatings.

CONTENTS

<u>Section</u>	<u>Page</u>
1.0 INTRODUCTION	1
2.0 DEVELOPMENT OF RADIATIVE COLORATION MODEL	3
2.1 Proton Ionization Effects in the Lattice. . .	4
2.2 Proton Displacement Effects in the Lattice. .	5
2.3 Annealing of Lattice Displacements . . .	7
2.3.1 Proton-Induced (Second Order) Annealing of Frenkel Defects . . .	7
2.3.2 Self-Annealing of Frenkel Defects . .	14
2.4 Photochemical Model . . .	23
2.4.1 Proton Stopping Region	23
2.4.2 UV Scattering Region	32
3.0 HIGH PURITY MATERIAL CONSIDERATIONS	35
3.1 Nature of Absorbing Color Center . . .	35
3.2 Radius r^*	35
3.3 Projected Proton Range R_p	38
4.0 EXPERIMENTAL STUDY PROGRAM	39
5.0 CONCLUSIONS .	41
6.0 REFERENCES	43
 <u>Appendices</u>	
A Review of Pertinent Space Environment .	45
B Charge State of Solar Wind Proton in Target Material	49
C Low Energy Proton Collision Theory	57
D Energy Barrier for Cation Vacancy Migration (ΔU_r) in an Otherwise Perfect Lattice	77
E Approximate Scattering Range of Solar UV Photons .	121

ILLUSTRATIONS

<u>Figure</u>		<u>Page</u>
1	Energy transfer from a 3000 eV proton as it is stopped in a MgO target	4
2	Cation displacement yield in oxides of interest as a function of initial proton energy	5
3	Comparison of cation and anion displacement yields in MgO as a function of initial proton energy	6
4	Cation displacement yield gradients generated by a 3000 eV proton in oxides of interest	6
5	Calculated probability that a Mg^{2+} knock-on in an MgO lattice will receive an energy $<T_1$ when struck by a proton of specified energy	12
6	Calculated probability that a metal knock-on ion (native to various lattices) will receive an energy $<T_1$ when struck by a proton from a Gaussian distribution in energies	13
7	Calculated probability that a metal knock-on interstitial ion (native to various lattices) will be separated from its parent vacancy a distance $<r_1$ when struck by a proton from a Gaussian distribution in energies	13
8	Variation in saddle-point relaxation energy in MgO as a function of displacement parameters ξ and η	16
9	Sketch of Frenkel defect in FCC lattice	20
10	Energy barrier for migration of a cation away from a nearby cation interstitial in a MgO lattice	22
11	Model predicted reflectance attenuation induced in the proton region of high purity MgO by simultaneous irradiation with 3 keV protons and the solar spectrum	31
12	Comparison of calculated and measured reflective attenuation in "reagent grade" MgO in the proton region by 10 keV protons	33
13	MgO crystal model (face centered cubic)	36
14	α - Al_2O_3 crystal model (rhombohedral)	37

1.0 INTRODUCTION

The work reported herein constitutes a detailed study of the mechanism by which a certain class of white powder compounds (of interest as pigments for spacecraft thermal control coatings) discolor upon irradiation with low energy protons and solar spectral emission. These radiation sources were selected as representative of the continuous flux in interplanetary space.

The study was restricted to wide band gap dielectric or insulator solids. This was done because (a) they appear more promising and because (b) one thus avoids the complexity introduced by necessary consideration of photo-decomposition kinetics (at room temperatures) when dealing with powders such as ZnO and TiO₂.

As reviewed herein, this theoretical effort is initiated by a study of defect generation in crystal lattices by low energy (1-3 keV) protons. Following the study of proton collision theory, a study of the probability for annealing processes to occur which would oppose proton generation of defects is undertaken. Annealing resulting from recombination of defect species by either (a) self-diffusion or (b) a second order, proton-induced process is investigated.

These defect generation and annealing kinetics are then integrated into a representative photochemical model. Some simplification of this model is made upon consideration in terms of MgO. Solutions of the model on this basis are presented.

Implications of the model in terms of material selection and experimental verification are also reviewed.

2.0 DEVELOPMENT OF RADIATIVE COLORATION MODEL

The environment to which this pigment coloration model is to be related is that existing in interplanetary space. Major features of the pertinent radiation are reviewed in Appendix A. The basic hazard is the solar wind consisting of a neutralized proton (p^+) flux of $\sim 2.5 \times 10^8$ p^+ /cm²-sec with an energy spectrum extending over limits of approximately 0.75 to 3.0 keV. The electron component is of the order of 1 eV. Additionally, one must also consider the UV component of the solar emission spectrum (0.2 to 0.4 μ wavelength).

Preliminary study of collision theory indicated that the keV range protons would likely charge equilibrate close to point of entry in a target to form, predominantly, the neutral species H^0 . Arguments relating to the $H^+ + e^- \rightleftharpoons H^0$ charge exchange process have been presented in Appendix B. As presently understood, low energy proton collision theory does not differentiate in terms of radiation effects induced by the two species. Despite this undefined dependence, some understanding of the charge state of the projectile may become important to the photochemical model which ultimately controls the coloration process.

Study of low energy proton collision theory reveals that two basic energy transfer mechanisms control the proton \rightarrow target interaction. In the area of interest, energy transfer as a result of inelastic collisions with target ions appears to be the dominant process by which the proton loses energy. A second process, in which energy transfer results from elastic collisions (i.e., nuclear stopping), appears to be more important in determining color center kinetics in high purity, dielectric oxides. The first process results in lattice ionization and the generation of charge carriers, e.g. electron (e^-) - hole (h^+) pairs. The second process results in lattice displacement with attendant generation of lattice vacancies, e.g. by creation of vacancy-interstitial pairs (Frenkel defects). These latter represent potential trapping sites which when populated form color centers. This pertinent collision theory is reviewed in detail, without consideration of channeling effects, in Appendix C.

Consideration of the displacement process on an ionic basis indicates a potential for annealing. This may be proton-induced and result from recombination of opposite defect species generated by separate, random proton collisions. Such annealing represents a second order process. An example, in the case of a Frenkel pair, would consist of the simultaneous recombination of the vacancy and the interstitial created by a given proton collision with their opposite species, respectively by, generated by prior uncorrelated events. Conventional self-annealing involves thermal motion of a single induced vacancy to within a capture radius of an interstitial. The latter process may be first or second order kinetics. In both cases, the energy barrier opposing migration can effectively determine the saturation density of these induced defect trapping sites. In order to demonstrate the source of this important parameter (i.e. in terms of material considerations), Appendix D is included. While generally applicable, specifically it is formulated for a case of interest, namely the evaluation of the energy barrier for migration of a cation vacancy in an otherwise perfect, face centered cubic crystal lattice.

Indications are that proton-induced displacement and ionization effects are dominant in that portion of a layer of pigment particles traversed by the proton. A study of the scattering of near-UV photons by typical pigment particles (see Appendix E) reveals that they penetrate this layer to a distance of the order of $100\mu(10^6\text{\AA})$. This may be compared with a proton penetration of the order of 100\AA . The radiation effects associated with 3.2 to ~ 6.5 eV solar UV photons incident on dielectric particles are likely to involve exciton generation, subsequent decomposition to free carriers, and trapping. Even though the density of such UV-induced effects is likely small, compared to proton-induced effects, the projected range affected is about four orders of magnitude greater. Consequently they warrant consideration in terms of their contribution to optical changes affecting solar absorption.

2.1 Proton Ionization Effects in the Lattice

Equations developed in Appendix C permit one to compute the partition of energy, transferred from a moving proton to a crystal lattice, between ionization and nuclear processes. Figure 1 illustrates the result of such a computation for a case of interest, a 3000 eV proton incident on MgO. The computation is made without regard to channeling effects. It will be observed that at the end of the particle track, $\sim 800\text{\AA}$, about 83% of its energy resulted in ionization effects. For a material such as MgO (band gap energy $E_g \approx 10$ eV), the ionization yield of such a collision is approximately 125 ($= 2500/(2 \times 10)$) $e^- - h^+$ pairs.

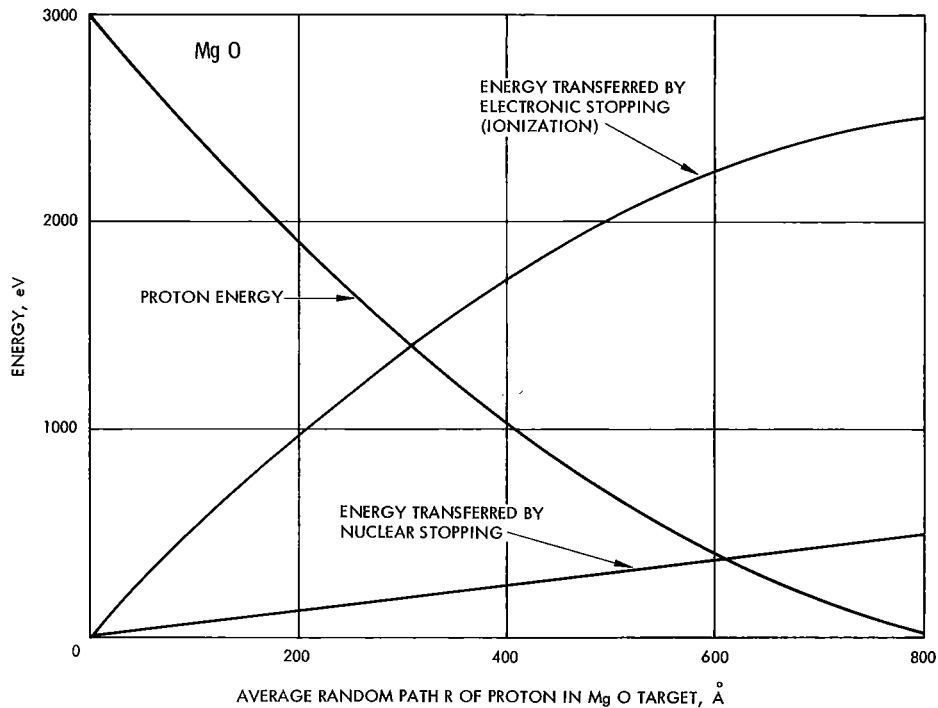


Figure 1. Energy transfer from a 3000 eV proton as it is stopped in a MgO target.

Note also that while the energy transfer gradient (slope of curve) for ionization drops off continuously along the random path R (track) the energy transfer gradient as a result of nuclear stopping is essentially constant. This results from the assumption that the nuclear stopping cross section S_e is independent of energy over the limits of interest (say 150-3000 eV).

2.2 Proton Displacement Effects in the Lattice

The displacement yields (number of displacements per proton) as a function of proton energy and target material is computed from equations (C29) and (C30) presented in Appendix C. A comparison of various targets in Figure 2 demonstrates that the cation displacement yield increases with decreasing cation mass, as would be anticipated. Also expected is the non-linear increase in yield with increase in energy for a given material. This latter indicates that, with increasing proton energy, nuclear stopping becomes less significant.

In a real crystalline compound, e.g. A_jB_m , there is a strong likelihood of the proton colliding alternately with cation and anion members of the lattice. In those cases where the anion mass is less than the cation mass, e.g. MgO, anion displacement can continue even when the protons' energy has dropped to a level below which cation displacement cannot occur. Below such an energy level, energy transfer to the cation can only induce "thermal" effects. There is a still lower energy limit below which the proton cannot effect anion displacement. Below this energy level, the residual proton energy is dissipated to both cation and anion as a "thermal" effect. A comparison of cation (n_A) and anion (n_B) displacement yields in MgO is presented in Figure 3 as a function of proton energy. As explained above, $n_B > n_A$ where mass $B < \text{mass } A$.

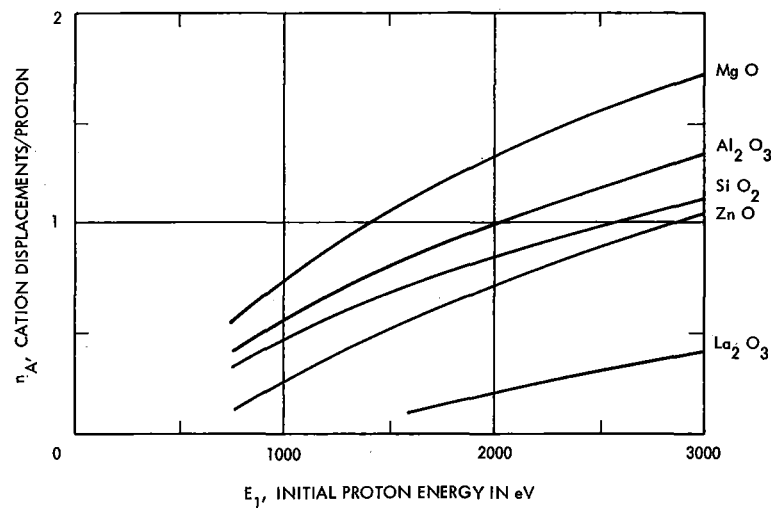


Figure 2. Cation displacement yield in oxides of interest as a function of initial proton energy.

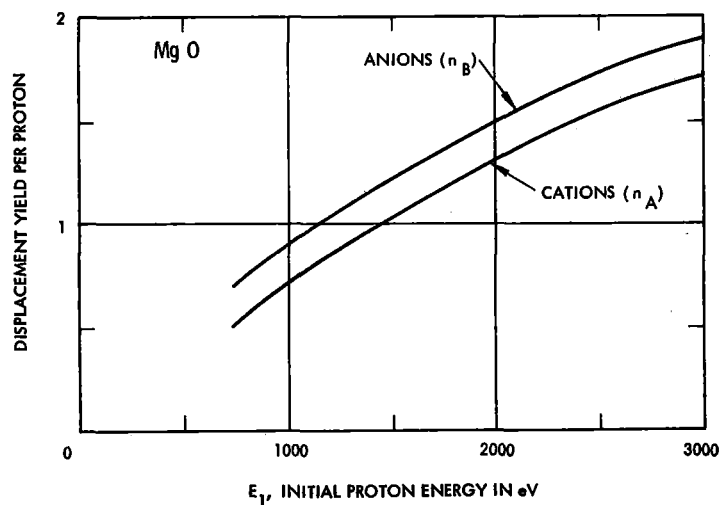


Figure 3. Comparison of cation and anion displacement yields in MgO as a function of initial proton energy.

In terms of a coloration model one needs to know whether the color center rate equations must be expressed as being dependent on projected range. For this reason the cation displacement yield gradients generated by a 3000 eV proton in various oxides were computed as shown in Figure 4.

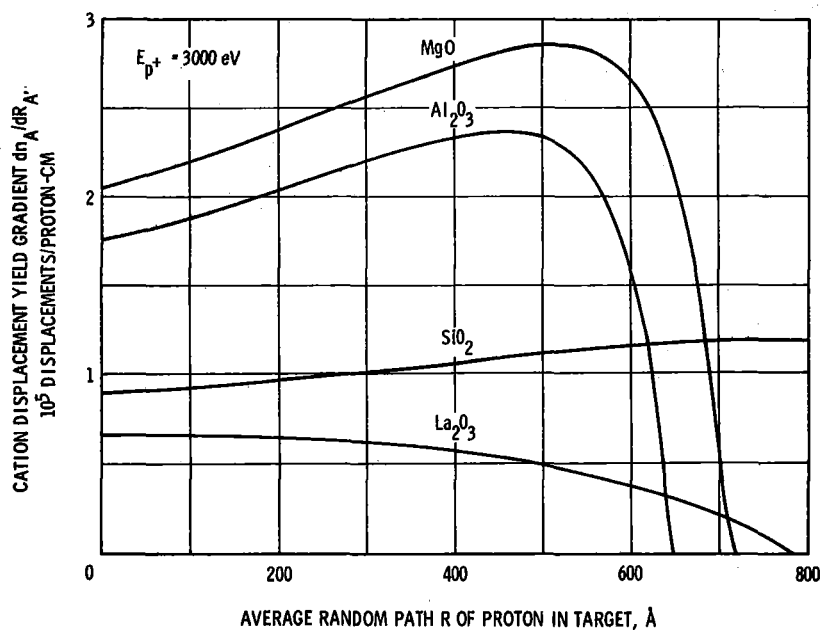


Figure 4. Cation displacement yield gradients generated by a 3000 eV proton in oxides of interest.

Even though presented on the basis of total path R rather than projected range R_p , there is a reasonable indication that the cation displacement yield is fairly uniform over the projected range. Thus displacement yields need not be considered range-dependent in the color center kinetics. Note from Appendix C (Table C1) that R_p is an order of one-fourth R for a proton of initial energy = 3000 eV.

2.3 Annealing of Lattice Displacements

Earlier consideration of low energy proton collision kinetics in ionic lattices revealed that a significant portion of the protons' energy is transferred to a crystal lattice via an elastic collision mechanism. This results in displacement of lattice ions from normal sites to metastable interstitial positions with a yield of the order of one displacement per proton. A given displaced ion thus comes to rest at an interstitial position a radial distance r away from its normal site. This pair, consisting of an interstitial (say M_i'') and its parent vacancy (say V_M''), is termed a Frenkel pair.

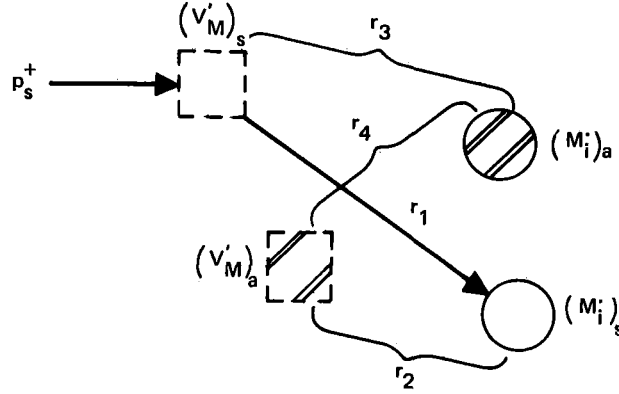
Charged particle collision studies further indicated (without consideration of channeling) that the projected range over which dissipation of the protons' energy is complete is an order of 10^{-6} cm for materials of interest. This energy loss is also indicated to be reasonably uniform over the projected ranges. These facts, when considered together in terms of a typical space flux of 2.5×10^8 solar wind protons/cm²-sec, indicate the generation in the surface of $\sim 10^{21}$ Frenkel defects per cm³ per year without consideration of annealing processes. Such defect levels would represent material decomposition. Further, this order of defect density makes insignificant the contributions to intrinsic defect levels (e.g., the density of isolated cation vacancies) introduced into the p^+ range by virtue of any reasonable thermal or mechanical history or the presence of selected, substitutional impurities.

Thus it is imperative to investigate the probability for annealing (both self- and proton-induced) of these proton-induced Frenkel pairs, for example $V_M'' - M_i''$.

2.3.1 Proton-Induced (Second Order) Annealing of Frenkel Defects

2.3.1.1 Second Order Annealing Model

Based on the concept of forward scattering in an ionic lattice, the pair density in a crystal MX containing a stable vacancy $(V_M)_a$ - interstitial $(M_i)_{1a}$ pair generated by p^+ collision event a will double if, after a subsequent, unrelated, random p^+ event s resulting in a second pair $(V_M)_s - (M_i)_s$, the separations between $(V_M)_a - (M_i)_s$, $(V_M)_s - (M_i)_s$, and $(V_M)_s - (M_i)_{1a}$ in all cases exceeds the radius of certain recombination r^* . This concept is illustrated as follows:



The above stable defect system ($r_4 > r^*$) experiences a net gain of one pair after event p_s^+ if $r_1, r_2, r_3 > r^*$.

The probability for initial pair separation (i.e., upon impact) controls r_1 and r_4 and may be estimated from Holmes' displacement theory.¹ In terms of a $(V_M)_a - (M_i)_a$ separation $> r^*$, this probability is labeled $\rho(r > r^*)$ or ρ for shorthand.

The probability for recombination between allowed, random pair members, e.g., $(V_M)_a - (M_i)_s$, may be expressed as the ratio of the volume associated with certain recombination to that existing "average" volume associated with a given defect. This probability may be labeled P . It will be observed that once separated by $r_1 > r^*$ (i.e., prevented from self-recombination), each member of the new pair above, $(V_M)_s$ and $(M_i)_s$, is independently able to recombine with an existing opposite species. This gives rise to $P(V_s \rightarrow M_a)$ and $P(M_s \leftarrow V_b)$, where \underline{a} and \underline{b} represent any random existing species and the arrows denote a vacancy jumping toward an interstitial assumed to be stationary. By definition then:

$$P(V_s \rightarrow M_a) = P(M_s \leftarrow V_b) \equiv P \equiv \frac{(4/3)\pi r^{*3}}{1/N} \quad (1)$$

where:

$$N = \text{pair density} \approx \text{defect density, no./cm}^3$$

$$1/N = \text{crystal vol. (cm}^3\text{) associated with each defect}$$

$$(4/3)\pi r^{*3} = \text{max. vol. associated with certain recombination}$$

It is evident that recombination of a single pair results in no net defect density change. Simultaneous recombination (with probability P^2) of both members of a single defect event is required for annealing.

Based on the above considerations, a rate expression for N is as follows:

$$\frac{dN}{dt} = \rho(n\phi/R_p) - \left[\rho(n\phi/R_p)\right](P)(P) \quad (2)$$

where:

$n' = n\phi/R_p$ = Frenkel pair generation rate, no./cm³-sec
(neglecting secondary effects)

n = cation or anion displacement yield n_A or n_B , displacements/proton

ϕ = proton flux, p⁺/cm²-sec

R_p = projected range of proton, cm

The factor ρ insures that only displacements greater than r^* are counted.

Substituting from (1) into (2) and rearranging yields:

$$\begin{aligned} \frac{dN}{dt} &= \rho(n\phi/R_p) \left\{ 1 - \left[(4/3) \pi r^{*3} N \right]^2 \right\} \\ &= \rho n' (1 - CN^2) \end{aligned} \quad (3)$$

where:

$$C = \left[(4/3) \pi r^{*3} \right]^2$$

The resulting rate expression, equation (3), is observed to be of second order. Rearrangement facilitates its solution as follows:

$$\begin{aligned} \frac{(1/C) dN}{1/C - N^2} &= \rho n' dt \\ \frac{1}{C} \int_{N(o)}^{N(t)} \frac{dN}{1/C - N^2} &= \rho n' \int_0^t dt \\ \frac{1}{C} \left[\frac{1}{C^{-1/2}} \tanh^{-1} \left(\frac{N}{C^{-1/2}} \right) \right]_{N(o)}^{N(t)} &= \rho n' t \end{aligned}$$

$$\begin{aligned}
\tanh^{-1} \left[C^{1/2} N(t) \right] - \tanh^{-1} \left[C^{1/2} N(o) \right] &= \left(\rho n' C^{1/2} \right) t = t/\tau \\
C^{1/2} N(t) &= \tanh \left\{ t/\tau + \tanh^{-1} \left[C^{1/2} N(o) \right] \right\} \\
C^{1/2} N(t) &= \frac{\tanh(t/\tau) + C^{1/2} N(o)}{1 + \tanh(t/\tau) C^{1/2} N(o)} \\
N(t) &= \frac{C^{-1/2} \tanh(t/\tau) + N(o)}{1 + C^{1/2} N(o) \tanh(t/\tau)} \quad (4)
\end{aligned}$$

where:

$$\tau = \text{time constant} = (\rho n' C^{1/2})^{-1}$$

Note that the expression for $\tanh(t/\tau)$ is:

$$\tanh(t/\tau) = \frac{\exp(t/\tau) - \exp(-t/\tau)}{\exp(t/\tau) + \exp(-t/\tau)} \quad (5)$$

Thus at $t = \infty$ (approximated by $t \gg \tau$) from equation (5) we see that $\tanh(t/\tau) = 1$. Therefore from (4), $N(\infty) = C^{-1/2}$. Similarly the pair density $N(\tau)$ may be obtained by evaluating $\tanh(t/\tau)$ at $t = \tau$ and substituting in (4) as follows:

$$\left[\tanh(t/\tau) \right]_{t=\tau} = \frac{e - 1/e}{e + 1/e} = \frac{2.718 - 0.368}{2.718 + 0.368} = 0.76 \quad (6)$$

$$\begin{aligned}
\therefore N(\tau) &= \frac{0.76 C^{-1/2} + N(o)}{1 + 0.76 C^{1/2} N(o)} \\
&\approx 0.76 C^{-1/2} \approx 0.76 N(\infty) \quad (7)
\end{aligned}$$

The pair density at a time equal the time constant has thus attained 76 percent of its steady state value $N(\infty)$ when $N(o)$ values are relatively small.

Examination of equations (3) or (4) reveals an increasing rate of approach to $N(\infty)$ with increasing proton flux ϕ of a given energy level. They further indicate that the time-dependent Frenkel pair density created by low energy proton incidence may be expressed as a second order rate equation in terms of a pair generation rate n' ($= n\phi/R_p$ in primary pairs/cm²-sec) and certain probabilities for initial pair separation and for recombination between allowed random pair members.

2.3.1.2 Probability For Initial Pair Separation

The calculation of the probability that a given proton (either monoenergetic or with a defined probability of energy distribution) upon collision with a lattice cation will knock the cation (primary knock-on ion) a distance $>r^*$ away from the parent lattice site is based on collision theory presented in Appendix C. It proceeds in two steps:

- (a) First calculate the ratio $\Omega(T < T_1)$ of the number of knock-on ions receiving energy $< T_1$ from a proton of energy E_1 , $n(T < T_1, E_1)$, to the total number knock-ons which a proton of energy E_1 can generate, $n(E_1)$. This ratio represents the probability that a knock-on will possess an energy $< T_1$ when struck by a proton of energy E_1 .
- (b) Holmes presents a general correlation of the average vector range (in this case equivalent to $M_i'' - V_M''$ separation) of a knock-on ion moving in its own lattice with initial energy T_1' . (Note: His symbol for T_1' is E . Further $T_1' = T_1 - E_D$; in other words the initial energy of the knock-on is equal to the upper limit of transferred energy T_1 less the energy required to effect ion displacement E_D , ≈ 25 eV.)

Thus the probability that a knock-on will receive energy $< T_1$ from a proton of energy E_1 can be equated through Holmes' work to a corresponding probability that the separation between the knock-on interstitial (M_i'') and its parent vacancy (V_M'') will be some value $< r_1$.

The probability that a primary knock-on will be transferred an energy $< T_1$ by a proton of initial energy E_1 may be expressed as follows:

$$\Omega(T < T_1, E_1) = \frac{n(T < T_1, E_1)}{n(E_1)} \quad (8)$$

This expression may be modified to include the more general case when the proton has a probable distribution in initial energy $\Psi(E)$ as follows:

$$\Omega \left[T < T_1, \Psi(E) \right] = \frac{\int d\Psi(E) \cdot n(T < T_1)}{\int d\Psi(E) \cdot n} \quad (9)$$

Using relationships similar to those developed in Appendix C, solutions for both the case of a knock-on generated by monoenergetic proton collision and the case where proton energies are distributed have been obtained. These solutions are presented for MgO in Figure 5. Within the context of the precision of this effort, it is noted that the probability Ω is not greatly sensitive to the method of specification of initial proton energy within the limited solar wind energy range. In Figure 6 probability values for additional oxide compounds are presented, all based on the same, arbitrary, Gaussian, proton energy distribution (peak energy = 1.75 keV, limits of 0.75 to 3 keV) indicated in Figure 5.

The calculated probabilities Ω have been converted into calculated probabilities for vacancy-interstitial separation, $\rho(r < r_1')$, by means of Holmes' correlation and presented in Figure 7. Note that the Holmes' correlation relates to "equal mass cases," i.e., those cases where a single species of knock-on atom moves in its own lattice. The conversion of probabilities has been made with this tacit assumption refined by the further assumption that the metal ion moves in its own lattice, modified so as to possess the ionic density of an actual designated compound. For given values of r_1 (e.g. r^*), the probability that the vacancy-interstitial separation is greater than r^* is given by: $\rho(r > r^*) = 1 - \rho(r < r^*)$.

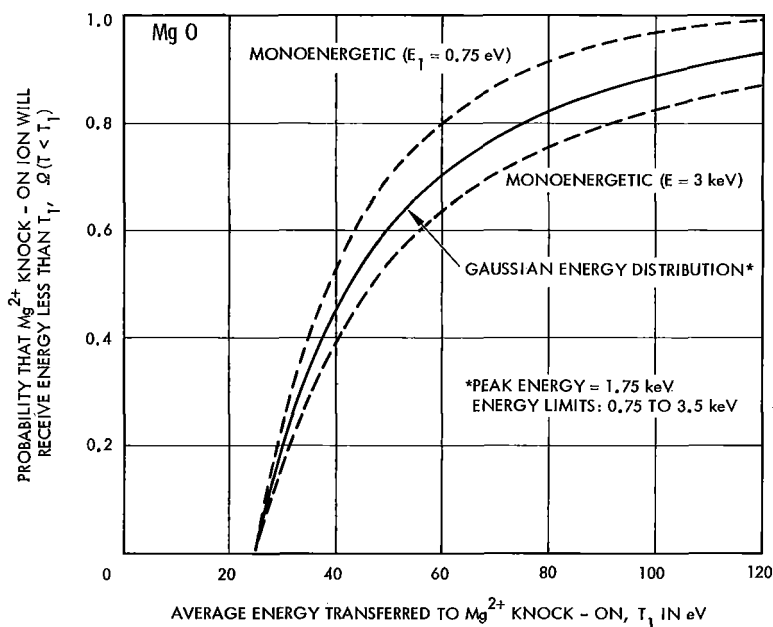


Figure 5. Calculated probability that a Mg²⁺ knock-on in an MgO lattice will receive an energy $< T_1$ when struck by a proton of specified energy.

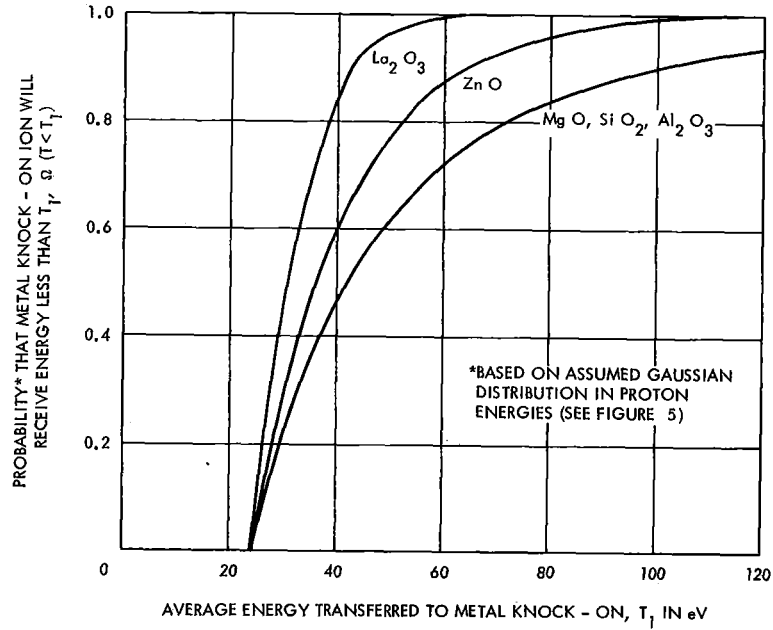


Figure 6. Calculated probability that a metal knock-on ion (native to various lattices) will receive an energy $< T_1$ when struck by a proton from a Gaussian distribution in energies.

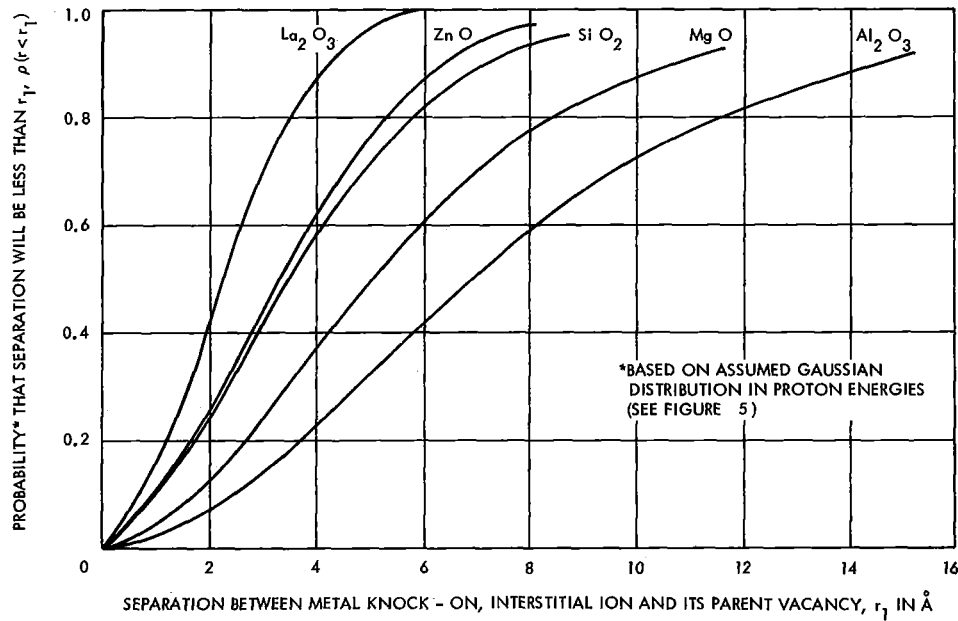


Figure 7. Calculated probability that a metal knock-on, interstitial ion (native to various lattices) will be separated from its parent vacancy a distance $< r_1$ when struck by a proton from a Gaussian distribution in energies.

2.3.2 Self-Annealing of Frenkel Defects

The maximum volume associated with certain recombination between $(V_M'')_a$ and $(M_i'')_a$ resulting from p^+ collision a is $4/3 \pi r^3$. Thus r^* is termed that radial separation between $(V_M'')_a$ and $(M_i'')_a$ below which self-annealing is certain in a time of interest (e.g., a year). At separations $> r^*$, second order annealing is possible and is accounted for in equation (4).

Self-annealing is thus controlled by the value determined for r^* . This r^* determination has proven to be a difficult task even on the basis of certain simplifying assumptions. These assumptions, while limiting the rigorosity of the solution, certainly do not appear restrictive in terms of usefulness of the solution to the problem at hand. For example, it is assumed that in a metal oxide (1) the metal ion interstitial (M_i'') -vacancy (V_M'') pair is preferentially generated and further that (2) $V_M'' - M_i''$ self-recombination occurs by V_M'' migration through the lattice directly toward an essentially stationary M_i'' . At some small separation $r = r^*$, it is thought that the energy barrier to cation (V_M'') migration (characteristic of large separation) will be sufficiently overcome by $V_M'' - M_i''$ interactions in the lattice so that thermal motion (at room temperature) will offer high probability that a jump toward M_i'' can occur within a year. Any required, subsequent lattice jumps to effect final recombination would then be expected to occur in times small compared to a year.

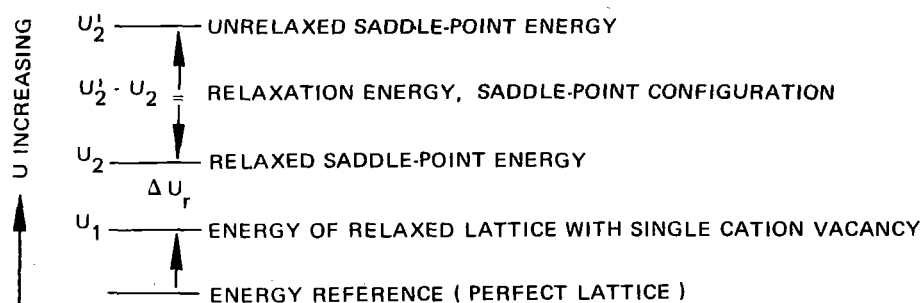
2.3.2.1 Energy Barrier for Cation Vacancy Migration in an Otherwise Perfect Lattice

The first step in this task involves the theoretical calculation of the energy barrier for vacancy migration ΔU_r (cation) in an otherwise perfect lattice. This basis approximates the real case when r is very large. Computation of ΔU_r requires evaluation of the lattice potential (or lattice energy) along certain paths between normal lattice positions. Although imposing some limitation on ultimate usefulness, the complexity of the calculation dictated selection of one of the simplest lattices as a basis for initial calculations, namely the face centered cubic lattice. In this lattice, separations between adjacent cation and anion is termed r_0 and the pertinent cation migration path is a diagonal one from a 0, 0, 0 to a 1, 1, 0 position and passing through the saddle-point approximated by position 1/2, 1/2, 0. Schematically, this is shown in Figure D2 (Appendix D). Cation movement is indicated as occurring from normal lattice site b (0, 0, 0) to vacancy a (1, 1, 0), with the cation shown in the saddle-point position (1/2, 1/2, 0). Cation vacancy migration, of course, occurs in the opposite direction.

Note that migration of the lattice cation is based on an otherwise perfect lattice containing a cation vacancy. As the lattice cation moves to the saddle-point configuration, critical to the ΔU_r value, three defect states result, namely cation vacancies v_a and v_b and the lattice cation at the saddle-point. There are ten nearest neighbor (n.n.) anions to these three defects. The two n.n. anions to the saddle cation undergo the critical displacement $\sqrt{2}\xi r_0$ upon lattice relaxation about the saddle-point configuration. The remaining eight anions are located n.n. to the two vacancies and undergo lesser displacement ηr_0 upon relaxation. The net energy release ($U_2' - U_2$), primarily resulting from reduced non-Coulombic ionic interactions, which accompanies this relaxation to displaced positions by all lattice ions is dominated by the displacement of these ten nearest neighbor anions.

By means of solutions given in Appendix D one may demonstrate the variation in relaxation energy ($U_2' - U_2$) in terms of the dimensionless displacement parameters ξ and η . Such variation is presented in Figure 8 for the case of MgO, a face centered cubic lattice. Note that this relaxation energy represents the sum of Coulombic and non-Coulombic interaction energies. Since η is the least sensitive of the two parameters, interaction energies are computed for a selected η value while the value of ξ is varied. The maximum decrease in energy ($U_2' - U_2$) locates the equilibrium displacement positions. It happens that the value indicated (-64.396 eV) results from a process of successive trial-and-error selection of η values and calculation of corresponding ξ values until a maximum decrease, indicative of equilibrium, was obtained.

The value of ΔU_r for a vacancy in an otherwise perfect lattice equals the relaxed saddle-point energy less the work done in creating this single vacancy. An energy level schematic demonstrates this relationship as follows:



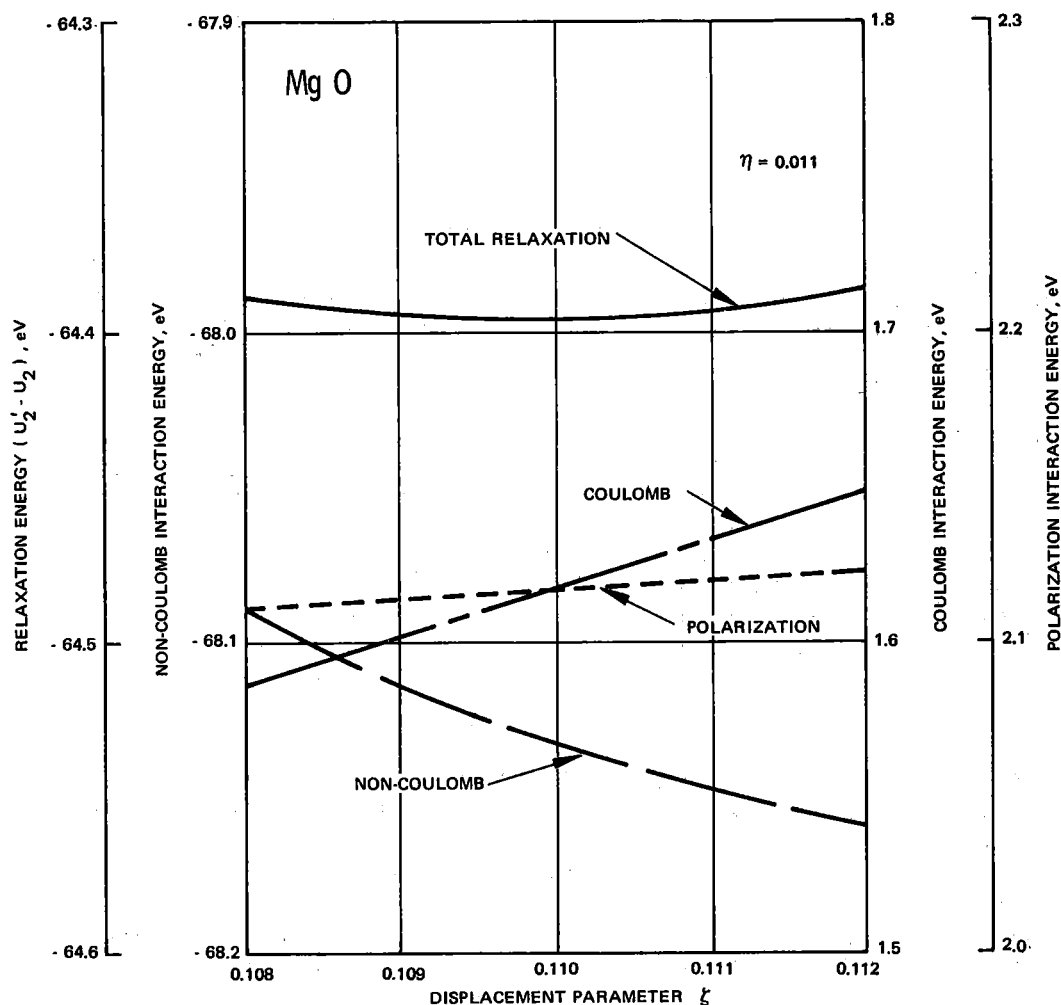


Figure 8. Variation in saddle-point relaxation energy in MgO as a function of displacement parameters ξ and η

Thus, in a lattice with energy U_1 , as the cation migrates from position 0, 0, 0 to 1/2, 1/2, 0 the lattice energy would rise sharply were it not for relaxation of the nearest neighbor ions, especially the two adjacent to the saddle ion. Upon relaxation, energy $U_2' - U_2$ is released and the lattice energy drops significantly to the value indicated at the relaxed saddle-point. The energy barrier for cation (or cation vacancy) migration ΔU_r is thus observed to be the difference in lattice energy levels existing in the relaxed saddle-point configuration U_2 and in the relaxed single cation vacancy configuration U_1 . Indicative of the importance of this relaxation energy is the fact that typically it is an order of magnitude greater than ΔU_r .

The results of a calculation of ΔU_r for the case of MgO are presented in Table 1, both with and without consideration of Van der Waal interactions. These values were computed using procedures described in Appendix D.

TABLE 1. EFFECT OF VAN DER WAAL INTERACTIONS ON CALCULATED ΔU_r (CATION) VALUE FOR MgO

	<u>MgO</u>	
	<u>Without</u> <u>Van der Waal</u>	<u>With</u> <u>Van der Waal</u>
Polarization displacement of ions nearest neighbor to <u>a</u> :		
Cation vacancy, νr_o	0.035	0.035 (est)
Saddle-Point Configuration, ξr_o	0.11	0.11 (est)
ηr_o	0.011	0.011 (est)
Unrelaxed saddle-point energy U_2' , eV	90.070	90.328
Saddle-point relaxation energy change $U_2' - U_2$, eV	-64.396	-64.396
$U_2 \left[= U_2' - (U_2' - U_2) \right]$ in eV	25.674	25.932
Relaxed lattice with single cation		
vacancy (U_1), eV	22.211	22.583
$\Delta U_r(\text{cation}) = U_2 - U_1$ in eV	3.463	3.349

The effect of Van der Waal's contributions to the lattice energy at various defect configurations is seen to be small, thus resulting in a small net effect on ΔU_r (cation). The Van der Waal energy interaction terms are Coulombic and are generally expressed as follows:

$$U_{AB} = -\frac{C_{AB}}{r^6} - \frac{D_{AB}}{r^8} \quad (10)$$

$$U_{BB} = -\frac{C_{BB}}{r^6} - \frac{D_{BB}}{r^8} \quad (11)$$

$$U_{AA} = -\frac{C_{AA}}{r^6} - \frac{D_{AA}}{r^8} \quad (12)$$

where, for the case of MgO, consider A to represent the Mg^{2+} and B to represent the O^{2-} . Constants C_{AB} , C_{AA} , and C_{BB} are applicable to interactions between $Mg^{2+} - O^{2-}$, $Mg^{2+} - Mg^{2+}$, and $O^{2-} - O^{2-}$ respectively. The D constants are similarly designated. As might be expected from the fact that Van der Waal forces are attractive between the nuclear charge of one ion and the valence charge of a neighbor, the largest values of the constants are C_{AA} and D_{AA} , representing the interaction between both of the heavier species Mg^{2+} . Also, it is obvious that these interactions (varying as $1/r^6$ and $1/r^8$) drop off very rapidly with separation r between two given ions.

Referring to the cation saddle-point configuration shown in Figure D2 in Appendix D, it is seen that only the 10-nearest neighbor anions (say O^{2-}) undergo major displacement upon relaxation. Since it is so sensitive to the separation r , the contribution of the Van der Waal terms is thus minimized by the fact that the interactions at closest separation are largely between Mg^{2+} and O^{2-} .

Please note that for the case of an anion saddle-point configuration, the n.n. displaced ions would be cations (say Mg^{2+}). In such a case, the $Mg^{2+} - Mg^{2+}$ interaction terms are dominant and have been calculated to be more than an order of magnitude greater than the $Mg^{2+} - O^{2-}$ or $O^{2-} - O^{2-}$ interactions. Thus Van der Waal interactions would, in this case, have to be considered integrally with the other Coulombic and non-Coulombic interactions in order to calculate lattice relaxation about the saddle-point by the procedure of maximizing the decrease in relaxation energy.

Since Van der Waal contributions are fortuitously small in the case of the cation vacancy migration, these contributions were calculated independently and added to the values in the left hand column of Table 1 in order to obtain those given in the right hand column. Similar reasoning indicates that displacement values may be estimated as unchanged by Van der Waal interactions for the case of cation vacancy migration.

The above computation discloses two major points as follows:

- a. The calculated value of ΔU_r (cation) = 3.3 eV is close to the experimentally obtained value ² of 3.4 eV in the region of intrinsic self-diffusion (i. e. for MgO).

- b. Lattice relaxation displacements are much smaller than anticipated based on comments by Fletcher and Brown,³ being only 0.11 r_0 in the case of the two anions which are nearest neighbors to the saddle-point ion.

2.3.2.2 Energy Barrier for Cation Migration in Close Proximity to an Interstitial Ion

A second step is involved in the study of self-annealing of Frenkel pairs. This consists of evaluating ΔU_r (cation) as the cation moves in close proximity to the stationary interstitial. Summation of explicit and continuum interaction energy terms for this lattice defect configuration has proven too complex to consider within the scope of this work. As an alternative procedure, V_M'' is considered to jump directly toward the oppositely charged $M_i^{\bullet\bullet}$ against $\Delta U_{r''}$ (even when r is small) but assisted by the energy of interaction between V_M'' and $M_i^{\bullet\bullet}$, $q_V \cdot q_M / (\kappa r) = q^2 / (\kappa r)$. Justification for such a procedure stems from the fact that, since lattice distortion was found to be much smaller than anticipated, it seems reasonable that one is thus permitted to uncouple the two members of the approaching defect pair ($V_M'' - M_i^{\bullet\bullet}$) in terms of their overlap repulsion interaction. Their interaction may therefore be treated on the basis of a Coulombic interaction only between two charges, q_V and q_M (where $q = q_M = q_V$), with polarization accounted for by insertion of κ . That is, the Coulombic interaction is treated on a continuum basis. Precedent for such a continuum treatment is found in computations of cation vacancy-anion vacancy recombination in a face centered cubic (conceptually similar to $V_M'' - M_i^{\bullet\bullet}$ recombination) reported by Seitz⁴ and by Reitz and Gammel,⁵ where the cation vacancy jumps toward the stationary anion vacancy.

Consider the face centered cubic lattice in Figure 9 with divalent cations M^{2+} , only a few of which are shown. A reference cation M_{ℓ}^{2+} is shown at a lattice site (000). A cation vacancy \square generated by a previous proton collision has moved as close as position (110) with respect to an interstitial ion M_i^{2+} shown at one of three alternative interstitial positions, $(-1/2, -1/2, 0)$, $(-3/2, -1/2, 0)$ or $(-3/2, -3/2, 0)$. Note that, when the reference cation M_{ℓ}^{2+} jumps from (000) into the cation vacancy at (110), this vacancy appears to migrate to a new position at (000). At the latter position $V_M'' - M_i^{\bullet\bullet}$ recombination is instantaneous. Additionally, it is apparent that there is an interaction energy between M_i^{2+} and M_{ℓ}^{2+} causing the latter to be pushed in the 110 direction. This interaction energy, as discussed previously, may be calculated for the specific case of MgO as follows:

$$U = \frac{q^2}{\kappa r} \quad (13)$$

By using c g s units and letting r have integral values j of lattice jumps in the 110 direction, i. e., $r = j \sqrt{2} r_0$, equation (13) converts to the following:

Case 2: M_i^{2+} at $(-3/2, -1/2, 0)$

$$\Delta U = \frac{1.98}{\sqrt{5}/2} - \frac{1.98}{\sqrt{5}/2} = 0.52 \text{ eV} \quad (16)$$

Case 3: M_i^{2+} at $(-3/2, -3/2, 0)$

$$\Delta U = \frac{1.98}{3/2} - \frac{1.98}{2} = 0.33 \text{ eV} \quad (17)$$

In effect these values in equations (15), (16), and (17) represent energy available to M_ℓ^{2+} to overcome the energy barrier at the saddle position $(1/2, 1/2, 0)$ taken = 3.3 eV for MgO. For Case 1, this energy push is still 1.32 eV less $(3.3 - 1.98)$ than the barrier height. The time constant τ for thermal motion to overcome this deficiency at room temperature (say 300°K) is estimated as follows:

$$1/\tau = \nu = \nu_o \exp [-1.32/(kT)] = (10^{13})(1/1.3 \times 10^{22})$$

$$\tau = 1.3 \times 10^9 \text{ sec} \gg 1 \text{ year} \quad (18)$$

Thus when M_ℓ^{2+} is nearest neighbor to M_i^{2+} ($r = r_o \sqrt{2}/2$), the former is still unable to overcome, in any reasonable period of time, the energy barrier for migration. As a consequence, the cation vacancy at (110) may not (appear to) move closer, i.e., to (000), and so effect recombination with the interstitial M_i^{2+} . It is evident that greater separation between M_ℓ^{2+} and M_i^{2+} makes migration of M_ℓ^{2+} even less probable.

Based on the analysis above, recombination between M_i^{2+} and the vacancy is not probable when $r \geq 3/2 \sqrt{2} r_o$. This then represents r^* separation for the MgO face centered cubic lattice. Estimating the limiting or steady state volume per Frenkel pair on this basis one obtains:

$$\frac{4}{3} \pi r^{*3} = \frac{4}{3} \pi \left(\frac{3}{2} \sqrt{2} r_o \right)^3 = \frac{4}{3} \pi \left(\frac{3}{2} \sqrt{2} \times 2.1 \times 10^{-8} \text{ cm} \right)^3$$

$$= 3.7 \times 10^{-22} \text{ cm}^3 / \text{pair in MgO}$$

$$\frac{1}{3.7 \times 10^{-22}} = 2.7 \times 10^{21} \text{ Frenkel pairs/cm}^3 \text{ of MgO} \quad (19)$$

Thus it appears that self-annealing of displacements is not significant in reducing radiation damage in dielectric oxides. Further, in those cases where damage is restricted to very small depths (e. g., with low energy protons) Frenkel defect densities associated with major decomposition (e. g., $\sim 5\%$ in the case of MgO) are expected at steady state.

The separation r^* has thus been defined for the case of a cation vacancy migrating against an energy barrier (activation energy) U_r directly toward a stationary interstitial cation. In reality of course, migration of a cation vacancy only reflects the actual migration of a lattice cation. Estimates of interaction and migration barrier energies involved are illustrated in Figure 10 for the case of MgO. Curve A represents the interaction energy (on a continuum basis) between a lattice cation moving in a 1, 1, 0 direction and a fixed interstitial cation at $-1/2, -1/2, 0$ (see Figure 9 also). Curve B illustrates the energy barrier for migration of a lattice cation with no interstitial cation present. Curve C indicates the Coulomb repulsive effect of a nearby interstitial cation on ΔU_r . Such an effect is seen to be significant only at close separation, reducing ΔU_r from 3.3 eV to ~ 1.3 eV only when $r = \sqrt{2} r_0$ (as was shown earlier). As shown, Curve A must also represent the locus of the minima in Curve C.

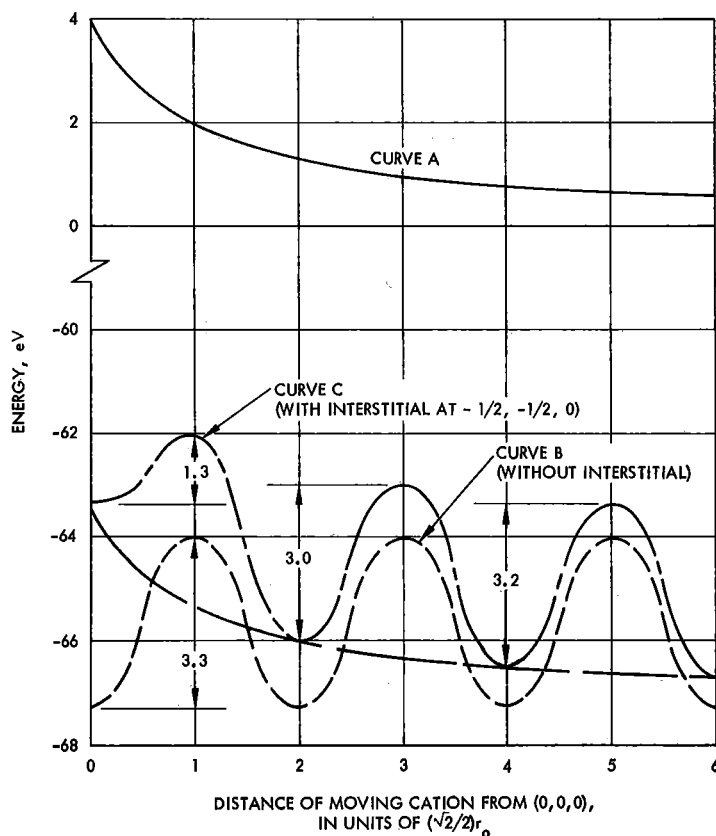


Figure 10. Energy barrier for migration of a cation away from a nearby cation interstitial in a MgO lattice.

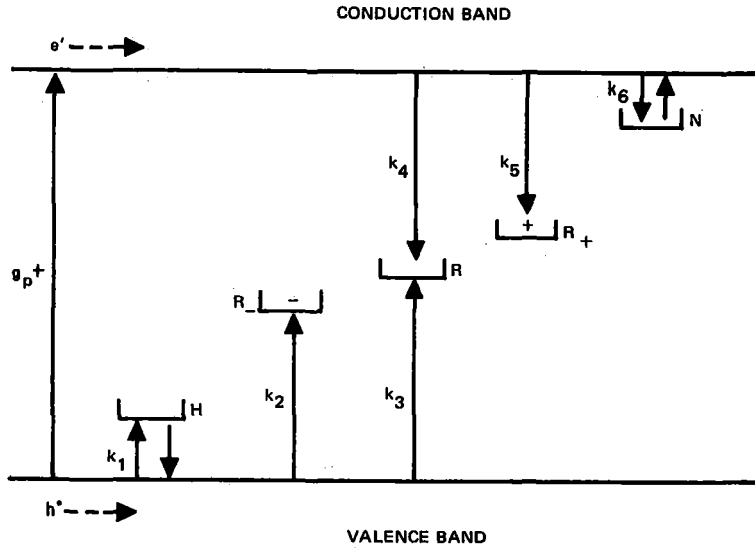
2.4 Photochemical Model

Earlier it was reported that the projected ranges of solar wind protons (1-3 keV energies) were expected to be an order of 10^2 Å in inorganic pigment powders of interest. Studies of light scattering by small "particles" indicate that the scattering range of a 0.3μ UV photon in a dense medium containing typically $\sim 1\mu$ diameter scatters (particles or pores) is an order of $10^2\mu$ ($= 10^6$ Å). It is evident then that proton energy absorption is largely concentrated at the periphery of the pigment particle. Lattice vacancy generation, an order of one vacancy/ p^+ collision, is accompanied by energy transfer via ionization in this restricted region yielding an order of 40 to 125 e^-h^+ pairs. The generation rate of both traps and carriers in this proton range is so great as to permit UV-induced photochemical processes to be ignored. However, the UV scattering depth extends about four orders of magnitude beyond the projected p^+ range and includes something of the order of 10^2 particle layers. Thus even though exciton-complex defect interactions induced by UV may result in low densities of solar resonant centers, the optical path affected by UV is large enough to warrant consideration in terms of ultimate coloration kinetics. Thus the proton region will be considered separately from the UV region, and in effect the final model will contain a step function in projected depth.

2.4.1 Proton Stopping Region

2.4.1.1 Model Theory

The photochemical kinetics in the proton stopping region may be considered initially in terms of a five level band model, including: (a) one hole trapping level H near the valence band (e.g., a cation vacancy), (b) one electron trapping level N near the conduction band (e.g., an interstitial cation, a Cr^{3+} in MgO, or an anion vacancy) and, (c) three recombination levels — one R neutral (e.g., perhaps Fe^{2+} in MgO), one R_- with a localized e^- and consequently possessing a high cross-section for recombination with an h^+ (e.g., perhaps Fe^{1+} in MgO), and one R_+ with a localized h^+ and a high cross-section for recombination with an e^- (e.g., perhaps Fe^{3+} in MgO). Such a model may be illustrated by a band level diagram shown as follows:



Allowing the symbols H, R, and N to represent the total density of levels (filled and empty) and using the following symbols to account for charge carriers:

p = density of free holes

p_H = density of trapped or localized holes

n = density of free electrons

n_N = density of trapped or localized electrons

we may express, in order, the time-dependent trapped hole, free hole, trapped electron, and free electron rate equations as follows:

$$dp_H/dt = k_1 p(H - p_H) - p_H/\tau_p - p_H/O_H \quad (20)$$

$$dp/dt = g_{p+} + p_H/\tau_p - k_1 p(H - p_H) - k_3 pR - k_2 pR_- + p_H/O_H \quad (21)$$

$$dn_N/dt = k_6 n(N - n_N) - n_N/\tau_n - n_N/O_N \quad (22)$$

$$dn/dt = g_{p+} + n_N/\tau_n - k_6 n(N - n_N) - k_4 nR - k_5 nR_+ + n_N/O_N \quad (23)$$

where

k_1 = rate constant for trapping holes at H

k_2 = rate constant for h^* recombination with localized e'

k_3 = rate constant for localization of h^* at recombination center

k_4 = rate constant for localization of e' at recombination center

k_5 = rate constant for e' recombination with localized h^*

k_6 = rate constant for trapping electrons at N

Note: All rate constants in units of $\text{cm}^3/\text{sec-species}$.

τ_p = time constant for thermal release of h^* from trap H, sec.

τ_N = time constant for thermal release of e' from trap N, sec.

g_{p+} = $e'-h^*$ generation rate by proton, pairs/ $\text{cm}^3\text{-sec}$

O_H = time constant for optical bleaching of trapped h^* by the resonant flux I_H contained in the solar spectrum, $\text{sec}, = 1/I_H \sigma_H$

O_N = time constant for optical bleaching of trapped e' by the resonant flux I_N contained in the solar spectrum, $\text{sec}, = 1/I_N \sigma_N$

σ_H = photon absorption cross-section of h^* trapped at H, $\text{cm}^2/\text{photon}$

σ_N = photon absorption cross-section of e' trapped at N, $\text{cm}^2/\text{photon}$

On the basis of conservation we may write:

$$R_o = R + R_- + R_+$$

The time dependent densities of recombination centers are related through the following rate expressions:

$$dR_+/dt = k_3 p R - k_5 n R_+ \quad (24)$$

$$dR/dt = k_2 p R_- + k_5 n R_+ - k_4 n R - k_3 p R \quad (25)$$

$$dR_-/dt = k_4 n R - k_2 p R_- \quad (26)$$

Note that k-values represent trapping or recombination rate constants as appropriate to the transition. The τ -values designate time constants for thermal release from trap levels. O_H and O_N represent time constants for optical (solar) bleaching of a single species of trapped hole and trapped electron, respectively. Hopefully these latter terms can be simplified. For example, in MgO, O_N is largely operable in the UV (e.g., the F center) and might easily be omitted from consideration, with O_H retained to account for bleaching of the V_1 center (2.3 eV).

Generation of trap densities is considered a function predominantly of p^+ collision kinetics and has been given previously in equation (4). This expression gives the time dependent density of Frenkel pairs. Since Frenkel pair generation effectively determines the dominant trapping level densities in the proton region, equation (4) may also be used to express H or N as follows:

$$H(t) = \frac{\frac{3}{4\pi r^3} \tanh \left[\frac{4\pi r^3}{3} \cdot \frac{\rho n \phi}{R_p} \cdot t \right] + H(o)}{1 + \frac{4\pi r^3}{3} \cdot H(o) \tanh \left[\frac{4\pi r^3}{3} \cdot \frac{\rho n \phi}{R_p} \cdot t \right]} \quad (27)$$

As an illustrative example, one may assume $k_4 \gg k_3$. Thus the transition involving k_5 cannot occur to any significant extent. This one assumption then reduces the 5-level band model to a more manageable 3-level model which contains only one recombination level. R_- .

Additional simplification results if one can select a material in which the major coloration is primarily related to a single level of only one type of trapped species. Fortunately, MgO has only one color center in the visible spectrum. This consists of a hole trapped at a cation vacancy and is termed the V_1 center. As a first effort, one may thus examine the above photo-chemical model for the case of MgO and $k_4 \gg k_3$. The pertinent expressions (including equation 27) thus condense to the following:

$$\frac{dp}{dt} = g_{p^+} + p_H/\tau_p + I_H \sigma_H p_H - k_1 p(H - p_H) - k_2 p R_- \quad (28)$$

$$\frac{dp_H}{dt} = k_1 p(H - p_H) - p_H/\tau_p - I_H \sigma_H p_H \quad (29)$$

It has been found that, for this case, both dp/dt and dp_H/dt reach steady state very quickly after changes in H. Thus in effect $p(t)$ and $p_H(t)$ values track the very much slower changes in H. Thus dp/dt and dp_H/dt may be placed equal to zero. On this basis a value of $k_1 p$ may be derived from equation (28) as follows:

$$k_1 p = \frac{g_{p+} + I_H \sigma_H p_H + p_H / \tau_p}{H - p_H + (k_2/k_1) R_-} \quad (30)$$

This value when substituted in equation (29) yields:

$$\frac{dp_H}{dt} = \left[\frac{g_{p+} + I_H \sigma_H p_H + p_H / \tau_p}{H - p_H + K R_-} \right] (H - p_H) - p_H / \tau_p - I_H \sigma_H p_H = 0 \quad (31)$$

$$\therefore p_H = \frac{g_{p+} H}{g_{p+} + K R_- / \tau_p + I_H \sigma_H K R_-} \quad (32)$$

where: $K = k_2/k_1$

For this simplified three level system then, equations (32) and (27) provide an explicit expression of the time dependent trapped hole density $p_H(t)$, in this case assumed exclusively to be the V_1 center in MgO.

A final step in this development of a model for the proton region consists of relating optical change with the time dependent density of color centers (V_1 in this example) induced by the protons. Such optical attenuation may be conveniently expressed by Beer's law, since the proton projected range R_p is less than the diameter of a typical pigment particle. Furthermore, since the column of particles in a pigment array (in a coating) typically exceeds the scattering range for solar photons, the path ℓ associated with optical extinction in the proton region is equal to $2R_p$. Thus one may express the attenuation in spectral reflectance as follows:

$$\frac{\rho'_\lambda(t)}{\rho'_\lambda(o)} = \exp(-\alpha_\lambda \ell) = \exp(-\alpha_\lambda \cdot 2R_p) \quad (33)$$

where:

$\rho'_\lambda(t), \rho'_\lambda(o)$ = spectral reflectance at time t and initially, respectively
 α_λ = spectral absorption coefficient, cm^{-1}
 R_p = projected range of proton of energy E , cm

The spectral absorption coefficient $\alpha_{\lambda}(\text{max})$ (at the spectral peak λ_{max} of the color center optical absorption band) is related to the density of centers by Smakula's expression as follows:

$$\alpha_{\lambda}(\text{max.}) = \sigma C_D \quad (34)$$

where:

$$C_D = \text{color center density, no./cm}^3$$

σ = average photon absorption cross section of a center (of half width W eV, oscillator strength f , and given index of refraction), in $\text{cm}^2/\text{photon}$

For the particular example involving the V_1 center in MgO, one may thus substitute $p_H(t)$ for C_D in equation (34). Further substitution of this modified equation (34) into equation (33) yields a normalized reflectance expression for the peak of the V_1 band as follows:

$$\left[\frac{\rho'(t)}{\rho'(0)} \right]_{\lambda_{\text{max.}}} = \exp \left[-\sigma_H p_H(t) \cdot 2R_p \right] \quad (35)$$

By appropriate substitution of equations (32) and (27) into equation (35), one thus obtains the proton-induced reflectance attenuation at the peak of the color center band,

$$\left[\rho'(t) / \rho'(0) \right]_{\lambda_{\text{max.}}}$$

in terms of time t , proton flux ϕ , and various material-derived parameters.

2.4.1.2 Example of Use of Proton Model

A first example might consist of predicting the coloration of high purity MgO by a 3000 eV monoenergetic beam normally incident at the solar rate, say 2.5×10^8 p+/cm²-sec. Outlined as follows are the bases for the calculated parameters required:

(a) Select 1 ppm Trivalent Impurity Level (e.g. Fe³⁺ or Cr³⁺):

$$R_-(0) = \left[6.02 \times 10^{23} \times 3.65/40.3 \right] 10^{-6} = 5.5 \times 10^{16} \text{ recomb. centers/cm}^3$$

Since one cation vacancy is created by every two Cr^{3+} , the number of cation vacancies (= no. hole traps initially) is as follows:

$$H(0) = (1/2)5.5 \times 10^{16} = 2.75 \times 10^{16} \text{ hole traps/cm}^3$$

Assume initial trapping of holes is small. Thus let $p_H(0) \approx 2.75 \times 10^{15}$ trapped holes/cm³

(b) Obtain Value of τ_p

From Chen and Sibley⁶ one obtains (as approximated by a 5 ppm Fe-content single crystal) 1/e thermal decay of the V_1 center in ~7 hours. Thus:

$$\tau_p = 7 \times 3600 = 2.52 \times 10^4 \text{ sec}$$

(c) Obtain Value of R_p

From Figure 1, one notes that the path for cation displacement (H generation) terminates at that proton energy (~165 eV) below which the required displacement energy (~25 eV) cannot be transferred in nuclear collision. Thus we find that $R \approx 7.09 \times 10^{16}$ cm. From Appendix C (Table C1) we have therefore:

$$R_p = R/\beta \approx 7.09 \times 10^{-6}/3.8 \approx 1.87 \times 10^{-6} \text{ cm}$$

(d) Obtain Forcing Functions

Based on data in Figures 2 and 7, one may write the following expression for hole trap generation rate A:

$$\begin{aligned} A = \rho n \phi / R_p &= (0.56) \left[(1.709 \text{ hole traps/p}^+)(2.5 \times 10^8 \text{ p}^+/\text{cm}^2\text{-sec}) / 1.87 \times 10^{-6} \text{ cm} \right] \\ &= 1.28 \times 10^{14} \text{ hole traps/cm}^3\text{-sec} \end{aligned}$$

Based on the energy partition shown in Figure 1 an expression for e⁻-h⁺ pair generation rate g_{p^+} is obtained as follows:

$$\begin{aligned}
g_{p^+} &= \frac{\Delta E(\text{ioniz.})}{2E_g/\text{pair}} \cdot \frac{\phi}{R_p} = \frac{2500 \text{ eV}/p^+}{(2 \times 10^8 \text{ eV}/\text{pair})} \cdot \frac{2.5 \times 10^8 \text{ p}^+/\text{cm}^2\text{-sec}}{1.87 \times 10^{-6} \text{ cm}} \\
&= 1.67 \times 10^{16} \text{ pairs}/\text{cm}^3\text{-sec} \\
&= 1.67 \times 10^{16} \text{ free } h^+/\text{cm}^3\text{-sec}
\end{aligned}$$

(e) Obtain Volume/Frenkel pair (see Equation 19) from:

$$\frac{4}{3} \pi r^*{}^3 = 3.7 \times 10^{-22} \text{ cm}^3/\text{Frenkel pair}$$

(f) Obtain Value of σ_H for V_1 Center in MgO

Using data of Chen and Sibley⁶ and Dexter's⁷ modification of Smakula's equation one obtains:

$$\sigma_H = 2.6 \times 10^{-17} \text{ cm}^2/\text{photon}$$

(g) Obtain Value of Optical Bleaching Flux I_H

The value I_H corresponds to that portion of the solar flux which falls within the spectral half width limits of the V_1 band. Thus:

$$\begin{aligned}
I_H &= I_S(\lambda = 4450\text{\AA}) - I_S(\lambda = 6810\text{\AA}) \\
&= 1.637 \times 10^{17} \text{ photons}/\text{cm}^2\text{-sec}
\end{aligned}$$

(h) Assume Value of K

As a first estimate assume that the recombination rate (k_2) is much greater than the hole trapping rate (k_1). This inequality has been observed experimentally in this laboratory in other similar work. Thus let $K = k_2/k_1 = 1000$.

The results of the above described attempt to theoretically estimate coloration kinetics in high purity MgO with 3000 eV protons only is shown in Figure 11 by the curve labeled $I_H = 0$. Additionally, the optical bleaching effect by the resonant (V_1) component of the solar emission spectrum is shown. This solar bleaching is indicated to be quite marked and serves to suppress coloration. Barring other factors, negligible change in reflectance is indicated to occur in 10^8 sec. This corresponds to a cumulative fluence of $\sim 2.5 \times 10^{16}$ p+/cm² which would be obtained in interplanetary space over a period of about three years.

Quantitatively, solar bleaching is a dominant process because it is found that its time constant for this system is relatively fast, being of the order of 0.2 second, $= (\sigma_H I_H)^{-1}$. On the other hand $\tau_p \approx 2.5 \times 10^4$ sec. Slowest of all processes is the rate of trap generation with a time constant of the order of

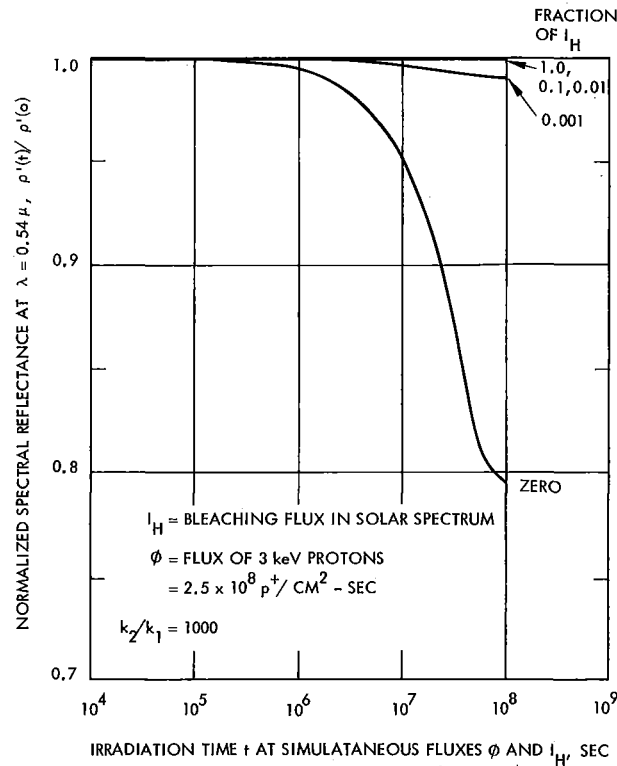


Figure 11. Model predicted reflectance attenuation induced in the proton region of high purity MgO by simultaneous irradiation with 3 keV protons and the solar spectrum.

2.1×10^7 sec,

$$\tau = \left[\frac{4}{3} \pi r^*{}^3 \cdot \rho n \phi / R_p \right]^{-1}.$$

Thus experimental irradiation and measurement procedures must incorporate precautions against extraneous optical bleaching effects.

A second effort to test this preliminary proton region model was by comparison with data reported by Holland⁸ for 10 keV protons on MgO. The fluence was 5×10^{15} p⁺/cm² delivered at 5.5×10^{11} p⁺/cm²-sec. It was roughly estimated that the material contained Fe³⁺ or Cr³⁺ at a concentration of ~ 100 ppm. Using procedures similar to those described earlier for 3 keV p⁺ → MgO (high purity), proton-induced reflectance attenuation in the proton region was calculated. This is shown in Figure 12. There is considerable discrepancy between Holland's point at 9.1×10^3 sec ($= 5 \times 10^{15} / 5.5 \times 10^{11}$) and the calculated value shown for zero optical bleaching. This discrepancy probably results from:

- (a) Incorrect estimation of impurity content
- (b) Occurrence of limited optical bleaching during irradiation or reflectance measurement
- (c) Limitations of model in its simplified state

While any combination of the above factors could explain this disagreement, it is believed to stem mostly from factor (a). Thus the stated MgO purity is 99.41% (by wt. ?). On this basis the density of recombination centers with localized electrons, $R_{\underline{}}$, will likely be greater than the $\sim 5 \times 10^{18}$ /cm³ associated with the assumed concentration of Fe³⁺ or Cr³⁺ as 100 ppm. Assumption of a concentration of recombination centers of the order of 800 ppm is probably more reasonable. Such a revised estimation of selected impurities is shown to yield improved agreement (dashed curves - Figure 12) between calculated and experimental values upon assumption of a low level of optical bleaching.

2.4.2 UV Scattering Region

Current evidence reveals no indication of exciton bands occurring at the absorption edge of high purity MgO. This does not preclude exciton generation by UV photons (in the solar spectrum) with energy as little as 6.2 eV in other dielectric solids. Pending experimental evidence that such a UV damage mechanism can exist in the UV scattering range, the photochemical model for the UV region has been postponed. Such a model will be more meaningful when based on carefully controlled experiments with UV alone.

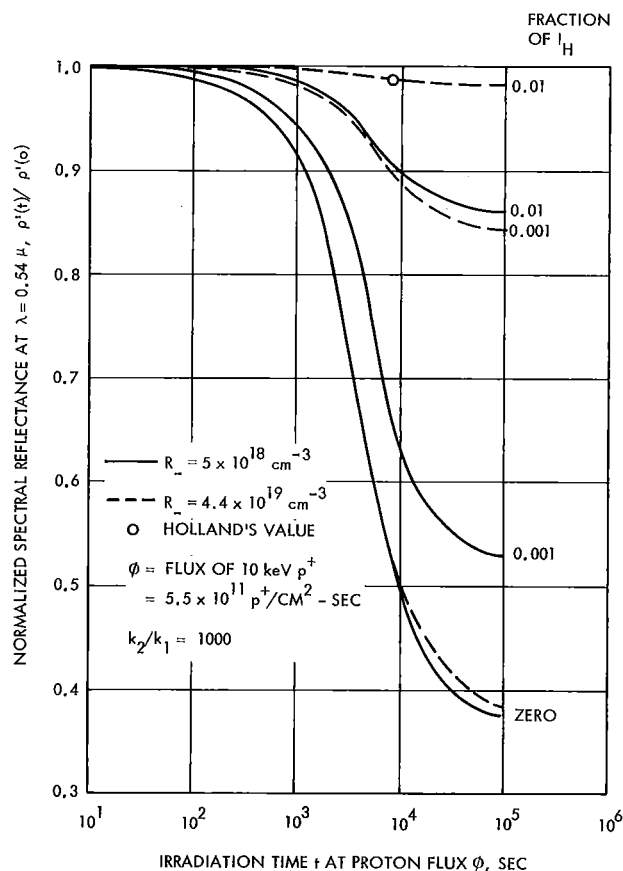


Figure 12. Comparison of calculated and measured reflective attenuation in "reagent grade" MgO in the proton region by 10 keV protons.

Most reported descriptions of UV-generated V_1 centers in MgO, e.g., that by Lunsford⁹ with $\lambda = 2537\text{\AA}$, probably do not involve ionization across the band gap. Instead, e^-h^+ pair generation by near-UV is likely associated with ionization of impurity levels within the band gap. In fact Wertz et al¹⁰ indicate that the density of trapped holes "produced by 4.9 eV or X-radiation is strongly dependent on the concentration of impurities in the crystal."

3.0 HIGH PURITY MATERIAL CONSIDERATIONS

Although it remains to be demonstrated, assume that coloration within the proton stopping region represents the major portion of the measured pigment coloration induced by combined solar wind protons and the solar spectral emission. Previous review (section 2.4.1) of the photochemical kinetics in the proton region, which extends from the surface inwards a distance R_p , reveals that radiative attenuation of spectral reflectance is most sensitively affected by the nature of the color center or centers involved. Perhaps equally important in the case of high purity materials (i.e. those having initially low densities of trapping levels associated with pertinent color centers) is the radius r^* , below which self-annealing of certain color center trapping levels can occur. Although less sensitively affected by R_p values, reflectance attenuation remains a function of the optical path ($2 R_p$) in the colored region.

3.1 Nature of Absorbing Color Center

The color centers pertinent to this effort are those which absorb radiant energy in the visible and near-IR spectra. A measure of a center's ability to selectively absorb such radiant energy is given by its average photon absorption cross section, σ . This can vary by an order of magnitude among centers within a given compound or between different compounds as follows:

$$\sigma(\text{F-center in ZnO}) = 2.8 \times 10^{-16} \text{ cm}^2 \text{ per } 2.8 \text{ eV avg. photon}$$

$$\sigma(\text{V}_1\text{-center in MgO}) = 2.6 \times 10^{-17} \text{ cm}^2 \text{ per } 2.3 \text{ eV avg. photon}$$

Upon reference to equation (35), selection of a minimum σ value would seem desirable in terms of minimizing reflectance attenuation. Unfortunately a simple procedure for arranging such selection is not apparent. Although Ivey type relationships, e.g. $\lambda_{\max} \propto (\text{lattice constant})^2$, have been shown to correlate some features of centers in certain generic groups (e.g. alkali halides¹¹ and alkaline earth oxides¹²), broad correlation useful for material selection purposes does not appear feasible. Instead, compounds will have to be examined first on an individual basis in terms of such experimental data as exists. Comparison between compounds may then follow to the extent possible.

3.2 Radius r^*

For a given material, trap generation appears to be coloration-rate-controlling. From equation (27) it is seen that r^* determines trap saturation density and also contributes to the time constant for the trap generation process. Upon consideration of various dielectric solids, it has been observed that the trap generation function, $\rho n \phi / R_p$, is not particularly sensitive

to material parameters. Thus it would appear that the time dependent trap density associated with pertinent color centers is quite sensitive to the r^* value.

As demonstrated in section 2.3.2.2 the estimation of this critical radius is quite a complex task for even a simple cubic lattice such as MgO. There are experimental methods for estimating these r^* values. Thus, in those cases where it can be established that the proton-induced defect introduction rate is coloration rate-controlling, r^* can be estimated from the "dark" decay rate of optical or ERP spectra observed in irradiated specimens. Suffice to say, no ready theoretical correlation of r^* with crystal lattice is apparent. An illustration of the nature of the problem is seen by comparing a face centered cubic lattice, e.g. MgO (Figure 13), with a rhombohedral lattice, e.g. Al_2O_3 (Figure 14).

The orderly ionic array in MgO will be observed. Note that the $V_{\text{Mg}}'' - \text{Mg}_i^{\bullet}$ pair (Frenkel defect) shown at r^* separation $[= (3/2)\sqrt{2} r_0]$ is intended for comparison with Figure 9.

On the other hand the ionic array in corundum ($\alpha - \text{Al}_2\text{O}_3$) is much less regular. A unit cell containing two molecules of Al_2O_3 is outlined. In addition to the electrostatic and overlap repulsive considerations previously discussed for the case of MgO, the inequality between cation and anion charge

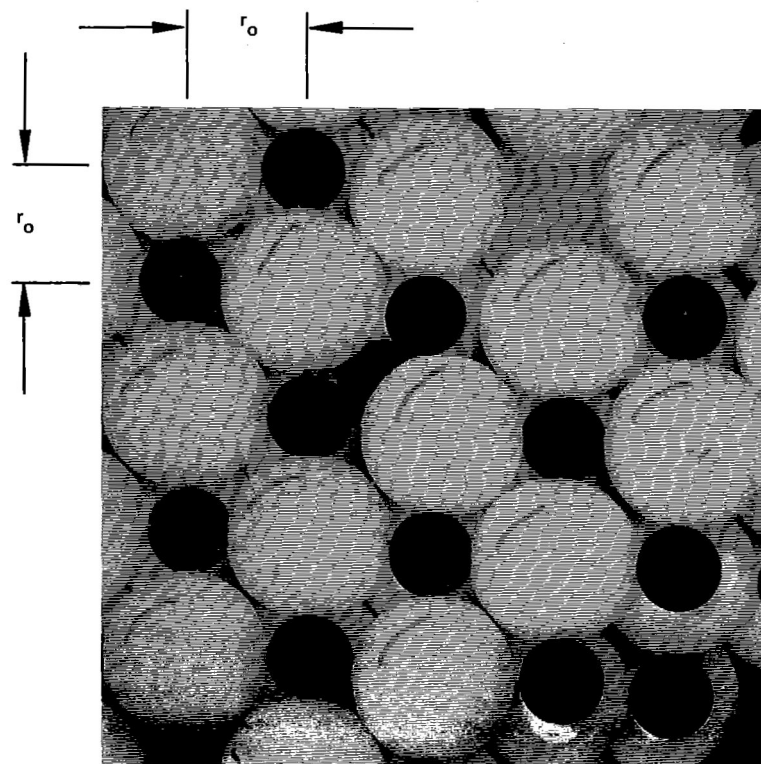


Figure 13. MgO crystal model (face centered cubic).

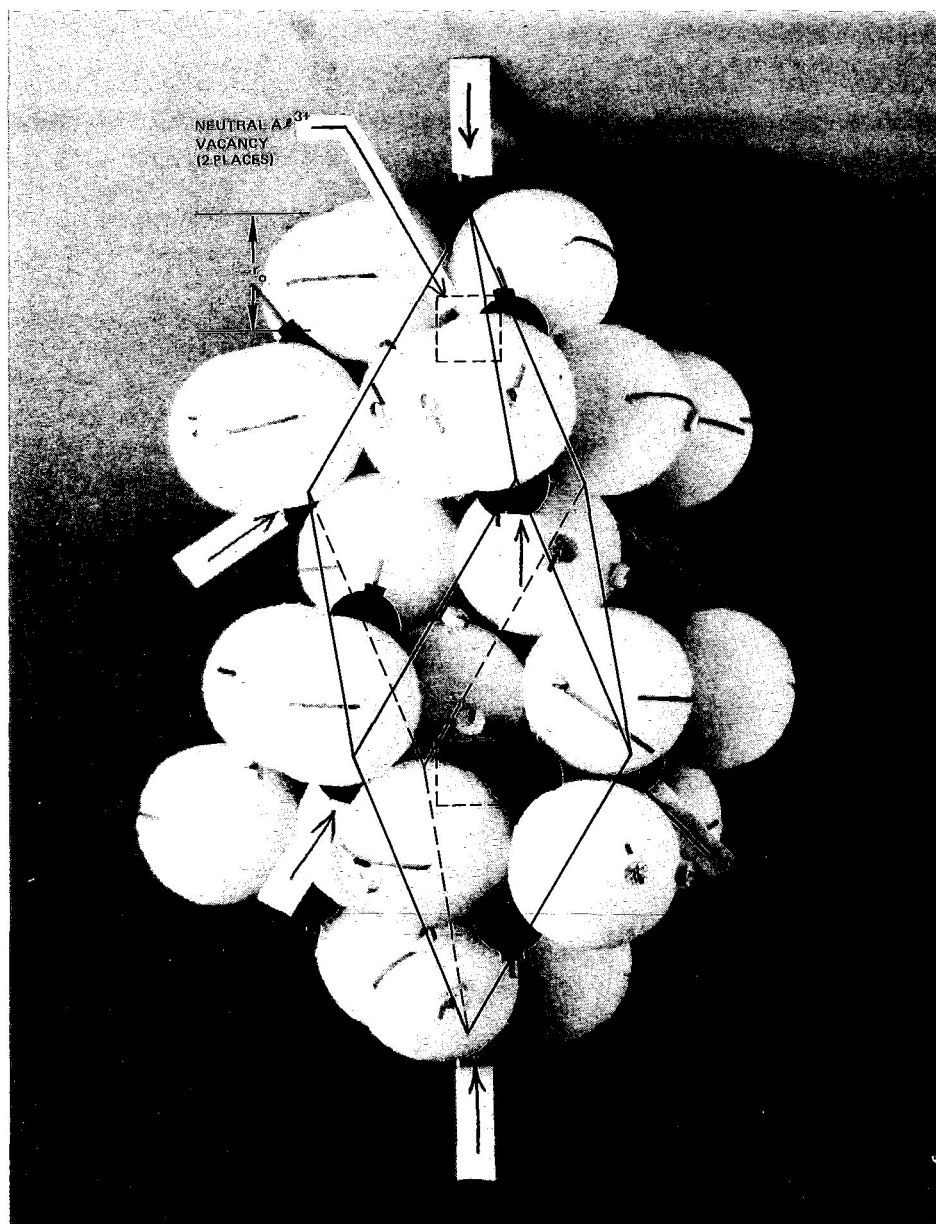


Figure 14. α - Al_2O_3 crystal model (rhombohedral).

introduces two uncharged vacancies into the unit cell as shown. Thus an additional complexity enters the problem since these sites would appear to readily accommodate proton-induced interstitials.

Based on what has been learned, limited generalization regarding r^* values may prove acceptable. Values of r^* pertaining to oxide dielectric solids will probably be small, i.e. $< \sim 3 r_0$. Variation between solids will

probably be no greater than by a factor of two, i. e. $\sim 1.5 r_0$ to $\sim 3 r_0$. Such variation could introduce an order of magnitude into the material selectivity process.

3.3 Projected Proton Range R_p

The range parameter R_p is not very sensitive to compound composition. Thus it provides only limited selectivity with regard to materials. A recent review of low energy proton channeling in crystals by McCargo, Greenberg, and Breuch¹³ indicates that crystal structure does play a role in determining the total random path of the proton in a target. The net effect of such channeling, on the distribution of displacement and ionization damage along a projected path (which is less than the diameter of crystallites randomly arrayed in a layer normal to the proton at incidence), remains to be demonstrated. It is possible, however, that compound arrangement (i. e. crystal type) may prove to significantly affect collision kinetics and thus R_p values.

4.0 EXPERIMENTAL STUDY PROGRAM

The objective of an experimental effort ought to be twofold, namely: (a) provide feed-back useful for refining the degradation model and (b) direct attention toward potentially useful high purity materials in terms of acceptable defect structure.

It is conceivable that a given material at a given impurity density level would be desirable in a variety of forms. Thus thin film (100 to 200Å) poly- or single crystals would offer an opportunity to verify the predicted high saturation color center densities. At the same time proton range estimates could be checked and channeling effects observed. Bulk single crystals in comparison with compressed powders (consisting of particles $\leq 1\mu$ diameter) may prove useful in studying damage in the UV region. Compressed powders would provide the ultimate check on material usefulness and model validity.

In terms of radiation sources, a low energy proton gun, a xenon lamp, and perhaps a higher energy proton source are required. The low energy proton beam should be neutralized (with ~ 1 eV electrons) and either mono-energetic (0.75 to 3 keV) or distributed in energies about 1.5 to 1.75 keV. Desirably, the flux would be variable between $\sim 2.5 \times 10^8$ and $\sim 2.5 \times 10^{11}$ $p^+/\text{cm}^2\text{-sec}$ in a uniform beam approximately 3 cm in diameter.

In terms of studying UV photoexcitation while minimizing optical bleaching, it is recommended that UV irradiation be carried out at wavelengths less than 0.25 to 0.3 μ , the lower wavelengths being preferred. Intensities of the order of 100 x solar, with respect to this near UV band, are deemed necessary to avoid unduly long experimental times. The UV source may have either a continuous or line emission. Thus a 5 KW Xenon lamp with a suitable high side blocking filter and a quartz condensing lens should prove adequate. Alternatively, a low pressure mercury arc source (2537 Å line emission) of suitable power flux should be satisfactory. It is suggested that these photoexcitation studies be performed first without simultaneous optical bleaching, i. e. irradiating with only the selected UV band. Subsequently, simultaneous exposure to the selected UV band and one or more selected bleaching bands in the visible-near IR spectrum is proposed.

In certain cases it would be desirable to uncouple optical bleaching from proton defect introduction. Such irradiation "in the dark" is difficult to do experimentally with 1-3 keV p^+ incident on sub-micron powders because the projected range of the p^+ is several orders of magnitude less than the scattering range of visible-near IR photons. Higher energy radiation (5-10 MeV p^+), selected so as to introduce defect structure primarily in the specimen bulk, would facilitate such "dark" irradiation.

A number of experimental techniques have been used to identify defect structure in crystals. These vary widely in ease of application, precision, resolution capability, information generated, etc. It is thought that, in terms of the data required to extend this development effort, a combination of reflectance and paramagnetic resonance spectroscopy should prove satisfactory. Correlation between such spectra (measured in situ in specimens irradiated under carefully controlled conditions of temperature, absorbed radiation dose, and radiation rate) should greatly aid in establishing the controlling transitions in the energy band model. Further, measurements of spectral decay rates (either thermally or optically induced) can enable calculation of various transition rate constants.

Specifically, the indicated spectroscopic data is designed to provide certain of the parameters illustrated in section 2.4.1.2. For example, the time constant for thermal decay of a given, radiation - induced center, e. g. τ_p , may be calculated directly from the measured, time - dependent dark decay of the EPR signal or the optical absorption. Additionally, the effect of the density of a selected recombination center on τ_p may be observed by irradiation of a series of specimens of a single material containing varying densities of a single dopant.

A second parameter of major importance is the photon absorption cross section of a particular color center, e. g. σ_H . This may be calculated from the characteristic optical absorption (or reflectance) band of the center when the oscillator strength f of this center is available. If required, f may be determined by EPR measurement of the center density (for those centers characterized by unpaired spin) used in conjunction with spectral band data.

By means of these and other required parameters, (as discussed in detail earlier) one can formulate a photochemical model that should be consistent with the net measured reflectance attenuation induced by the radiation involved. Achievement of a kinetic model consistent with controlled experiment demonstrates basic understanding of the controlling processes involved in radiative coloration of white powder pigments. As such it provides a powerful tool for use in selecting candidate pigments.

5.0 CONCLUSIONS

A systematic theoretical effort has been carried out. Its purpose was to identify those parameters which effectively regulate space radiation-induced coloration in those white powder compounds relevant to spacecraft thermal control coatings. Such quantitative identification has progressed to a level which permits the following conclusions regarding radiative coloration:

(a) Crystalline Powders

(1) Maximum color center density is a function of the minimum stable separation of vacancy-interstitial pairs. This separation is in turn intimately related to crystal structure and ionic charge.

(2) A large degree of sensitivity to materials parameters is contained in the absorption band characteristic of a given color center in a given crystal lattice. Characterized by constants in Smakula's equation, these parameters include the magnitude of the absorption cross section, half width, and index of refraction as well as location of the absorption band relative to the solar spectrum. Correlation of such parameters between generically dissimilar compounds does not appear feasible.

(3) Pending identification of coloration in the UV region, wide band gap solids appear to minimize UV contributions to coloration from the combined radiation environment. At the same time selective, solar, spectral bleaching occurs which opposes coloration. In this regard, high purity MgO and Al₂O₃ with low intrinsic defect structure still look promising. The reader is cautioned that much of the reported optical data obtained on these two crystals is really associated with defect structure rather than the basic lattice.

(4) Impurity content has two important effects. First, such impurities may act as recombination centers to inhibit color center growth. Secondly, impurities which differ in valence from that of the host ions contribute to the initial color center density through the equilibrium density of lattice defects. The latter are insignificant in the proton range region due to the high density of injected defects, although in the UV range such existing defects could be significant. Wet chemical synthesis methods followed by appropriate vacuum thermal processing seem to offer the best route to high purity, insulator-type solids.

(5) Certain analytical relationships (photochemical model) have been developed to estimate radiation-induced reflectance attenuation in the proton stopping region.

(6) An experimental effort is proposed in order to improve the model in the proton stopping region, extend it to the UV scattering region, and demonstrate its ability to select radiation-resistant white powder compounds suitable for spacecraft thermal control coatings.

(b) Amorphous Powders

Direct application of model theory to solids possessing only short range order will be limited at best. Some useful information may result by analogy (applied with great care) with their crystalline counterparts, where such exist. Fortunately the number of glasses that might prove pertinent to this development is limited. Therefore the handicap relative to material selection of amorphous powders should prove manageable.

6.0 REFERENCES

1. Holmes, D.K., "The Range of Energetic Atoms in Solids", Proceedings of Symposium: Radiation Damage in Solids, International Atomic Energy Agency, Vienna, pp. 23-26 (1962).
2. Lindner, R., and Parfitt, G.D., "Diffusion of Radioactive Magnesium in Magnesium Oxide Crystals," J. Chem. Phys. 26, 182 (1957).
3. Fletcher, R.C., and Brown, W.L., "Annealing of Bombardment Damage in a Diamond-Type Lattice: Theoretical," Phys. Rev. 92, 585-590 (1953).
4. Seitz, F., "Color Centers in Alkali Halides," Rev. Mod. Phys. 18, 396 (1946).
5. Reitz, J.R., and Gammel, J.L., "Dissociation Energies of the Cd^{2+} Vacancy Complex and of the Double Vacancy in Sodium Chloride," J. Chem. Phys. 19, 899 (1951).
6. Chen, Y., and Sibley, W.A., "Study of Ionization-Induced Radiation Damage in MgO ," Phys. Rev. 154, 844-6 (1967).
7. Dexter, D.L., "Absorption of Light by Atoms in Solids," Phys. Rev. 101, 48 (1956).
8. Holland, W.R., "Stability of Thermal Control Coatings Exposed to Combined Space Environments," NASA Report CR 73160, pp. 4, 70, 77 (Dec. 1967).
9. Lunsford, J.H., "A Study of Irradiation Induced Active Sites on Magnesium Oxide Using Electron Paramagnetic Resonance," J. Phys. Chem. 68, 2312-16 (1964).
10. Wertz, J.E., Orton, J.W., and Auzins, P., "Spin Resonance of Point Defects in Magnesium Oxide," J. App. Phys. 33 (supplement), 328 (1962).
11. Ivey, H.F., "Spectral Location of the Absorption Due to Color Centers in Alkali Halide Crystals," Phys. Rev. 72, 341-3 (1947).
12. Johnson, B., "Color Centers in Strontium Oxide," Ph.D. Thesis — Univ. of Missouri, p. 63 (1967).
13. McCargo, M., Greenberg, S.A., and Breuch, R.A., "Study of Environmental Effects Upon Particulate Radiation Induced Absorption Bands in Spacecraft Thermal Control Coating Pigments," NASA CR-73289.

APPENDIX A

REVIEW OF PERTINENT SPACE ENVIRONMENT

The pertinent environment is interplanetary space. In this environment the radiation of prime importance to thermal control coating degradation is solar in origin and consists of continuous solar electromagnetic and particulate emission. Solar electromagnetic emission is reasonably well characterized. The particulate emission of importance is the continuous solar plasma which flows radially from the sun.

For radiation physics, the solar plasma (wind) presents two interesting aspects. First, the incident particle energies are smaller than those usually considered in the province of high energy effects. This in turn leads to considerations of the interaction of a charged particle and a stopping medium in an energy range that only recently has been explored in its basic aspects. Secondly, the solar wind is properly a plasma and as such must be electrically neutral in any macroscopic volume. This means that the protons and heavier ions must be accompanied by an electronic component. If they all have the same directed velocities outward from the sun then the electron energy will be of the order of 1 eV. While this represents a fairly "hot" electron from the point of view of solid state physics, it is a very slow particle from the point of view of radiation damage effects. Nevertheless, it is believed that this electronic component should not be neglected in the "chemistry" of the effect of the solar plasma on thermal control material.

That this plasma is indeed electrically neutral is evidenced by the flux of very low energy electrons reported by Serbu and Maier¹ for IMP 2. Additionally the plasma contains hydrogen nuclei (protons) and helium nuclei (alpha particles) in a ratio dependent on velocity. Neugebauer and Snyder² have summarized "the average properties of the positive ion component of the solar wind as determined by the electrostatic spectrometer on Mariner II" (Venus probe) as follows:

$$\begin{aligned}\text{average proton velocity } (\bar{v}_p) &\approx 500. \text{ km/sec} \\ \text{average proton density } (\bar{n}_p) &\approx 5. \text{ p}^+/\text{cm}^3 \\ \alpha/\text{p}^+ \text{ ratio } (@\bar{v}_p = 500 \text{ km/sec}) &\approx 0.08\end{aligned}$$

Corresponding to \bar{v}_p , one may calculate an average energy of 1.3 keV. Further, the product $\bar{n}_p \bar{v}_p$ yields the average flux $\approx 2.5 \times 10^8$ protons/cm² - sec. According to Dr. Snyder³, Mariner II data demonstrates almost continuous variation in the flux-energy spectrum with time. However there is evidence to indicate the plasma spectra peaks fall within a limited energy range of ~ 0.75 to 2.5 keV. Additionally an order of magnitude flux variation about the above average value is probably typical.

The above proton data have been generally confirmed by data from Mariner IV⁴ (Mars probe), Mariner V (Venus probe)³ and Pioneer 6⁵.

The electron component, with 1/1837 the mass of the proton and the same velocity, would be expected to have 1/1837 of the p⁺ energy, or an

order of 1 eV. Serbu and Maier¹ did in fact observe an electron flux in the solar wind similar to p^+ flux levels with a Maxwellian distribution of energies below 2 eV.

At the observed solar plasma densities, mean free paths are obviously large enough to prevent charge annihilation of individual particles. Thus the degradation kinetics remain based on charged particle-material interaction. Because of their low energy, electron-induced ionization effects should be negligible. Electron excitation effects may warrant further consideration.

Cosmic radiation is not being considered a factor. Deposition rates in surface coating thicknesses by galactic proton radiation does not appear serious because of the typical low flux at energy levels of importance. The temporal character of solar (flare) radiation introduces complexities beyond the scope of this work.

Summarizing, in terms of color center kinetics associated with interplanetary particulate radiation, induced ionization and displacement effects are largely determined by 1 to 3 keV protons incident at the rate of 10^8 to 10^9 protons/cm² - sec. Interplanetary electromagnetic radiation will primarily affect color center kinetics by inducing various photoexcitation and in certain cases photoionization processes as a result of solar photon absorption.

REFERENCES

1. Serbu, G.P., and Maier, E.J.R., "Low Energy Electrons Measured on IMP 2," J. Geophys. Res. 71, 3755 (1966).
2. Neugebauer, M., and Snyder, C.W., "Average Properties of the Solar Wind as Determined by Mariner II," Jet Propulsion Laboratory Tech. Rept. No. 32-991 (NASA N67-10253), pp. 1, 4, 5, 9, 19 (1966). See also Science 138, 1096 (1962).
3. Snyder, C.W., private communication.
4. Lazarus, A.J. Bridge, H.S., Davis, J.M., and Snyder, C.W., "Initial Results from the Mariner 4 Solar Plasma Experiment," Space Research VII, vol. 2, edited by R.L. Smith-Rose, North Holland Publishing Co., Amsterdam, pp. 1300-1 (1967).
5. Lazarus, A.J. Bridge, H.S., and Davis, J.M., "Preliminary Results from the Pioneer 6 MIT Plasma Experiment," J. Geophys. Res. 71, 3790 (1966).

APPENDIX B

CHARGE STATE OF SOLAR WIND PROTON IN TARGET MATERIAL

1.0 Implications Pertinent to Damage Model

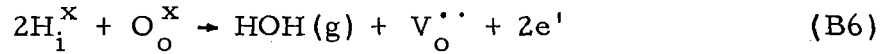
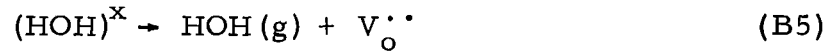
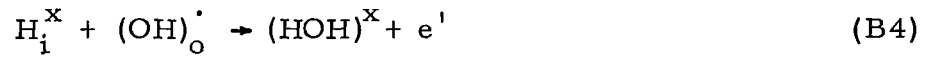
As reviewed in Appendix A, the neutral solar plasma deposits at a unit surface in space equal numbers of oppositely charged particles, e' (~ 1 eV) and H^+ (~ 1 to 3 keV), in a given time. Because of their extremely low kinetic energy, the electrons remain at or very near the surface. There is some reason to believe they induce a net negative space charge to the surface.

The 1-3 keV protons (H^+) have sufficient kinetic energy to penetrate the surface. Immediately upon entry charge equilibration as follows is permitted:



The source of the electrons available to charged beams are the valence electrons of the target ions. In this case involving a neutral plasma, the surface deposited electrons may also effect this equilibration, since (as will be discussed later) at ~ 3 keV, the probability for electron capture (indicated by capture cross section σ_{10} in cm^2) far exceeds the probability for electron loss (indicated by loss cross section σ_{01}). To the extent that gas experiments are indicative, the formation of H^- is negligible at the conditions of interest.

The sub-model that emerges (supported by later arguments) indicates that the incident H^+ equilibrates to a mostly neutral hydrogen atom H^0 prior to significant loss of its energy or traversal of its range. The H^0 then proceeds to generate electronic and displacement disorder until its energy drops below ~ 175 eV, at which time electronic stopping only continues down to ~ 20 eV. It is apparent that since we are dealing with a "thick target" (thickness $\gg R_p$), the ultimate fate of the H^0 is also important to describing irradiation-induced defect structure. This ultimate fate, after its energy has been expended in the creation of both atomic and electronic disorder, is the implantation as H^0 atoms. These are capable of creating both impurity and atomic disorder as follows:



The symbols are those used by Professor F.A. Kröger, where

superscript x = neutral species; e. g., interstitial atom,
ion at its normal lattice site, or
electronically-filled vacancy

superscript dot = contributes a net single positive charge to
lattice

superscript prime mark = contributes a net single negative charge to
lattice

subscript i = interstitial species

subscript element = refers to ion normally occupying the lattice
site specified

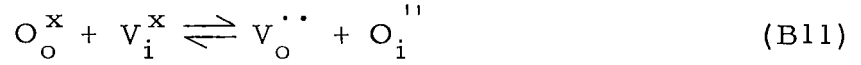
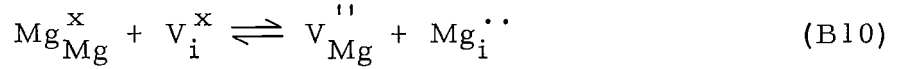
Note that the charged (empty) oxygen vacancy, $V_o^{\cdot\cdot}$, may singly or doubly
trap electrons. Thus



Since the plasma bombardment in space does not permit equilibration
between disorder states, one must resort to describing the transient kinetics
involved. Especially important is the identification of the rate controlling
transitions.

Frenkel disorder generation and $e' - h'$ pair production complete the
major elements of the solar plasma defect generation sub-model. For a
metal oxide, e. g., MgO, these may be expressed as follows:





Disorder rates (forward direction) are of course dependent on the H^+ flux and energy and material constants. In the case of the interstitials, re-order rates (back transition) are a function of local diffusion (self-annealing) and second order annealing.

2.0 Arguments for Neutral Hydrogen Particle

2.1 Lindhard's¹ Arguments Based on Bohr² Relation

Bohr distinguishes between the methods applicable to describe the collision of a fast particle of velocity v and charge q_1 with another at rest (i. e., in the target medium) and having charge q_2 through a parameter κ as follows:

$$\kappa = \frac{2q_1 2q_2}{\hbar v} \quad (\text{B12})$$

When $\kappa > 1$, classical mechanics apply. When $\kappa < 1$, quantum perturbational methods should be used. Bohr further points out that the average charge q_1 of the moving particle in strongly screened collisions is of the following order:

$$q_1 = Z_1^* e = e Z_1^{1/3} (v/v_o) \quad (\text{B13})$$

Lindhard argues that based on equation (B13), the moving ion begins to carry electrons "to an appreciable extent" when $v < v_o Z_1^{2/3}$. This is readily apparent since satisfaction of this inequality is equivalent to stating that $q_1 < e Z_1$, where $e Z_1$ is the original charge of the moving particle.

The domain of applicability may be considered in terms of a specific example of interest, e. g., the interaction of a 1 keV $\text{H}^+ \rightarrow \text{MgO}$.

$$E = (1/2) m v^2 \quad (\text{B14})$$

where

E = proton energy in ergs ($\text{g-cm}^2/\text{sec}^2$)

m = proton mass, g

v = proton velocity, cm/sec

$$v = (2E/m)^{1/2} = \left[\frac{(2) 10^3 \text{ eV} / (6.24 \times 10^{11} \text{ eV/erg})}{(1.67 \times 10^{-24} \text{ g})} \right]^{1/2} = 4.4 \times 10^7 \text{ cm/sec} \quad (\text{B15})$$

Since v_o (electron velocity in first Bohr orbit, i. e., ground state of hydrogen) $= e^2/\hbar = 2.18 \times 10^8 \text{ cm/sec}$,

$$v_o Z_1^{1/3} = (2.18 \times 10^8)(1)^{1/3} = 2.18 \times 10^8 \text{ cm/sec} \quad (\text{B16})$$

where Z_1 = atomic number of proton.

Thus, it is noted that, in a representative case, $v < v_o Z_1^{2/3}$ at incidence and the proton immediately can capture electrons. The maximum degree of neutralization of the proton permitted by charge equilibration at this incident velocity is obtained from (B13) as follows:

$$q_1(\text{incidence}) = (e)(1^{1/3})(4.4 \times 10^7 / 2.18 \times 10^8) = 0.2e \quad (\text{B17})$$

Equilibration at this velocity thus results in 80 percent of the particles being neutral at a given time, this percentage increasing with decreasing velocity. As discussed later there is some justification in believing that such equilibration occurs prior to significant energy transfer and thus is representative of the charge state during energy transfer.

Referring back to (B12), the magnitude of κ is found as follows for the interaction cited earlier (where $\text{avg. } q_2 = (12 + 8)/2 = 10$):

$$\begin{aligned}
\kappa &= \frac{2(0.2e)(10e)}{(1.05 \times 10^{-27})(4.4 \times 10^7)} \\
\kappa &= \frac{4(4.80 \times 10^{-10} \text{ cm}^{3/2} \text{ g}^{1/2} \text{ sec}^{-1})^2}{(1.05 \times 10^{-27} \text{ g cm}^2 \text{ sec}^{-1})(4.4 \times 10^7 \text{ cm sec}^{-1})} \\
&= 20
\end{aligned} \tag{B18}$$

Since $\kappa > 1$, energy transfer can be considered according to classical methods.

Also note that according to Lindhard, electronic stopping is dominant when $v \leq v_0 Z_1^{2/3}$. When $v \ll v_0 Z_1^{2/3}$ (e.g., $v = 0.015 v_0 Z_1^{2/3}$) nuclear stopping is dominant. In the above example electronic stopping is therefore the dominant energy transfer process, at least initially. Further, it can be shown for the interaction $p^+ \rightarrow \text{MgO}$ (as approximated by $p^+ \rightarrow \text{Mg}^{2+}$) using Lindhard's dimensionless stopping power relationships for both electronic and nuclear stopping, e.g.,:

$$(d\epsilon/dp)_e = \kappa \epsilon^{1/2} \tag{B19}$$

$$(d\epsilon/dp)_n = (\text{constant}) S_n \tag{B20}$$

that both energy transfer mechanisms become equally probable when the proton energy is reduced from incident to $\sim 27 \text{ eV}$ ($= E_c$). Above this critical energy value (also termed "ionization limit"), electronic transfer (inelastic process leading to ionization) is dominant although nuclear stopping cannot be ignored. Conversely, between the minimum energy for displacement E_{\min} and E_c (i.e., $E_{\min} < E < E_c$) nuclear stopping is dominant. In a practical sense, since E_{\min} ($\approx E_D/\alpha^2 \approx 165 \text{ eV}$ for Mg^{2+}) is greater than E_c there is no dominant region for nuclear stopping.

2.2 Experimental Evidence

2.2.1 Studies With $\text{H}^+ \rightarrow \text{Solids}$

Phillips^{3, 4} reported evidence that a low energy proton beam (of the order of one keV) will charge equilibrate almost immediately after striking a solid oxide target (e.g., Al_2O_3 or SiO_2) and become a predominantly neutral beam. His measurements with a pure H^+ beam incident on these typical insulator oxides demonstrate that charge equilibration occurs within the first 5-10 ionic diameters along the projected range, at which point an initially

1-3 keV beam is 85 to 83 percent neutral. The H^0 content increases with decreasing initial proton energy.

2.2.2 Studies With $H^+ \rightarrow H_2^0$ (gas)

Allison, Cuevas, and Garcia-Munoz⁵ observed that when a pure proton beam (in keV energy region) enters a molecular hydrogen gas, it develops a "neutral component which attains the fraction, $1-1/e$, of its equilibrium value before more than a negligible decrement in the beam's kinetic energy has taken place." The growth of this neutral fraction F_0 (in the initially pure H^+ beam) toward an equilibrium value F_{∞} may be expressed in terms of an electron capture cross section σ_{10} , an electron loss cross section σ_{01} , and the number of target atoms/cm² traversed by the beam designated π as follows:

$$F_0 = F_{\infty} \{1 - \exp[-\pi (\sigma_{01} + \sigma_{10})]\} \quad (B21)$$

For the special case mentioned above when charge equilibration is $1-1/e$ ($= 0.632$) completed, i. e., $F_0 = 0.632 F_{\infty}$, the beam must have traversed $(\sigma_{01} + \sigma_{10})^{-1}$ atoms/cm² with negligible energy loss. For the interaction $H^+ \rightarrow H_2$ (gas), Allison, et al., have graphically summarized capture cross sections as a function of H^+ incident energy yielding the following values at $E_1 = 1$ keV:

$$H^+ + e' \rightarrow H^0; \sigma_{10} \approx 3 \times 10^{-16} \text{ cm}^2/\text{atom} \quad (B22)$$

$$H^0 \rightarrow H^+ + e'; \sigma_{01} \approx 10^{-17} \text{ cm}^2/\text{atom} \quad (B23)$$

Thus, $(0.1 \times 10^{-16} + 3 \times 10^{-16})^{-1} \approx 3.2 \times 10^{15}$ atoms/cm² have been traversed by the beam at 63.2 percent equilibration. Assuming such an approach to charge equilibration is equally probable in an atom density $n_0 \approx 5 \times 10^{22}$ atoms/cm³ (an approximation for Mg^{2+} in MgO), the corresponding path of the primary H^+ particle is $\approx 3.2 \times 10^{15} / (5 \times 10^{22}) \approx 6 \times 10^{-8} \text{ cm} \approx 6 \text{ \AA}$. Under these conditions, the actual (i. e., total) path length is of the order of 300 \AA . It is therefore apparent that such equilibrium approach occurs prior to significant energy transfer.

Further, F_{∞} is given as follows:

$$F_{\infty} = \sigma_{10} / (\sigma_{10} + \sigma_{01}) \approx \frac{3 \times 10^{-16}}{0.1 \times 10^{-17} + 3 \times 10^{-16}} \approx 0.97 \quad (B24)$$

With the equilibrated 1 keV H^+ beam essentially neutral (i. e., a given particle is neutral 97 percent of the time) and approach to equilibrium so rapid, one may conclude (based on the pertinence of the gas to the solid system) that the neutral H^0 is the dominant charge state prior to energy transfer.

The evidence appears reasonable to conclude that both elastic and inelastic collision processes occurring in target solids irradiated by the solar wind involve neutral hydrogen atoms primarily which are implanted and ultimately concentrated near the projected range. The ultimate fate of these hydrogen atoms remains to be determined. Professor Kröger suggests that their possible function as donor states be considered. Such a function would be important in terms of coloration kinetics.

REFERENCES

1. Lindhard, Jr., Studies in Penetration of Charged Particles in Matter (Nuclear Science Series Report #39), Nat. Acad. Science - Nat. Res. Council, Washington, p. 3-4 (1964).
2. Bohr, N., Kgl. Danske Videnskab. Selskab, Mat. -fys. Medd. 18 no. 8, (1948).
3. Phillips, J. A., "Charge Equilibrium Ratios for Hydrogen Ions from Solids," Phys. Rev. 97, 404-10 (1955).
4. Phillips, J. A., "Equilibrium Proton Charge Ratios From Charge Exchange in Various Materials," Phys. Rev. 91, 455(A) (1953).
5. Allison, S.K., Cuevas, J., and Garcia-Munoz, M., "Partial Stopping Power of Gaseous Hydrogen for Hydrogen Beams I," Phys. Rev. 127, 792-4 (1962).

APPENDIX C

CONTENTS

<u>Section</u>	<u>Page</u>
1.0 Introduction	59
2.0 Lattice Displacement Efficiency by keV Protons (n) .	60
2.1 Total Cross Section for Displacement – Single Ion or Atom Basis	60
2.2 Stopping Relations for Compounds	62
3.0 Distance Traveled by Proton in Target Compound . .	70
3.1 Average Proton Random Path R Over Which Ion Displacement Occurs	70
3.2 Average Proton Projected Range R_p	72
4.0 Bulk Displacement Rate of Ions in the Crystal (n')	74
5.0 Lattice Ionization Yield by keV Protons .	74

APPENDIX C

LOW ENERGY PROTON COLLISION THEORY

1.0 Introduction

Low energy (keV range) protons constitute the major charged particle flux in interplanetary space. Hence a study of energy transfer by low energy ions, e.g., keV ^1H and keV heavier ions, to ionic solids, especially inorganic oxides is certainly pertinent to the kinetics of radiative coloration. The ^1H relate to the solar p^+ , the primary or incident particle, and the heavier ions to the knock-ons generated when primaries or knock-on ions are successful in displacing lattice ions.

For incident ion energies in the KeV range the work of Lindhard¹⁻⁶ and his colleagues is fundamental. A review of their work reveals that two principal energy transfer interactions are involved, namely, (1) inelastic encounters of the p^+ with valence electrons of the target ion and (2) elastic encounters with the target ion as a whole. In the first case average energy loss per unit path length is measured by the electronic stopping cross section per ion, $S_e(E)$, and in the second case by the nuclear stopping cross section per ion (i.e., per scattering center), $S_n(E)$, both being a function of p^+ energy.

In addition, a number of experiments have now been carried out and reported with the objective of testing the Lindhard, et al., theory. Of importance are papers by Duckworth^{7, 8} and colleagues and some recent work by Professor Suita⁹ and colleagues. In both cases deviations from the theory were detected. In the former work a periodic behavior in $S_e(E)$ for a given material as a function of atomic number of the incident ion was found. This may be interpreted as an effect occurring in the valence electrons that is not predicted by the statistical Thomas-Fermi model employed by Lindhard. The work of Suita, et al., is very interesting as it is concerned with incident protons in various metal films. Again, deviations from the Lindhard theory were found. The discrepancy was explained by consideration of a charge-exchange process, one involving electron capture and loss by the incident proton (i.e., equilibration between allowed charge states of the projectile ion) prior to energy transfer to the target medium.

The analysis which is presented in this appendix is more correctly applicable to amorphous solids. Crystalline solids do offer channeling opportunities to the energetic proton with resultant increase in total path length of the projectile particle. Extending Lindhard⁶ channeling theory in order to obtain $S_e(E)$ values, McCargo, Greenberg, and Breuch¹⁰ recently reported approximate, total path values for a one keV p^+ in zinc and lanthanum. These values were 5 to 7 times greater in the crystalline solid than in the amorphous solid. At this time it is impossible to infer from such data a dose-depth profile having practical implications in terms of the coloration kinetics of pigment crystallites arranged as a coating layer. There simply is no ready basis for equating channeling-induced increases in the projectile's total path with an increase in target penetration (projected range). Thus this analysis of collision kinetics will treat channeling effects in crystals as a future refinement, pending developments in this area.

2.0 Lattice Displacement Efficiency By keV Protons (n)

2.1 Total Cross Section for Displacement – Single Ion or Atom Basis

In terms of keV protons incident on real thermal control coatings, the average total path length \bar{R}_1 for a proton of initial energy E_1 (say = 1. keV) is very small compared to typical coating thicknesses of several mils. Thus the pertinent physical model is one involving a "thick target," i.e., one in which total energy attenuation of the proton energy occurs in the target. Thus energy transfer occurs between the limits: $E = E_1$ at $\bar{R} = 0$; $E = 0$ at $\bar{R} = \bar{R}_1$. Note that \bar{R} designates the actual average path length measured along the track of the incident proton. It should not be confused with the average projected path length or range \bar{R}_p , that target penetration measured in a direction normal to the surface. In the development which follows symbols R and R_p are used to denote \bar{R} and \bar{R}_p , respectively.

"The probability that a given amount of energy will be transferred" from a primary (incident) particle to a lattice ion "is best expressed in terms of an area through which the particle trajectory must pass if the energy transfer is to occur. This area is called the differential cross section for energy transfer $d\sigma$. Hence, if the particle has energy E and if it transfers an energy between T and $(T + dT)$ to a lattice ion, the differential cross section will be given by:"¹¹

$$\frac{d\sigma(E, T)}{dT} \cdot dT \quad (C1)$$

In order to relate energy transfer with ion displacement, $d\sigma(E, T)$ must be integrated over all possible transferred energies great enough to cause displacement. For the sake of simplicity assume a sharp threshold value $E_D \approx 25$ eV as the lower limit of transferred energy required for displacement. For comments on more exact definition of E_D see reference 11. The maximum amount of energy that can be transferred (upper limit of integration) corresponds to a direct collision. From Seitz and Koehler,¹² this maximum energy transfer T_m between a projectile with incident energy E and mass M_1 in any given collision with a target atom of mass M_2 at rest, is as follows:

$$T_m(E) = \left[\frac{4 M_1 M_2}{(M_1 + M_2)^2} \right] E = \alpha^2 E \quad (C2)$$

where

α = an arbitrary constant

Integration over the above limits in T yields the total cross section for displacement $\sigma_D(E)$ as follows:

$$\sigma_D(E) = \int_{E_D}^{T_m(E)} \frac{d\sigma(E, T)}{dT} dT \quad (C3)$$

In the remaining discussion, $\sigma_D(E) \equiv \sigma_D$ and $T_m(E) \equiv T_m$.

The development of collision theory by Linhard, et al., is based on a classical mechanical treatment of the scattering in nearly elastic collisions between low velocity ions and atoms at rest using a Thomas-Fermi expression for differential scattering cross section. This treatment is considered applicable when the incident particle velocity $v < v_0 Z_1^{2/3}$, where v_0 is the electron velocity in the first Bohr orbit ($= 2.18 \times 10^8$ cm/sec) and Z_1 is the atomic number of the particle. Since the maximum energy of protons of interest is 3 keV and since each has a velocity of 7.6×10^7 cm/sec (with $Z_1 = 1$), the condition for application is met. The differential cross section for energy transfer in a random scattering process is thus written by Lindhard, et al., as follows:

$$d\sigma = \frac{S_n}{2} \frac{1}{T_m^{1/2}} \frac{dT}{T^{3/2}} \quad (C4)$$

where S_n is considered constant at low projectile velocity. The total cross section for displacement follows by integration of equation (C4) between the limits E_D to T_m :

$$\sigma_D = \int_{E_D}^{T_m} d\sigma = \frac{S_n}{2} \frac{1}{T_m^{1/2}} \int_{E_D}^{T_m} \frac{dT}{T^{3/2}} = \frac{S_n}{T_m^{1/2}} \left[\frac{1}{E_D^{1/2}} - \frac{1}{T_m^{1/2}} \right] \quad (C5)$$

Substituting a value of T_m from equation (C2) into equation (C5) yields:

$$\sigma_D = \frac{S_n}{\alpha E^{1/2}} \left[\frac{1}{E_D^{1/2}} - \frac{1}{\alpha E^{1/2}} \right] \quad (C6)$$

2.2 Stopping Relations for Compounds

The atomic stopping cross section per atom (or molecule) S is defined by Lindhard as follows:

$$S = - \frac{1}{N} \frac{dE}{dR} \quad (C7)$$

where:

$$N = n_0 = \text{no. molecules/cm}^3 ; \quad S = \text{eV} \cdot \text{cm}^2/\text{molecule}$$

For a compound $A_j B_m$, where j and m are the number of atoms (or ions) per molecule of A and B , respectively, Whaling¹⁸ indicates the following relationship between compound (S_{AB}) and component stopping cross section (S_A and S_B):

$$S_{AB} = jS_A + mS_B \quad (C8)$$

where

$$j = \text{no. A atoms/molecule } A_j B_m$$

$$m = \text{no. B atoms/molecule } A_j B_m$$

Note carefully that the specific energy loss (generally termed stopping power) in the compound $(dE/dR)_{AB}$, from which the range in the compound is derived, follows from equation (C7):

$$-(dE/dR)_{AB} = N_{AB} S_{AB} = N_{AB} (jS_A + mS_B) = jN_{AB} S_A + mN_{AB} S_B \quad (C9)$$

where

$$N_{AB} = \text{No. molecules of the compound } A_j B_m/\text{cm}^3$$

$$= A \rho_{AB} / M_{AB}$$

$$A = \text{Avogadro's no.} = \text{no. molecules per mol. wt. of compound in grams}$$

$$M_{AB} = \text{g-mol. wt. of compound}$$

$$\rho_{AB} = \text{density of compound, g/cm}^3$$

Note that the product jN_{AB} (= no. A atoms/molecule $A_j B_m$ x no. molecules $A_j B_m/\text{cm}^3$ = no. A atoms/ cm^3) is equal to N_A , no. A atoms/ cm^3 . Similar

reasoning leads to the equality $mN_{AB} = N_B$. Thus equation (C9) may be expressed either in terms of N_{AB} or alternatively in terms of N_A and N_B .

For the general case of stopping due to both nuclear and electronic processes the stopping cross sections for each ion may be expressed as a sum of nuclear S_n and electronic stopping cross sections S_e as follows:

$$S_A = S_{nA} + S_{eA} \quad ; \quad S_B = S_{nB} + S_{eB} \quad (C10)$$

Values of S_n do decrease rapidly at very low energies (e.g., when the proton's energy has dropped to less than a few hundred eV). However in the energy range (say 500 to 3000 eV) where displacement is significant, Lindhard's work indicates that S_n is fairly insensitive to particle energy and may be considered constant. Thus according to Lindhard and Scharff³ we may write the following expressions:

$$S_n = (0.83)(\pi^2/2) e^2 a Z_1 Z_2 \left[M_1 / (M_1 + M_2) \right] = \text{constant} \quad (C11)$$

where

a = atomic screening radius in cm

$$= (0.8853) a_o (Z_1^{2/3} + Z_2^{2/3})^{-1/2}$$

a_o = first Bohr radius in hydrogen atom

$$= \hbar^2 / (me^2) = 5.29 \times 10^{-9} \text{ cm}$$

Z_1 = nuclear charge of $p^+ = 1$

Z_2 = nuclear charge of target ion

M_1 = proton mass = 1

M_2 = target ion mass

$$\therefore S_{nA} = C_A \quad ; \quad S_{nB} = C_B \quad (C12)$$

Lindhard and Scharff³ also present an expression for electronic stopping power S_e in terms of particle energy E as follows:

$$S_e = \left[\xi_e 8 \pi e^2 a_o \frac{Z_1 Z_2}{\left(Z_1^{2/3} + Z_2^{2/3} \right)^{3/2}} \right] \frac{v}{v_o} \quad (C13)$$

Since non-relativistic velocities are involved:

$$E(\text{in ergs}) = 1/2 m v^2$$

$$\therefore v = \left[(2/m)^{1/2} E^{1/2} \right] 6.24 \times 10^{11} \quad (C14)$$

where E is in eV. Substituting (C14) in (C13) yields:

$$S_e = \left[\xi_e 8 \pi e^2 a_o \frac{Z_1 Z_2 (2/m)^{1/2} 6.24 \times 10^{11}}{\left(Z_1^{2/3} + Z_2^{2/3} \right)^{3/2} v_o} \right] E^{1/2} = k' E^{1/2} \quad (C15)$$

where

k' = front factor in brackets (in consistent units when E is in eV).

Substitution of equations (C12) and (C15) into equations (C10) yields the following:

$$S_A = C_A + k'_A E^{1/2} \quad ; \quad S_B = C_B + k'_B E^{1/2} \quad (C16)$$

Thus one has expressed the stopping cross section of each ion (A and B) in compound $A_j B_m$ in terms of projectile energy E and certain constants.

2.3 Cation (A) and Anion (B) Displacement as a Function of Proton Energy

Seitz and Koehler state that the number of primary lattice atoms (or ions) displaced, dn , by a primary particle of energy E_1 in moving an actual distance dR through a solid is given as follows:

$$dn = n_o \sigma_D dR \quad (C17)$$

This differential expression for the number of displacements per proton n in terms of actual path dR , displacement cross section σ_D , and molecular density n_0 may be rewritten to reflect association with compound $A_j B_m$ as follows:

$$dn_{AB} = N_{AB} (\sigma_D)_{AB} dR_{AB} \quad (C18)$$

The relation between compound $(\sigma_D)_{AB}$ and component stopping cross section $(\sigma_A$ and $\sigma_B)$ is similar to that described by Whaling, equation (C8), and may be expressed as follows:

$$(\sigma_D)_{AB} = \sigma_{AB} = j(\sigma_D)_A + m(\sigma_D)_B \quad (C19)$$

where

$$j = \text{no. A ions/molecule } A_j B_m$$

$$m = \text{no. B ions/molecule } A_j B_m$$

Substituting (C19) into (C18) yields:

$$dn_{AB} = N_{AB} \left[j(\sigma_D)_A + m(\sigma_D)_B \right] dR_{AB} \quad (C20)$$

The total cross section for displacement characteristic of each ion, $(\sigma_D)_A$ and $(\sigma_D)_B$ respectively, may be expressed as in equation (C6) as follows:

$$(\sigma_D)_A = \frac{S_{nA}}{\alpha_A E^{1/2}} \left[\frac{1}{E_{DA}^{1/2}} - \frac{1}{\alpha_A E^{1/2}} \right] \quad (C21)$$

$$(\sigma_D)_B = \frac{S_{nB}}{\alpha_B E^{1/2}} \left[\frac{1}{E_{DB}^{1/2}} - \frac{1}{\alpha_B E^{1/2}} \right] \quad (C22)$$

where

E_{DA} = displacement threshold energy for A (typically the heavier ion)

E_{DB} = displacement threshold energy for B (typically the lighter ion)

$$\alpha_A^2 = \frac{4 M_1 M_A}{(M_1 + M_A)^2}$$

$$\alpha_B^2 = \frac{4 M_1 M_B}{(M_1 + M_B)^2}$$

M = mass (subscript 1 = proton, subscripts A and B relate to the ions of the compound)

S_{nA}, S_{nB} = nuclear stopping cross section for individual ion

By substitution of values for S_A and S_B from equation (C16) and rearranging, one obtains an expression for the differential actual path dR_{AB} of the projectile in the target material $A_j B_m$ as follows:

$$dR_{AB} = \frac{1}{N_{AB}} \left[\frac{-dE}{j S_{nA} + m S_{nB} + (j k'_A + m k'_B) E^{1/2}} \right] \quad (C23)$$

One may now obtain an expression for dn_{AB} in terms of E by substituting equations (C21), (C22), and (C23) into equation (C20) as follows:

$$dn_{AB} = N_{AB} \left\{ \frac{j S_{nA}}{\alpha_A E^{1/2}} \left[\frac{1}{E_{DA}^{1/2}} - \frac{1}{\alpha_A E^{1/2}} \right] + \frac{m S_{nB}}{\alpha_B E^{1/2}} \left[\frac{1}{E_{DB}^{1/2}} - \frac{1}{\alpha_B E^{1/2}} \right] \right\} \frac{1}{N_{AB}} \left[\frac{-dE}{j S_{nA} + m S_{nB} + (j k'_A + m k'_B) E^{1/2}} \right] \quad (C24)$$

Equation (C24) may be rearranged as follows:

$$\begin{aligned}
dn_{AB} = & - \frac{\left[\frac{j S_{nA}}{\alpha_A E_{DA}^{1/2}} + \frac{m S_{nB}}{\alpha_B E_{DB}^{1/2}} \right] dE}{\left[j S_{nA} + m S_{nB} + (j k'_A + m k'_B) E^{1/2} \right] E^{1/2}} \\
& + \frac{\left[\frac{j S_{nA}}{\alpha_A^2} + \frac{m S_{nB}}{\alpha_B^2} \right] dE}{\left[j S_{nA} + m S_{nB} + (j k'_A + m k'_B) E^{1/2} \right] E} \quad (C25)
\end{aligned}$$

Note that S_n may be considered constant in the energy range of interest. Equation (C25) may be simplified by grouping constants as follows: Let

$$\left. \begin{aligned}
B_1 &= \frac{j S_{nA}}{\alpha_A E_{DA}^{1/2}} \quad ; \quad B_2 = \frac{m S_{nB}}{\alpha_B E_{DB}^{1/2}} \quad ; \quad C_1 = B_1 + B_2 \\
D_1 &= \frac{j S_{nA}}{\alpha_A^2} \quad ; \quad D_2 = \frac{m S_{nB}}{\alpha_B^2} \quad ; \quad C_2 = D_1 + D_2 \\
C_3 &= j S_{nA} + m S_{nB} \quad ; \quad C_4 = j k'_A + m k'_B
\end{aligned} \right\} \quad (C26)$$

Substitution of the above constants from equation (C26) into equation (C25) yields:

$$dn_{AB} = \frac{- C_1 dE}{\left(C_3 + C_4 E^{1/2} \right) E^{1/2}} + \frac{C_2 dE}{\left(C_3 + C_4 E^{1/2} \right) E} \quad (C27)$$

Equation (C27) may be rearranged for integration as follows, where E_1 = incident proton energy and E_2 = minimum proton energy required to cause lattice displacement:

$$n_{AB} = -\frac{C_1}{C_4} \int_{E_1}^{E_2} \frac{dE}{\left(C_3/C_4 + E^{1/2}\right) E^{1/2}} + \frac{C_2}{C_4} \int_{E_1}^{E_2} \frac{dE}{\left(C_3/C_4 + E^{1/2}\right) E} \quad (C28)$$

For purposes of integration, temporarily let $E = x^2$ in equation (C28), integrating the first term directly and the second term by conversion first to the sum of two rational fractions. Thus, we have the following:

$$\begin{aligned} n_{AB} &= -\frac{C_1}{C_4} \int_{E_1^{1/2}}^{E_2^{1/2}} \frac{2 \, x \, dx}{(C_3/C_4 + x) \, x} + \frac{C_2}{C_4} \int_{E_1^{1/2}}^{E_2^{1/2}} \frac{2 \, x \, dx}{(C_3/C_4 + x) \, x^2} \\ &= \frac{2 \, C_1}{C_4} \int_{E_2^{1/2}}^{E_1^{1/2}} \frac{dx}{C_3/C_4 + x} + \frac{2 \, C_2}{C_4} \int_{E_1^{1/2}}^{E_2^{1/2}} \frac{dx}{(C_3/C_4 + x) \, x} \\ &= 2 \frac{C_1}{C_4} \ln \left[\frac{C_3/C_4 + E_1^{1/2}}{C_3/C_4 + E_2^{1/2}} \right] + 2 \frac{C_2}{C_4} \left(\frac{1}{C_3/C_4} \right) \ln \left[\frac{\frac{E_2^{1/2}}{C_3/C_4 + E_2^{1/2}}}{\frac{E_1^{1/2}}{C_3/C_4 + E_1^{1/2}}} \right] \\ &= 2 \frac{C_1}{C_4} \ln \left[\frac{C_3/C_4 + E_1^{1/2}}{C_3/C_4 + E_2^{1/2}} \right] + 2 \frac{C_2}{C_3} \ln \left\{ \left[\frac{C_3/C_4 + E_1^{1/2}}{C_3/C_4 + E_2^{1/2}} \right] \frac{E_2^{1/2}}{E_1^{1/2}} \right\} \\ n_{AB} &= 2 \left\{ \left[\frac{C_1}{C_4} + \frac{C_2}{C_3} \right] \ln \left[\frac{C_3/C_4 + E_1^{1/2}}{C_3/C_4 + E_2^{1/2}} \right] - \frac{C_2}{C_3} \ln \left(\frac{E_1^{1/2}}{E_2^{1/2}} \right) \right\} \quad (C29) \end{aligned}$$

Note that $n_{AB} = n_A + n_B$. Thus an expression for n_A may be inferred from equation (C29) by referring back to the constants C_1 and C_2 and inserting B_1 for C_1 and D_2 for C_2 . A similar procedure was used to obtain an expression for n_B . These expressions are as follows:

$$n_A = 2 \left\{ \left[\frac{B_1}{C_4} + \frac{D_1}{C_3} \right] \ln \left[\frac{C_3/C_4 + E_1^{1/2}}{C_3/C_4 + E_2^{1/2}} \right] - \frac{D_1}{C_3} \ln \left(\frac{E_1^{1/2}}{E_2^{1/2}} \right) \right\} \quad (C30)$$

$$n_B = 2 \left\{ \left[\frac{B_2}{C_4} + \frac{D_2}{C_3} \right] \ln \left[\frac{C_3/C_4 + E_1^{1/2}}{C_3/C_4 + E_2^{1/2}} \right] - \frac{D_2}{C_3} \ln \left(\frac{E_1^{1/2}}{E_2^{1/2}} \right) \right\} \quad (C31)$$

Recall that E_{DA} and E_{DB} represent the minimum energy which the proton must transfer to cation A and anion B, respectively, in order to displace either ion. Further, the maximum energy that a proton of energy E can transfer to a target is, from equation (C2), equal to $\alpha^2 E$. Therefore in order to cause a displacement a proton must have an energy $\geq E_D/\alpha^2$.

It is assumed that typically the anion, e.g., O^{2-} , will be lighter than the cation and further that the proton can effect anion displacement at residual energy levels below which it can transfer sufficient energy to cause cation displacement. This assumption may be expressed as:

$$E_{DA}/\alpha_A^2 > E_{DB}/\alpha_B^2 \quad .$$

It is for this reason that expression (C29) for n_{AB} can not be evaluated exactly, there being no common limit E_2 for cation A and anion B. Applicable limits of integration are thus:

For n_A (equation (C30))

$$E_1 \text{ to } E_2 = E_{DA}/\alpha_A^2$$

where:

$$E_1 \geq E \geq E_{DA}/\alpha_A^2$$

$$S_{nA} = \text{constant} \quad ; \quad S_{nB} = \text{constant}$$

For n_B (equation (C31))

$$E_1 \text{ to } E_2 = E_{DB}/\alpha_B^2$$

where:

$$E_1 \geq E \geq E_{DB}/\alpha_B^2$$

$$S_{nA} = \text{constant} \quad ; \quad S_{nB} = \text{constant}$$

Note that the residual proton energy, below which no ion displacement can take place, can still induce ionization between the limits E_{DB}/α_B^2 and $\sim 2 E_g$ (where E_g = band gap energy). In the case of the heavier ion, the range of residual proton energies permitting ionization and/or "heating" effects is even larger (see above), including energies between E_{DA}/α_A^2 and $\sim 2 E_g$. Thus, when the residual energy of a proton falls between

$$E_{DA}/\alpha_A^2 \text{ and } E_{DB}/\alpha_B^2 \quad ,$$

it is possible for it to ionize ion A or ion B or to displace ion B upon collision with either. Of course, at these low energies ($< \sim 150$ eV) it is difficult to distinguish between energy transfer resulting in ionization and that resulting simply in thermal effects.

3.0 Distance Traveled by Proton in Target Compound

3.1 Average Proton Random Path R Over Which Ion Displacement Occurs

By introducing the applicable constants from equation (C26) into equation (C23) an expression for the differential actual path dR_{AB} may be obtained as follows:

$$\begin{aligned} \int_0^{R_{AB}} dR_{AB} &= - \int_{E_1}^{E_2} \frac{dE}{N_{AB}(C_3 + C_4 E^{1/2})} \\ &= \frac{1}{N_{AB} C_4} \int_{E_2}^{E_1} \frac{dE}{(C_3/C_4 + E^{1/2})} \end{aligned} \quad (C32)$$

Integration of equation (C32) is facilitated by a change of variable such that $E = x^2$. On this basis $dE = 2x dx$, and the variable change converts equation (C32) into the following expression:

$$\int_0^{R_{AB}} dR_{AB} = \frac{2}{N_{AB} C_4} \int \left[\frac{x}{(C_3/C_4) + x} \right] dx \quad (C33)$$

The fraction under the integral sign at the right may be reduced to an integer and a rational fraction as follows:

$$R_{AB} = \frac{2}{N_{AB} C_4} \int 1 - \frac{C_3/C_4}{C_3/C_4 + x} dx = \frac{2}{N_{AB} C_4} \left[x - \frac{C_3}{C_4} \ln(C_3/C_4 + x) \right] \quad (C34)$$

Reverting back to the variable E and substituting appropriate limits for evaluation transforms equation (C34) into the following expression:

$$\begin{aligned} R_{AB} &= \frac{2}{N_{AB} C_4} \left[E^{1/2} - \frac{C_3}{C_4} \ln \left(C_3/C_4 + E^{1/2} \right) \right]_{E_2}^{E_1} \\ &= \frac{2}{N_{AB} C_4} \left\{ E_1^{1/2} - E_2^{1/2} - \frac{C_3}{C_4} \ln \left[\frac{C_3/C_4 + E_1^{1/2}}{C_3/C_4 + E_2^{1/2}} \right] \right\} \quad (C35) \end{aligned}$$

Path R_{AB} will consist of an initial random movement, during which both ions may be displaced, followed by a distance over which only the light ion (presumably the anion) is displaced. Finally, as discussed above, there will be a small terminal portion of the path over which no displacement can occur. That portion of the random path over which cation and anion displacement can take place is termed R_A . That random path over which anion (assumed to be the lighter) displacement occurs is termed R_B . Both R_A and R_B can be evaluated from equation (C35) by (a) insertion of proton energy limits (E_1 and E_2) appropriate to cation and anion displacement respectively (see earlier discussion), and (b) substitution of N_A or N_B for N_{AB} as required. On the basis that $R_B > R_A$, it is thus seen that the total actual path R_{AB} in a compound $A_j B_m$ is slightly greater than R_B .

3.2 Average Proton Projected Range R_p

In those cases involving proton incidence on metal oxides, the mass ratio M_2/M_1 (termed μ) is much greater than 1. For this pertinent situation, Schiott¹⁴ has graphically presented a projected range correction curve for protons ($\mu/k = 13.1$). Note that for $H^+ \rightarrow Mg^{2+}$ (as MgO):

$$k \approx \frac{0.0793 Z_1^{2/3} Z_2^{1/2} (M_1 + M_2)^{3/2}}{\left(Z_1^{2/3} + Z_2^{2/3} \right)^{3/4} M_1^{3/4} M_2^{1/2}} \approx 1.79 \quad (C36)$$

$$\mu = M_2/M_1 = 24.3/1 = 24.3 \quad (C37)$$

$$\mu/k \approx 24.3/1.79 \approx 13.6 \quad (C38)$$

with Schiott noting that the projected range correction dependence on μ/k is not very strong. Further, the Lindhard dimensionless energy expression ϵ for the above interaction at $E(H^+) = 3000 \text{ eV}$ may be evaluated as follows:

$$\epsilon = \left\{ \frac{\left[0.8853 a_o \left(Z_1^{2/3} + Z_2^{2/3} \right)^{-1/2} \right] M_2}{Z_1 Z_2 e^2 (M_1 + M_2)} \right\} E \quad \text{where: } E \text{ is in ergs}$$

$$= \left[\frac{(0.8853)(5.29 \times 10^{-9} \text{ cm})(1^{2/3} + 12^{2/3})^{-1/2} (24.3)}{(1)(12)(4.8 \times 10^{-10} \text{ cm}^{3/2} \text{ g}^{1/2} \text{ sec}^{-1})^2 (1 + 24.3)} \right] \frac{3 \times 10^3 \text{ eV}}{6.24 \times 10^{11} \text{ eV/erg}} = 3.1 \quad (C39)$$

Corresponding to this value of $\epsilon = 3.1$ is the ratio $\beta = R/R_p = 3.8$ which is to be associated with the path of a H^+ in a Mg^{2+} target. The following tabulation indicates the sensitivity of β to target parameters for the case of a 3000 eV H^+ projectile:

TABLE C1. - VALUES OF R/R_p FOR A 3000 eV PROTON INCIDENT
ON VARIOUS MATERIALS

Target		Z_1	Linhard's k	μ	μ/k	ϵ	$\beta = R/R_p$
Ion	M_2						
Mg^{2+} (as Mg O)	24.3	12	1.79	24.3	13.6	3.12	3.8
Al^{3+} (as Al_2O_3)	27	13	1.99	27	13.45	2.85	4.0
Si^{4+} (as SiO_2)	28	14	2.08	28	13.55	2.58	4.2
La^{3+} (as La_2O_3)	139	57	10.67	139	13.1	0.429	10.0

Note: The dependence of β on target material is observed as not large.

Values of R_A (see section 3.1) and β may be combined to yield estimates of the projected range R_p over which a proton of initial energy E_1 can effect cation displacement. Such R_p (cation) estimates are presented in Figure C1.

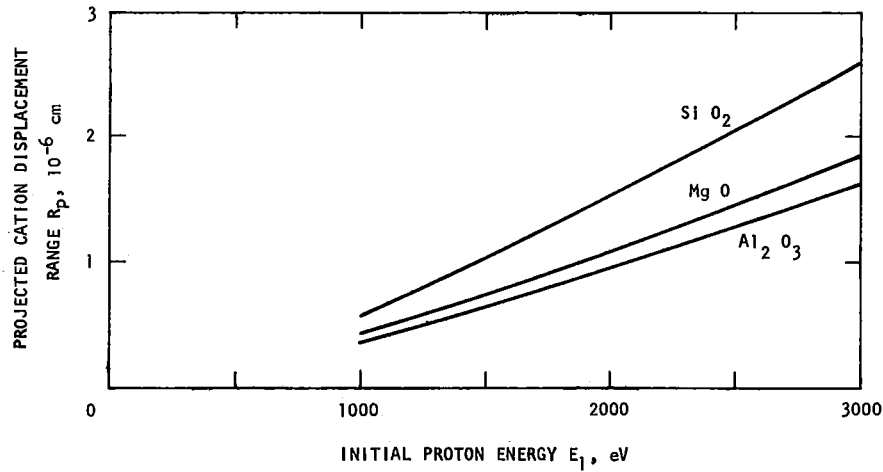


Figure C-1.

4.0 Bulk Displacement Rate of Ions in the Crystal (n')

The bulk or volumetric displacement rate n' of ions in the lattice may now be obtained. The number of primary displacements per proton n is given by equations (C30) and (C31). It has been estimated that, when protons of energy ≤ 3000 eV strike targets of interest, the average energy of the knock-on ions is $< \sim 70$ eV. Thus, on average, displacement production by knock-ons can be ignored, and the total displacement efficiency \approx primary displacement effectiveness. By means of the proton flux, R , and $\beta (= R/R_p)$ one may estimate a value for n' as follows.

$$n' = n \Phi / R_p = n \Phi \beta / R \quad (C40)$$

where:

$\beta = R/R_p$ = a constant which is a function of proton energy and of proton and target parameters as shown earlier

Φ = proton flux in $p^+/\text{cm}^2\text{-sec}$ and may be considered monoenergetic as a first approximation

5.0 Lattice Ionization Yield by keV Protons

Equation (C23) may be arranged, upon substitution of appropriate constants from equation (C26), to yield the following expression:

$$-dE = N_{AB} C_3 dR + N_{AB} \left(C_4 E^{1/2} \right) dR \quad (C41)$$

This resulting expression may be approximated on an incremental basis as follows:

$$-\Delta E = N_{AB} C_3 \Delta R + N_{AB} \left(C_4 E^{1/2} \right) \Delta R \quad (C42)$$

Note that the first term contains C_3 which represents nuclear stopping S_n and may be considered independent of E (see section 2.2). Electronic stopping (resulting in ionization) is given by the factor $C_4 E^{1/2}$ in the second term of equation (C42).

This equation may be numerically integrated to display the partition of the proton's incident energy E between nuclear absorption (first term) and ionization (second term). Thus, upon selection of an incident E value, say $E_1 = 3000$ eV, and a small increment of range ΔR_1 (say $\sim 0.02 R$), a corresponding energy loss ΔE_1 is calculated. This yields a new energy $E_2 (= E_1 - \Delta E)$ at the end of ΔR_1 . Based on E_2 a new value ΔE_2 is obtained

for a second range increment ΔR_2 . This process is repeated until $E_i \approx 2 E_g$. Summation of this incremental energy transfer to ionization per proton of initial energy E_1 (second term in equation(C42)) yields the ionization energy deposited per proton.

It is assumed that the energy required to generate an $e^- - h^+$ pair is $\approx 2 E_g$. On this basis the pair generation rate per proton is obtained by dividing the ionization energy deposited per proton by $2 E_g$.

REFERENCES

1. Lindhard, J., and Scharff, M., "Energy Loss in Matter by Fast Particles of Low Charge," Kgl. Danske Videnskab. Selskab, Mat.-fys. Medd. 27 (No. 15), 1-30 (1953).
2. Bohr, N., and Lindhard, J., "Electron Capture and Loss by Heavy Ions Penetrating Through Matter," *ibid.*, 28 (No. 7), 1-30 (1954).
3. Lindhard, J., and Scharff, M., "Energy Dissipation by Ions in the keV Region," Phys. Rev. 124, 128-130 (1961).
4. Lindhard, J., Scharff, M., and Schiott, H.E., "Range Concepts and Heavy Ion Ranges," Kgl. Danske Videnskab. Selskab, Mat.-fys. Medd. 33 (No. 14), 24-28 (1963).
5. Lindhard, J., Nielsen, V., Scharff, M., and Thomsen, P.V., "Integral Equations Governing Radiation Effects," *ibid.*, 33 (No. 10), 1-42 (1963).
6. Lindhard, J., "Influence of Crystal Lattice on Motion of Energetic Charged Particles," *ibid.*, 34 (No. 14), 1-64 (1965).
7. Ormrod, J.H., and Duckworth, H.E., "Stopping Cross Sections in Carbon for Low-Energy Atoms with $Z \leq 12$," Canad. J. Phys. 41, 1433 (1963).
8. Ormrod, J.H., MacDonald, J.R., and Duckworth, H.E., *ibid.*, 43, 280 (1965).
9. Morita, K., Akimune, H., and Suita, T., "Stopping Cross-Sections of Metallic Films for Projectile of Low Energy Proton," J. Phys. Soc, Japan 22, 1503 (1967).
10. McCargo, M., Greenberg, S.A., and Breuch, R.A., Final Report NASA Contract NAS 2-4353, pp 35-42 (January 1969).
11. Chatterton, L.T., Radiation Damage in Crystals, Menthuen & Co., London, pp 23-24, 27-29, 141 (1965).
12. Seitz, F., and Koehler, J.S., "Displacement of Atoms During Irradiation," in Solid State Physics Vol. 2, Ed. by Seitz and Turnbull, Academic Press, New York, pp 309-311, 313, 321, 378-379 (1956).
13. Whaling, W., Encyclopedia of Physics, S. Fluegge Ed., Springer-Verlag, Berlin, 34/2, p 193 (1958).
14. Schiott, H.E., "Range Energy Relations for Low-Energy Ions," Kgl. Danske Videnskab. Selskab., Mat.-fys. Medd. 35 (No. 9), 9 (1966).

APPENDIX D

CONTENTS

<u>Section</u>		<u>Page</u>
1.0	Introduction	79
2.0	Energy to Form Single Cation Vacancy (U_1)	80
2.1	Mott and Littleton Method	80
2.1.1	Electrostatic Energy Contributions (Coulomb)	81
2.1.2	Non-Coulomb Energy Contributions	87
2.1.3	Summation of Energy Contributions	88
2.2	Tosi and Doyama Method	88
2.2.1	Energy of Unrelaxed Configuration (U_1')	88
2.2.2	Energy Decrease Upon Relaxation	89
3.0	Energy of Formation of the Relaxed Cationic Saddle-Point Configuration (U_2)	89
3.1	Energy of Unrelaxed Configuration (U_2')	91
3.1.1	Electrostatic (Coulombic) Energy Contributions	91
3.1.2	Non-Coulombic Energy Contributions	100
3.1.3	Summation of Contributions to the Energy of the Unrelaxed Saddle-Point Configuration	103
3.2	Energy Decrease Upon Relaxation ($U_2' - U_2$)	103
3.2.1	Change in Coulombic Energy Contributions - ΔU_C	104
3.2.2	Decrease in Non-Coulombic Energy (ΔU_R)	114
3.2.3	Net Energy Decrease Upon Relaxation	118
3.3	Energy of the Relaxed Configuration (U_2)	118
4.0	Energy Barrier for Cation Vacancy Migration (ΔU_r) in an Otherwise Perfect Lattice	119

APPENDIX D
ENERGY BARRIER FOR CATION VACANCY MIGRATION (ΔU_r) IN
AN OTHERWISE PERFECT LATTICE

1.0 Introduction

For energy summations in the defect lattice various Coulomb and non-Coulomb (overlap repulsion) interactions among ions and between ions and defects have been considered. Where appropriate, discrete Coulomb interactions have been considered, i.e., those involving the nearest neighbors (n.n.), next nearest neighbors (n.n.n.) etc. of the defect. Coulomb interactions involving remaining ("distant") ions have been "averaged" on a continuum basis, with electronic polarization segregated according to cations and anions and displacement polarization averaged over both types of ions.

Non-Coulomb interactions are by their nature short range effects. Hence changes in repulsive energy induced by defects (vacancies or interstitials) have been considered significant only where involving (a) nearest, next nearest, and third nearest neighbors to the defects comprising the saddle-ion configuration and (b) nearest neighbors in the single cation vacancy configuration. In both cases, overlap interactions have been treated explicitly.

Energy summation over the perfect lattice with respect to a normal lattice site is most conveniently described by a Madelung sum. Ewald¹ or Evjen² summation methods are convenient where the perfect lattice energy is to be evaluated at a position displaced from a normal lattice site.

Theoretical determination of the energy barrier for migration (ΔU_r) of a cation vacancy in an otherwise perfect crystal has involved two major steps as follows, patterned after the work indicated:

- 1.0 Evaluate the energy (work) U_1 to extract a single cation from a perfect crystal lattice. Method of Mott and Littleton³ with refinements by Tosi, Fumi, and co-workers^{4,5,6,7} or alternate technique by Tosi and Doyama.⁸
- 2.0 Evaluate the energy U_2 to "extract from a perfect crystal two next nearest neighbor cations and introduce one of them into the saddle-point position between the two neighboring vacancies"⁴ which result. Method of Guccione, Tosi, and Asdente.⁴

Attention is called to the fact that the outlined procedures below are applicable to any crystal lattice type. On the other hand, specific energy terms and calculations which are presented are applicable only to a face-centered-cubic crystal lattice (FCC) containing either a single cation vacancy or a cationic saddle-point configuration.

2.0 Energy to Form Single Cation Vacancy (U_1)

2.1 Mott and Littleton Method

This method rests on a model in which the n.n. to a cation vacancy (six in the case of the cubic lattice sketched below) are treated explicitly in terms of:

(1) Coulomb interactions.

Electrostatic energy changes induced with the introduction a point charge (i. e., the cation vacancy) and resulting from polarization (electronic and displacement) and subsequent interaction between ionic and displacement dipoles and the charge-induced electric field. Also, electrostatic interactions between lattice charges.

(2) Non-Coulomb interactions.

Overlap repulsion interactions take into account displacement of n.n. ions to the cation vacancy as a result of the polarization induced by the effective charge located at this vacancy.

All other ions are treated as distant ions and averaged on a continuum basis, considered either separately as cations and anions or an average of the two species.

As presented so clearly by Bassani and Fumi (see their equations (6)), the first step involves the establishment of the outward electrostatic (F_e) and repulsive (F_r) forces acting on the six-negative n.n. (#1 through #6) in terms of a uniform explicit displacement νr_o indicated in the following sketch.

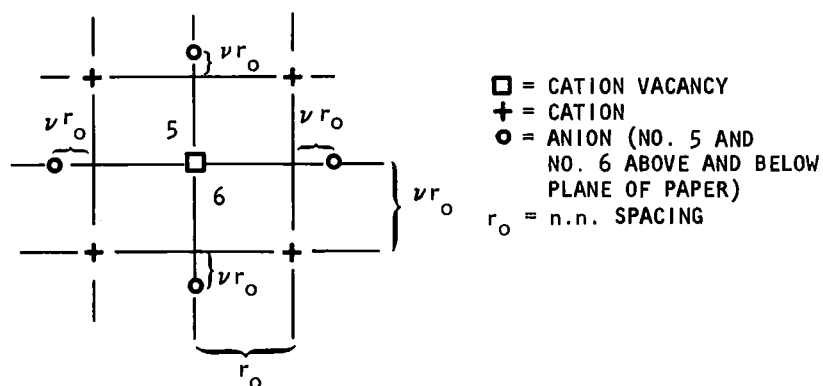


Figure D1. N.N. anion relaxation around single cation vacancy in otherwise perfect FCC lattice.

Balancing of these forces occurs at equilibrium. Hence a common solution to these two force equations (conveniently obtained graphically) yields the equilibrium displacement νr_o .

Upon establishing the value of ν and its corresponding equilibrium force value, the work done U_1 in extracting an ion (e.g., a cation) may then be formulated as the negative average of the potential energy of the cation in its normal position and in the field of the displacements and dipole moments appropriate to the vacancy.⁷ Thus for a cubic lattice one proceeds as follows:

2.1.1 Electrostatic Energy Contributions (Coulomb)

2.1.1.1 Interactions Between Lattice Charges (Monopole) - $(U_1)_C$

$$(U_1)_C = -\frac{1}{2} \left[(\text{potent. energy cation})_{\text{normal lattice}} + (\text{potent. energy cation})_{\text{distorted lattice}} \right]$$

$$= -\frac{1}{2} \left\{ -\frac{q^2}{r_o} \alpha_M + \left[-\frac{q^2}{r_o} \alpha_M + 6 \frac{q^2}{r_o} - 6 \frac{q^2}{(1+\nu) r_o} \right] \right\}$$

$$= -\frac{1}{2} \left\{ -\frac{q^2}{r_o} \alpha_M + \left[-\frac{q^2}{r_o} \alpha_M + \frac{q^2}{r_o} \left(\frac{6\nu}{1+\nu} \right) \right] \right\} \quad (D1)$$

$$= \frac{q^2}{r_o} \left(\alpha_M - \frac{3\nu}{1+\nu} \right) \quad (D2)$$

where

e = electron charge, c.g.s. units

$q = ze$ = ionic charge, c.g.s. units

α_M = Madelung sum (based on r_o) for FCC lattice

r_o = interionic spacing (n.n.) in cm

z = nuclear charge (valence)

Note that in equation (D1), the potential energy of the reference cation (i.e., taken at an origin of 0,0,0) in a normal or perfect lattice is described by the Madelung energy, $-[q^2/r_o] \alpha_M$. When the six nearest neighbor (n.n.) anions are displaced νr_o radially outwards from 0,0,0 as a result of displacement polarization (fictitiously assumed to occur with the reference cation still in place), the Madelung energy no longer correctly describes the energy of this cation. The expression in square brackets in equation (D1) contains the Madelung energy of this cation and two correction terms. The first correction term, $+6 q^2/r_o$, reduces the Madelung energy (note opposite sign) by an amount equal to the electrostatic energy contributions of the six-n.n.

anions, normally located at a distance r_o from the origin (and included in the Madelung energy as such) but in the distorted or polarized lattice no longer there. In the lattice distorted by polarization (by the electric field created upon extraction of the reference cation) the six-n.n. anions relax outwards from the origin (0,0,0) to a distance $(1 + \nu) r_o$. The electrostatic energy contributions of these n.n. ions in their new positions must be added to the Madelung energy of the reference cation and thus represent the second correction term in equation (D1), $- 6 q^2 / [(1 + \nu) r_o]$.

2.1.1.2 Interactions Between Dipoles and Electric Field Giving Rise to Dipoles (Polarization) - $(U_1)_P$

$$(U_1)_P = -\frac{1}{2} \left\{ (+q)(V_P)_{\text{normal lattice}} + (+q) \left[(V_P)_{\text{dipoles on 6-n.n. anions}} + (V_P)_{\text{all other cations}} + (V_P)_{\text{all other anions}} \right]_{\text{distorted lattice}} \right\} \quad (D3)$$

$$= -\frac{1}{2} \left\{ 0 + (q) \left[-\left(\frac{q}{r_o}\right) \frac{6m}{(1+\nu)^2} - \left(\frac{q}{r_o}\right) 6.3346 M'_+ - \left(\frac{q}{r_o}\right) 4.1977 M'_- \right] \right\} \quad (D4)$$

$$= \frac{q}{2r_o} \left[\frac{6m}{(1+\nu)^2} + 6.3346 M'_+ + 4.1977 M'_- \right] \quad (D5)$$

where

V_P = polarization-induced potential at cation site (0,0,0) by species indicated

mr_o = charge displacement in 6-n.n. due to electronic polarization, cm

$$m = \alpha_- F_e / (q^2 r_o)$$

α_- = anion polarizability, cm^3

Since no polarizing field exists in the normal lattice, there is zero induced polarization potential at the position of the reference cation (0,0,0).

The second term in the curly brackets in equation (D3) represents polarization energy contributions induced at 0,0,0. These result from interactions of the polarization-created, electronic dipoles on the six-n.n. anions with the electric field emanating from the origin which created them. The potential V induced at a point i by a dipole may be expressed:

$$V = \frac{\vec{\mu} \cdot \vec{r}}{r^3} \quad \begin{array}{c} \text{m} \\ \text{+q} \quad \text{-q} \\ \theta \\ \vec{r} \\ i \end{array} \quad (D6)$$

$$V = \frac{|\mu| |r \cos \theta|}{r^3} = \left| \frac{\mu \cos \theta}{r^2} \right| \quad (D7)$$

where

$\vec{\mu}$ = dipole moment

\vec{r} = vector separation between point and center of dipole

θ = angle between \vec{r} and $\vec{\mu}$, increasing angle measured from the dipole arrow tip counterclockwise.

$||$ = scalar quantity

In the case of the potential induced at 0,0,0 by an induced electronic dipole on a n.n. anion, $\theta = 0$. Also recalling that n.n. separation in the distorted lattice is $(1+\nu)r_o$, one may obtain the dipole-induced potential at 0,0,0 from equation (D7) as follows:

$$\left[V_P(0, 0, 0) \right]_{\text{by one-n.n.}} = - \frac{\mu_{\text{n.n.}} \cos(0)}{\left[(1+\nu) r_o \right]^2} = - \frac{\mu_{\text{n.n.}}}{(1+\nu)^2 r_o^2} \quad (\text{D8})$$

It can be shown that the negative sign arises from the fact the dipole is on a negative ion. The electronic dipole moment on any ion may be defined as follows (see sketch above):

$$\mu = \text{charge} \times \text{separation} = (q) (mr_o) \quad (\text{D9})$$

Substituting (D9) in (D8) and accounting for all six-n.n. yields:

$$\left[V_P(0, 0, 0) \right]_{6\text{-n.n.}} = - \frac{6 q m r_o}{(1+\nu) r_o^2} = - \frac{q}{r_o} \cdot \frac{6m}{(1+\nu)^2} \quad (\text{D9})$$

The energy induced by this potential at the origin on the cation at the origin (+q) is then: $(U_1)_P = (+q) V_P$, as shown in equation (D4).

The third term in equation (D3) represents the polarization energy contributions to the reference cation by all other lattice cations. Similarly the fourth term represents the contributions by all the lattice anions to the reference cation with the exception of the six-n.n. anions. These contributions are formulated according to Mott and Littleton (see their equations (3.1), (3.2), and (3.3)) and summed according to Jones and Ingram⁹ for a cubic lattice where the separation distance between the origin and any lattice point is raised to the fourth power. This latter arises from the fact that:

$$\mu \text{ (distant cation or anion)} = f (r^{-2})$$

$$V \text{ (at origin by distant ion)} = f (\mu / r^2)$$

$$\therefore V = f (r^{-4})$$

The parameters M_+^i and M_-^i contain ratios of the total ion polarizability to that of the molecule, for the cation and anion, respectively. These parameters are based on the fundamental relationship between the electric field \vec{E} in a dielectric, the displacement field \vec{D} , and the total polarization \vec{P} of the dielectric. Thus one may write the following expression:

$$\vec{E} = \vec{D} - 4\pi \vec{P} \quad (\text{D11})$$

In a spherical system the directions of \vec{E} , \vec{D} , and \vec{P} are the same; and hence (D11) may be rewritten in terms of scalars:

$$E = D - 4\pi P \quad (\text{D12})$$

By definition, E (vacuum) = D = force/unit charge = q/r^2 , where r = separation between the charge q and the point where its field is measured. In a dielectric medium E must be less than D , by an amount proportional to the dielectric constant i.e., the static or low frequency value κ in this case where ions in the continuum are considered to undergo physical displacement. Thus we may write: $E = q/(\kappa r^2)$. Substitution of the values of D and E from above and rearranging yields a value of P as follows:

$$P = \left(\frac{q}{r^2} - \frac{q}{\kappa r^2} \right) \frac{1}{4\pi} = \frac{1}{4\pi} \left(1 - \frac{1}{\kappa} \right) \frac{q}{r^2} \quad (D13)$$

It seems reasonable to assume that this expression for the total polarization of the continuum P may be apportioned between the total polarization (i.e., electronic and displacement) of cations P_+ and of anions P_- . We may express this apportionment as follows:

$$P = f_+ P_+ + f_- P_- \quad (D14)$$

where

f_+, f_- = fraction of continuum polarization assignable to cations and anions, respectively

Note that the smallest volume representative of the continuum is that associated with a molecule (i.e., a cation-anion pair) and equals $2r_o^3$. In terms of electronic polarizability of the ions, α_+ or α_- , and displacement polarizability α of the medium, the total polarizability of the molecule is equal to the sum: $\alpha_+ + \alpha_- + 2\alpha$. Thus the partition fractions may be written as ratios of total ionic polarization to total molecular polarization as follows:

$$f_+ = \frac{\alpha_+ + \alpha}{\alpha_+ + \alpha_- + 2\alpha} \quad (D15)$$

$$f_- = \frac{\alpha_- + \alpha}{\alpha_+ + \alpha_- + 2\alpha} \quad (D16)$$

Since the total polarization of the continuum is by definition the total dipole moment per unit volume and also since both \vec{P} and the dipole vector $\vec{\mu}$ are in the same direction, we may write the following scalar expression for one molecule of the continuum:

$$P = \mu_{\text{mol.}} / (2 r_o^3)$$

or

$$\mu_{\text{mol.}} = P 2 r_o^3 \quad (D17)$$

Substituting from (D15), (D16), and (D14) into (D17) yields:

$$\mu_{\text{mol.}} = 2 r_o^3 \left[\frac{\alpha_+ + \alpha}{\alpha_+ + \alpha_- + 2\alpha} \right] P + 2 r_o^3 \left[\frac{\alpha_- + \alpha}{\alpha_+ + \alpha_- + 2\alpha} \right] P \quad (\text{D18})$$

Substituting the value of P from equation (D13) into (D18) yields:

$$\begin{aligned} \mu_{\text{mol.}} &= r_o^3 \left[\frac{\alpha_+ + \alpha}{1/2 (\alpha_+ + \alpha_-) + \alpha} \right] \frac{1}{4\pi} \left(1 - \frac{1}{\kappa} \right) \frac{q}{r^2} \\ &\quad + r_o^3 \left[\frac{\alpha_- + \alpha}{1/2 (\alpha_+ + \alpha_-) + \alpha} \right] \frac{1}{4\pi} \left(1 - \frac{1}{\kappa} \right) \frac{q}{r^2} \\ &= M_+^1 r_o^3 \left(\frac{q}{r^2} \right) + M_-^1 r_o^3 \left(\frac{q}{r^2} \right) \end{aligned} \quad (\text{D19})$$

where by definition

$$M_+^1 = \frac{1}{4\pi} \left(1 - \frac{1}{\kappa} \right) \frac{\alpha_+ + \alpha}{1/2 (\alpha_+ + \alpha_-) + \alpha}$$

$$M_-^1 = \frac{1}{4\pi} \left(1 - \frac{1}{\kappa} \right) \frac{\alpha_- + \alpha}{1/2 (\alpha_+ + \alpha_-) + \alpha}$$

r = separation between the reference charge and a reference molecule in the continuum

κ = static dielectric constant (i.e., measured at frequencies less than the lattice vibration frequency, $\sim 10^{13} \text{ sec}^{-1}$, so that ionic displacement is able to take place)

α_+ = electronic polarizability of cation in the crystal, 10^{-3} cm^3

α_- = electronic polarizability of anion in the crystal, 10^{-3} cm^3

$\alpha = q^2/p$ = displacement polarizability of crystal

p = restoring force per unit displacement which opposes ion displacement resulting from polarization

Since $\mu_{\text{mol.}} = \mu_+ + \mu_-$, it may be seen by inspection of equation (D19) that the total dipole moment of a cation (μ_+) or an anion (μ_-) in the continuum may be expressed as follows:

$$\mu_+ = M_+^i r_o^3 \left(\frac{q}{r^2} \right) \quad (\text{D20})$$

$$\mu_- = M_-^i r_o^3 \left(\frac{q}{r^2} \right) \quad (\text{D21})$$

The value of p , the restoring force/unit displacement, is obtained by differentiation of the change in energy per ion pair caused by overlap repulsion when the ions are displaced by polarization. When the Born-Mayer expression for overlap repulsion energy,

$$U_R(r) = b C_{+-} \exp \left(\frac{r_+ + r_- - r}{\rho} \right)$$

is used, the value of p is found to be:

$$p = 4 b \left(\frac{1}{\rho^2} - \frac{2}{\rho r_o} \right) \exp \left(\frac{r_+ + r_- - r_o}{\rho} \right) \quad (\text{D22})$$

where:

b = Born-Mayer constant, ergs

ρ = Born-Mayer constant, cm

r_+, r_- = Goldschmidt values of ionic radii

C_{+-} = Pauling ionic dependence factor = 1.0 for overlap repulsion between ions of opposite sign

2.1.2 Non-Coulomb Energy Contributions

The Born-Mayer expression for overlap repulsion energy between ions has been used to describe the non-coulomb energy contributions. This has been found satisfactory for the case where $r \geq r_o$, the situation which prevails here where the work to form a single cation vacancy in a perfect lattice is to be determined.

As with previously discussed energy contributions, the overlap repulsion contribution to the reference cation is taken as the negative average of the potential energies before and after displacement. Only that repulsion between the reference cation and its six-n.n. anions is considered significant as indicated in the following expression:

$$\begin{aligned}
(U_1)_R &= -\frac{1}{2} \left\{ (\text{cation energy})_{\text{lattice normal}} + (\text{cation energy})_{\text{lattice distorted}} \right\} \\
&= -\frac{1}{2} \left\{ 6 b C_{+-} \exp \left[\frac{r_+ + r_- - r_o}{\rho} \right] + 6 b C_{+-} \exp \left[\frac{r_+ + r_- - (1+\nu) r_o}{\rho} \right] \right\} \\
&= -3 b C_{+-} \exp \left[\frac{r_+ + r_- - r_o}{\rho} \right] \left[1 + \exp (-\nu r_o / \rho) \right] \tag{D23}
\end{aligned}$$

2.1.3 Summation of Energy Contributions

The Coulomb contributions, equations (D2) and (D5), and the non-Coulomb contributions, equation (D23) may now be added to yield U_1 , the energy to form a cation vacancy in perfect FCC lattice as follows:

$$U_1 = (U_1)_C + (U_1)_P + (U_1)_R \tag{D24}$$

2.2 Tosi and Doyama Method⁸

This procedure is analogous to that used to obtain saddle point energy in a relaxed configuration, i.e., one in which equilibrium displacement has occurred. Three basic steps are involved: (1) formulation of the energy of the unrelaxed lattice after cation extraction, (2) determination of the energy released upon relaxation of the crystal around the cation vacancy and (3) subtraction of (2) from (1) to yield the energy of the relaxed lattice with a single cation vacancy. These first two steps are outlined as follows:

2.2.1 Energy of Unrelaxed Configuration (U_1')

2.2.1.1 Madelung energy

2.2.1.2 Polarization (electronic only)

- 2.2.1.1.1 Of nearest neighbors (n.n.) due to effective charge on the vacancy
- 2.2.1.1.2 Of nearest neighbors due to dipoles on nearest neighbors and all other more distant ions
- 2.2.1.1.3 Of non-nearest neighbors due to effective charge on the vacancy
- 2.2.2 Energy Decrease Upon Relaxation
 - 2.2.2.1 Coulomb energy between nearest neighbors
 - 2.2.2.2 Coulomb interaction with external lattice
 - 2.2.2.3 Polarization
 - 2.2.2.3.1 Of nearest neighbors with effective charge at the vacancy
 - 2.2.2.3.2 Of nearest neighbors with dipoles on nearest neighbors
 - 2.2.2.3.3 Of nearest neighbors due to displacement of nearest neighbors
 - 2.2.2.4 Non-Coulomb relaxation of the 30 "nearest neighbors" to the relaxing ions (i.e., the six displaced nearest neighbors to the vacancy) and of the 48 "next nearest neighbors" to these displaced ions
 - 2.2.2.4.1 Polarization displacement included explicitly in overlap repulsion terms
 - 2.2.2.4.2 Alternate solution with Born-Mayer-Verwey potential for all interactions where the separation $< r_0$ (inter-ionic spacing)

3.0 Energy of Formation of the Relaxed Cationic Saddle-Point Configuration (U_2)

Computation of the energy barrier for migration (ΔU_r) of a single vacancy in an otherwise perfect lattice requires evaluation of the lattice potential (or lattice energy) along certain paths between normal lattice positions. Although imposing some limitation on ultimate usefulness, the complexity of the calculation dictated selection of one of the simplest lattices as a basis for initial calculations, namely the face centered cubic lattice. In this lattice, the pertinent cation migration path is a diagonal one from a $0,0,0$ to a $1,1,0$ position and passing through the saddle-point at $1/2, 1/2, 0$. Schematically, this may be indicated as follows:

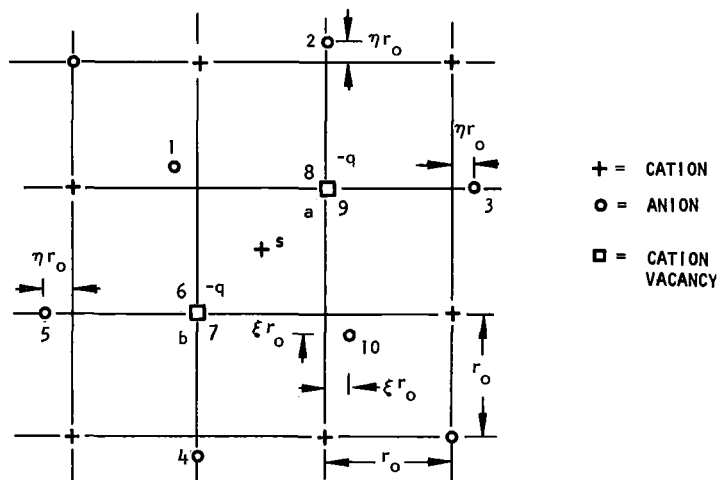


Figure D2. Relaxed saddle-point configuration in otherwise perfect FCC lattice.

Cation movement is indicated as occurring from normal lattice site b (0, 0, 0) to vacancy a (1, 1, 0), with the cation shown in the saddle-point position $(1/2, 1/2, 0)$. Cation vacancy migration, of course, occurs in the opposite direction.

Note that migration of a lattice cation is based on an otherwise perfect lattice containing a cation vacancy. As the lattice cation moves to the saddle point configuration, critical to the ΔU_r value, three defect states result, namely cation vacancies v_a and v_b and the lattice cation at the saddle-point. The 10 nearest neighbors to these three defects are numbered and shown in the above sketch in their relaxed positions. The displacement polarization resulting in the ion displacements shown (i.e., $\sqrt{2} \xi r_o$ for #1 and #10, ηr_o for ions #2 through #9) are attributed to the combined electric field of the three defects. Anions #6 and #8 are above and #7 and #9 are below the plane of the paper. Shown without numbers are the next nearest neighbors to the defects and some of the third nearest neighbors. Certain of these are above and below the plane of the paper, although not so indicated. Attention is called to the fact that in the discussions which pertain to the unrelaxed lattice anions #1 through #10 are considered to reside at their normal sites.

The energy of the crystal in the relaxed saddle-point configuration (relative to the perfect crystal) is obtained by adding the decrease in energy of the crystal as a result of displacement relaxation to the energy of the crystal in the unrelaxed saddle-point configuration (relative to the perfect crystal). The steps involved in such a computation together with terms applicable to a FCC lattice are outlined below.

3.1 Energy of Unrelaxed Configuration (U_2^1)

3.1.1 Electrostatic (Coulombic) Energy Contributions

3.1.1.1 Interactions Between Lattice Charges (Monopole) - (U_2^1)_C

Computation of interaction energies for the case of the unrelaxed saddle-point configuration is aided by reference to figure D2 for the condition $\eta = 0$, $\xi = 0$. This condition imposes the requirement that the 10-n.n.'s to the three defects are held at their normal lattice sites, i.e., they are not permitted to relax to displaced positions.

The electrostatic potential energy of a cation (or anion) at a normal lattice position in a perfect crystal is $-\frac{q^2}{r_o} \alpha_M$. When one cation (say at 0, 0, 0) is extracted from the lattice work must be done; hence the energy of the lattice is increased by $+\frac{q^2}{r_o} \alpha_M$.

When a second cation (say at 1, 1, 0) is extracted, work must be done against the Coulombic energy this cation would have in a perfect crystal (= the Madelung energy = $-\frac{q^2}{r_o} \alpha_M$) plus the additional energy acquired when its potential well was deepened $-\frac{q}{\sqrt{2} r_o}$ as a consequence of extracting the first cation at an ionic separation of $\sqrt{2} r_o$. Thus this additional energy is $-\frac{(q)(+q)}{\sqrt{2} r_o}$. Therefore with the 0, 0, 0 cation missing, the energy of the 1, 1, 0 cation is effectively: $-\frac{q^2}{r_o} \alpha_M - \frac{q^2}{\sqrt{2} r_o}$. Extraction of this second cation thus increases the Coulombic energy of the crystal by an amount $= q^2/r_o (\alpha_M + 1/\sqrt{2})$.

The Coulombic interaction energy of the saddle ion with a perfect lattice is zero. However, in the saddle-point configuration when the two-n.n. cations (at 0, 0, 0 and 1, 1, 0) are removed, the Coulombic interaction between the n.n. anions (1, 0, 0 and 0, 1, 0) and the saddle cation (1/2, 1/2, 0) is released. Since the separation in both cases is $r = (\sqrt{2}/2) r_o$, this cation-anion interaction is

$$(2) \frac{(+q)(-q)}{(\sqrt{2}/2) r_o} = -2 \frac{q^2}{(\sqrt{2}/2) r_o}$$

and thus represents a decrease in Coulombic energy of the crystal.

The above three terms represent the monopole contributions to the lattice energy relative to a perfect crystal in the unrelaxed saddle-point configuration. They may be summed as follows:

$$\begin{aligned}
(U_2')_C &= \frac{q^2}{r_o} \alpha_M + \frac{q^2}{r_o} \left(\alpha_M + \frac{1}{\sqrt{2}} \right) - \frac{2 q^2}{(\sqrt{2}/2) r_o} \\
&= \frac{q^2}{r_o} \left(2 \alpha_M + \frac{1}{\sqrt{2}} - \frac{2}{\sqrt{2}/2} \right)
\end{aligned} \tag{D25}$$

3.1.1.2 Polarization - $(U_2')_P$

These energy contributions result from the electrostatic interactions between the dipoles induced on the lattice ions (by the electric fields introduced by the charged defects) and these same electric fields. Separate fields radiate from the saddle ion charge (+q) and the "equivalent" charge (-q) hypothetically located at each of the two vacancies.

In this case, where the saddle ion configuration is considered to exist in an unrelaxed lattice, the 10-nearest neighbor (n.n.) anions to the three defects are considered electronically polarized but not displaced from normal lattice sites (i.e., unrelaxed). All other ions (non-nearest neighbor cations and anions) are considered to undergo both electronic and displacement (physical) polarization. This displacement polarization of distant ions is not considered as relaxable in order to reduce complexity. The above basis should be kept in mind when referring to figure D2 in connection with this section.

The calculation procedure is then as follows:

First - calculate the discrete, electronic polarization energy contribution of the 10-n.n. anions as induced by the three defects (s, v_a , v_b).

Second - calculate on a continuum basis total polarization of all non-n.n. anions and all distant cations induced by the three defects.

3.1.1.2.1 Electronic Polarization of 10-Nearest Neighbor Anions by the Three Defects

The discrete energy contribution by a n.n. anion in a rigid lattice arises from the interaction between its induced dipole moment $\vec{\mu}$ and the electric field \vec{E}_O giving rise to it as follows:

$$(U_P)_{n.n.} = -1/2 \vec{E}_O \cdot \vec{\mu} \tag{D26}$$

Both \vec{E}_O and $\vec{\mu}$ are always in the same direction. Also the dipole induced on an anion by \vec{E}_O may be expressed in terms of the anion polarizability α_- : $\vec{\mu} = \alpha_- \vec{E}_O$. On this basis equation (D26) may be transformed to the following:

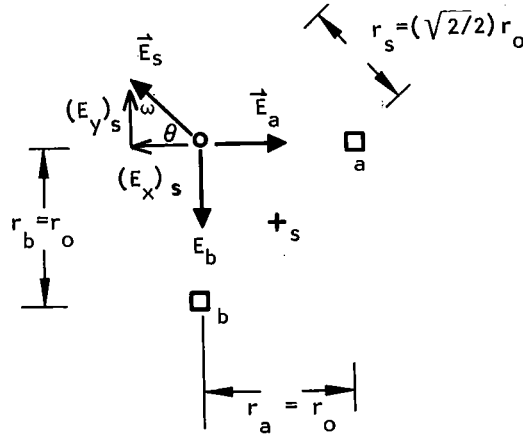
$$(U_P)_{\text{anion}}^{\text{n.n.}} = -1/2 \vec{E}_O \cdot \alpha_- \vec{E}_O = -1/2 \alpha_- \vec{E}_O^2 \quad (\text{D27})$$

where

$$\vec{E}_O^2 = \left(\sum E_x^2 \right) \vec{i} + \left(\sum E_y^2 \right) \vec{j} + \left(\sum E_z^2 \right) \vec{k} \quad (\text{D28})$$

Labeling the fields from the saddle ion and the vacancies a and b as \vec{E}_s , \vec{E}_a , and \vec{E}_b , respectively, these fields acting to polarize anion #1 are sketched as follows for the unrelaxed lattice:

Anion #1



$$\sum E_y = (E_y)_s + (E_y)_b = \left(\frac{q_s}{r_s^2} \right) \cos \omega - \frac{q_b}{r_b^2} \quad (\text{D29})$$

$$\sum E_x = - (E_x)_s + (E_x)_a = - \frac{q_s}{r_s^2} \cos \theta + \frac{q_a}{r_a^2} \quad (\text{D30})$$

where

pos. y-components are taken upwards; neg.-downwards

pos. x-components are taken toward right; neg.-toward left

$$\left.
\begin{aligned}
\omega &= \theta = \pi/4 \\
r_a &= r_b = r_o \\
r_s &= (\sqrt{2}/2) r_o \\
q_s &= q_a = q_b = q \text{ (where } z_{\text{cation}} = z_{\text{anion}})
\end{aligned}
\right\} \quad (D31)$$

Substituting from (D31) into (D29) and (D30) yields:

$$\Sigma E_y = \frac{q}{\left[(\sqrt{2}/2) r_o \right]^2} \frac{1}{\sqrt{2}} - \frac{q}{r_o^2} = \frac{q}{r_o^2} (\sqrt{2} - 1) \quad (D32)$$

$$\Sigma E_x = - \frac{q}{\left[(\sqrt{2}/2) r_o \right]^2} \frac{1}{\sqrt{2}} + \frac{q}{r_o^2} = - \frac{q}{r_o^2} (\sqrt{2} - 1) \quad (D33)$$

Thus

$$\begin{aligned}
\Sigma E_x &= - \Sigma E_y \\
\therefore \Sigma E_x^2 &= \Sigma E_y^2
\end{aligned} \quad (D34)$$

Although an approximation, ΣE_z is taken as zero. Substituting (D34) into (D28) yields:

$$\vec{E}_o^2 = 2 \Sigma E_x^2 \quad (D35)$$

Substituting (D35) into (D27) yields:

$$(U_P)_{\text{anion}} = - \frac{1}{2} \alpha_- \left(2 \Sigma E_x^2 \right) \quad (D36)$$

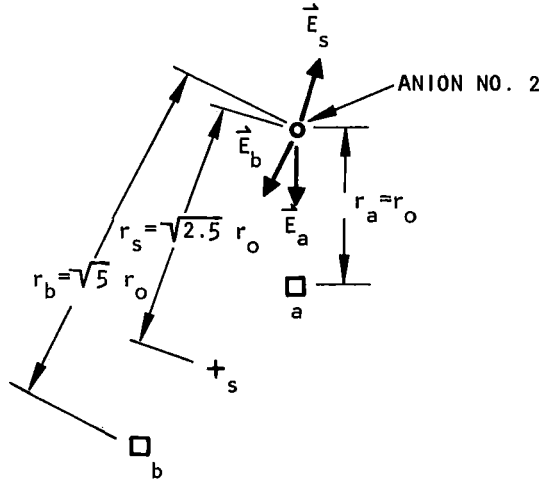
#1

Substituting the value of ΣE_x from equation (D33) into (D36), and noting from figure D2 that anions #1 and #10 because of symmetry have equivalent interactions, yields:

$$\begin{aligned}
(U_P')_{\substack{\text{anions} \\ \#1 \text{ and} \\ \#10}} &= 2 \left\{ - (1/2) \alpha_- (2) \left[\frac{q}{r_o^2} (\sqrt{2} - 1) \right]^2 \right\} \\
&= - 2 \alpha_- \frac{q^2}{r_o^4} (0.414)^2 = - 0.344 \alpha_- \frac{q^2}{r_o^4} \quad (D37)
\end{aligned}$$

It will be observed that anions #2, #3, #4, and #5 are symmetrically located with respect to defects \underline{s} , v_a , and v_b . Consideration of anion #2 in its unrelaxed position yields the following field vector diagram at #2:

Anion #2



Again we assume \underline{s} to lie in the plane of the paper and thus consider no z-component to the defect-induced field at anion #2. Using the expressions (D27) and (D28) we have:

$$(U_P')_{\substack{\text{anion} \\ \#2}} = - 1/2 \alpha_- \left[\Sigma E_x^2 + \Sigma E_y^2 \right] \quad (D38)$$

Using the same procedure as for anion #1, these x- and y-components of the defect field vectors at the unrelaxed position #2 are found to be:

$$\begin{aligned}
\Sigma E_x &= \frac{q}{r_o^2} \left[(E_x)_s - (E_x)_b \right] = \frac{q}{r_o^2} \left[\frac{0.5}{(2.5)^{3/2}} - \frac{1}{5^{3/2}} \right] \\
\Sigma E_y &= \frac{q}{r_o^2} \left[(E_y)_s - (E_y)_a - (E_y)_b \right] = \frac{q}{r_o^2} \left[\frac{1.5}{(2.5)^{3/2}} - 1 - \frac{2}{5^{3/2}} \right] \quad (D39)
\end{aligned}$$

Substitution of (D39) values into (D38) and multiplying by $\frac{4}{r_o}$ to account for the four symmetrical anions yields:

$$\begin{aligned}
 (U_P')_{\substack{\text{anions} \\ \#2, 3, 4, \\ \text{and } 5}} &= 4 \left\{ -\frac{1}{2} \alpha - \frac{q^2}{r_o^4} \left[\left(\frac{0.5}{(2.5)^{3/2}} - \frac{1}{5^{3/2}} \right)^2 + \left(\frac{1.5}{(2.5)^{3/2}} - 1 - \frac{2}{5^{3/2}} \right)^2 \right] \right\} \\
 &= -1.282 \alpha - \frac{q^2}{r_o^4} \quad (D40)
 \end{aligned}$$

Of the 10-n.n. anions to three defects, six have been accounted for (i.e., #1 through 5 and #10). The remaining four anions (#6 through #9) are seen in figure D2. It will be observed that the defect-induced field is the same at each of these four in the unrelaxed lattice. By the same procedure as above, that of summing the squares of the appropriate defect field components at a given ion position, one obtains:

$$\begin{aligned}
 (U_P')_{\substack{\text{anions} \\ \#6, 7, 8, \\ \text{and } 9}} &= 4 \left\{ -\frac{1}{2} \alpha - \frac{q^2}{r_o^4} \left[\left(-\frac{0.5}{1.5^{3/2}} + \frac{1}{3^{3/2}} \right)^2 + \left(-1 + \frac{1}{1.5^{3/2}} - \frac{1}{3^{3/2}} \right)^2 \right] \right\} \\
 &= -0.8636 \alpha - \frac{q^2}{r_o^4} \quad (D41)
 \end{aligned}$$

The energy contributions of the 10-n.n. anions, resulting from polarization by the defect field, may now be obtained by a summation of equations (D37), (D40), and (D41) as follows:

$$\begin{aligned}
 (U_P')_{\substack{10\text{-n.n.} \\ \text{anions}}} &= \alpha - \frac{q^2}{r_o^4} [-0.344 - 1.282 - 0.8636] \\
 &= -2.490 \alpha - \frac{q^2}{r_o^4} \quad (D42)
 \end{aligned}$$

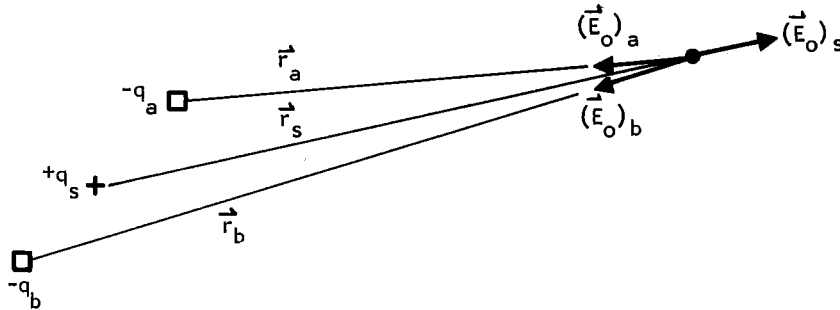
3.1.1.2.2 Electronic and Displacement Polarization of All Non-Nearest Neighbor Cations and Anions by the Three Defects

The scalar expression given in equation (D20) for the total dipole moment (electronic and displacement) of a cation in the dielectric continuum is as follows:

$$\mu_+ = M_+^i r_o^3 \left(\frac{q}{r^2} \right) \quad (D20)$$

where polarization of the continuum results from the single charged defect, $+q$. Where several charged defects (as in this case) act to polarize the dielectric, calculation of their individual contributions to polarization is more complicated. Fortunately it has been found that, although not justified on first principles, μ_+ (or μ_-) may be calculated by treating the factor (q/r^2) in equation (D20) as the combined electric field of the various charged defects at a given cation in the continuum. This combined field is obtained by summation of individual field vectors.

The "discrete" field vectors, which for purposes of calculation, are considered as generated by the charged defects (q_s , $-q_a$, $-q_b$) and result in polarization of a cation in the dielectric, may be sketched as follows:



With reference to the defect s in the saddle configuration, this total dipole moment on a distant cation may be expressed vectorially as follows:

$$(\mu_+)_s = M_+^i r_o^3 \left(\frac{q_s}{r_s^2} \hat{r}_s \right) \quad (D43)$$

where

r_s = separation between a given distant cation and the saddle ion of charge q_s .

\hat{r}_s = unit vector in r_s direction = $\vec{r}_s / |r_s|$

The vector field $(\vec{E}_O)_s$ induced by q_s at the distant cation may be expressed as follows:

$$(\vec{E}_O)_s = \frac{+q_s}{r_s^2} \hat{r}_s \quad (D44)$$

Summing the field contributions by the three defects at the position of a given distant cation yields:

$$\Sigma \vec{E}_O = \frac{q_s}{r_s^2} \hat{r}_s - \frac{q_a}{r_a^2} \hat{r}_a - \frac{q_b}{r_b^2} \hat{r}_b \quad (D45)$$

$$\Sigma \vec{\mu}_+ = M_+^+ r_o^3 \left[\frac{q_s}{r_s^2} \hat{r}_s - \frac{q_a}{r_a^2} \hat{r}_a - \frac{q_b}{r_b^2} \hat{r}_b \right] \quad (D46)$$

From equation (D26) we have:

$$(U_P)_{\text{one distant cation}} = -\frac{1}{2} \Sigma \vec{E}_O \cdot \Sigma \vec{\mu}_+ \quad (D47)$$

Substituting the sums from (D45) and (D46) into (D47) yields:

$$(U_P)_{\text{one distant cation}} = -\frac{1}{2} M_+^+ r_o^3 \left[\frac{q_s^2}{r_s^4} \hat{r}_s \cdot \hat{r}_s - 2 \frac{q_s q_a}{r_s^2 r_a^2} \hat{r}_s \cdot \hat{r}_a + \frac{q_a^2}{r_a^4} \hat{r}_a \cdot \hat{r}_a \right. \\ \left. - 2 \frac{q_s q_b}{r_s^2 r_b^2} \hat{r}_s \cdot \hat{r}_b + 2 \frac{q_a q_b}{r_a^2 r_b^2} \hat{r}_a \cdot \hat{r}_b + \frac{q_b^2}{r_b^4} \hat{r}_b \cdot \hat{r}_b \right] \quad (D48)$$

Since by definition we have:

$$\hat{r}_s \cdot \hat{r}_a = \frac{\vec{r}_s}{|r_s|} \cdot \frac{\vec{r}_a}{|r_a|} = \frac{|r_s| |r_a| \cos \theta_{sa}}{|r_s| |r_a|} = \cos \theta_{sa} \quad (D49)$$

Similarly:

$$\hat{r}_s \cdot \hat{r}_b = \cos \theta_{sb}; \quad \hat{r}_a \cdot \hat{r}_b = \cos \theta_{ab} \quad (D50)$$

By symmetry (see above sketch of field vectors) we have:

$$\left. \begin{aligned} \sum 1/r_a^4 &= \sum 1/r_b^4; & \sum 1/\left(r_s^2 r_a^2\right) &= \sum 1/\left(r_s^2 r_b^2\right); \\ \cos \theta_{sa} &= \cos \theta_{sb} \end{aligned} \right\} \quad (D51)$$

Further note that:

$$\left. \begin{aligned} \hat{r}_s \cdot \hat{r}_s &= 1; & \hat{r}_a \cdot \hat{r}_a &= 1; & \hat{r}_b \cdot \hat{r}_b &= 1 \\ q_s &= q_b = q_a = |q| \quad (\text{the appropriate signs were} \\ & \quad \text{assigned in (D45) and (D46)}) \end{aligned} \right\} \quad (D52)$$

Substitution of appropriate values from expressions (D49) through (D52) into (D48) yields for all distant cations:

$$(U_P)_{\text{all distant cations}} = -\frac{1}{2} M_+^1 r_o^3 \left[\sum \frac{q^2}{r_s^4} - \sum \frac{4 q^2 \cos \theta_{sa}}{r_s^2 r_a^2} + \sum \frac{2 q^2 \cos \theta_{ab}}{r_a^2 r_b^2} + \sum \frac{2 q^2}{r_a^4} \right] \quad (D53)$$

The scalar separation values may be expressed in units of r_o and the pure members, ℓ_s , ℓ_a , ℓ_b , as follows:

$$r_s = \ell_s r_o; \quad r_a = \ell_a r_o; \quad r_b = \ell_b r_o \quad (D54)$$

Substituting these values from (D54) into (D53) and removing a common factor $2 q^2/r_o^4$ from within the square brackets yields:

$$(U_P)_{\text{distant cations}} = -M_+^1 \frac{q^2}{r_o} \left[1/2 \sum \frac{1}{\ell_s^4} - 2 \sum \frac{\cos \theta_{sa}}{\ell_s^2 \ell_a^2} + \sum \frac{\cos \theta_{ab}}{\ell_a^2 \ell_b^2} + \sum \frac{1}{\ell_a^4} \right] \quad (D55)$$

Evaluation of the lattice sums shown in brackets in (D55) has been carried out by Guccione, et al., to yield a value of 2.441. Thus equation (D55) may be expressed as follows:

$$(U_P')_{\text{all distant cations}} = -\frac{q^2}{r_o} \left[2.441 M_+^{\prime} \right] \quad (D56)$$

In a similar manner, U_P' (non-n.n. anions) can be evaluated. Guccione, et al., report this value as follows:

$$(U_P')_{\text{all non-n.n. anions}} = -\frac{q^2}{r_o} \left[1.755 M_-^{\prime} \right] \quad (D57)$$

3.1.1.2.3 Sum of Polarization Terms

The combined polarization energy contributions from the undisplaced 10-n.n. anions (equation D42) and from the remaining, unrelaxably-displaced anions and cations in the continuum (equations (D56) and (D57)) may be summed as follows:

$$(U_2')_P = -2.490 \alpha - \frac{q^2}{r_o} - \frac{q^2}{r_o} \left[2.441 M_+^{\prime} + 1.755 M_-^{\prime} \right] \quad (D58)$$

3.1.2 Non-Coulombic Energy Contributions

Overlap repulsion is determined on the basis of the Born-Mayer (B-M) expression (see section 2.1.2):

$$U(r) = b C_{+-} \exp \left[(r_+ + r_-)/\rho \right] \exp (-r/\rho) \quad (D59)$$

for those cases where $r \geq r_o$. The constants b and ρ are evaluated from compressibility data for a given crystal lattice. The Pauling ionic dependence factor C is as follows:

$$C = 1 + \frac{z_i}{n_i} + \frac{z_j}{n_j} \quad (D60)$$

where

$$z_i, z_j = \text{nuclear charge on interaction ions}$$

$$n_i = +8$$

Taking MgO as an example:

$$\left. \begin{aligned} \text{Mg}^{2+} - \text{Mg}^{2+} \text{ repulsive interaction} &= C_{++} = 1 + \frac{(+2)}{(+8)} + \frac{(+2)}{(+8)} = 1.5 \\ \text{Mg}^{2+} - \text{O}^{2-} \text{ repulsive interaction} &= C_{+-} = 1 + \frac{(+2)}{(+8)} + \frac{(-2)}{(+8)} = 1.0 \\ \text{O}^{2-} - \text{O}^{2-} \text{ repulsive interaction} &= C_{--} = 1 + \frac{(-2)}{(+8)} + \frac{(-2)}{(+8)} = 0.50 \end{aligned} \right\} \quad (\text{D61})$$

For those cases where overlap repulsion is to be evaluated between ions separated by a distance $r < r_0$, the Born-Mayer expression is too "soft." In these cases only, the harder Born-Mayer-Verwey (B-M-V) expression for overlap repulsive interaction energy has been used, having been found to be more correct. The B-M-V expression is as follows:

$$U_{\text{BMV}}(r) = A + B r^{-12} \quad (\text{D62})$$

Rather than direct evaluation of B-M-V constants A and B from compressibility data, a short-cut was taken which effectively makes use of such data in the form of the B-M constants. It is assumed that at equilibrium in the perfect lattice (i.e., $r = r_0$), the B-M and B-M-V energy and force (energy derivative) expressions are equivalent as follows:

$$A + B r^{-12} = b C_{+-} \exp \left[(r_+ + r_-)/\rho \right] \exp (-r/\rho) \quad (\text{D63})$$

$$-12 B r^{-13} = (b/\rho) C_{+-} \exp \left[(r_+ + r_-)/\rho \right] \exp (-r/\rho) \quad (\text{D64})$$

Using equation (D64) and given values of b , ρ , C_{+-} , r_+ , and r_- , a value of B may be obtained for the special case of $r = r_0$. With this value of B and the same constants, a value of A may be obtained at $r = r_0$ from equation (D63). Note that, in the repulsive interactions considered important to the unrelaxed saddle-point configuration (see below), only the interaction between the saddle ion and its 2-n.n. anions (at a separation of $\sqrt{2}/2 r_0$) required use of the B-M-V expression.

Regardless of which overlap repulsion energy expression is used, it is applied to the presumably undistorted lattice in the vicinity of the saddle-point cation. As shown in Guccione, et al., (see their equation (2)), included are repulsive interactions involving the saddle ion as follows:

(1) Cation and Anion

- (a) Saddle cation and 2-n.n. anions (note: the dominant term)
- (b) Saddle cation and 4-anions n.n. to v_a and v_b (above and below)
- (c) Saddle cation and 4-anions n.n. to v_a and v_b (at sides)
- (d) Saddle cation and 8-anions next n.n. to anions #1 and #10

(2) Cation and Cation

- (a) Saddle cation and 4-cations n.n. to anions #1 and #10 (above and below)
- (b) Saddle cation and 4-cations n.n. to anions #1 and #10 (at sides)
- (c) Saddle cation and 8-cations n.n. to anions #2, 3, 4, and 5

The extraction of two cations from normal sites effectively releases 12 cation-anion overlap interactions (i.e., between each of the cations and their six n.n. anions at a separation r_o in the unrelaxed lattice. In addition, 23 cation-cation overlap interactions are released i.e., 22 between each of the two cations and their next n.n. at a separation $\sqrt{2} r_o$ and one between the two original cations at a separation of $\sqrt{2} r_o$. These terms must be subtracted from the seven energy increasing terms outlined above.

The above described repulsive interactions may be summed as a group of explicit terms (each expressed by the appropriate overlap repulsion energy expressions as in (D59) or (D62)). This summation, with the terms written to correspond to the order presented above, is as follows:

$$\begin{aligned}
 U_R = & 2U_{BMV} \left(\frac{\sqrt{2}}{2} r_o \right) + 4U \left(\frac{\sqrt{6}}{2} r_o \right) + 4U \left(\frac{\sqrt{10}}{2} r_o \right) + 8U \left(\frac{\sqrt{14}}{2} r_o \right) \\
 & + 4U \left(\frac{\sqrt{6}}{2} r_o \right) + 4U \left(\frac{\sqrt{10}}{2} r_o \right) + 8U \left(\frac{\sqrt{14}}{2} r_o \right) \\
 & - 12U (r_o) - 23U (\sqrt{2} r_o)
 \end{aligned} \tag{D65}$$

where

$U_{B-M-V}(r)$ = Born-Mayer-Verwey expression (see equation (D62))

$U(r)$ = Born-Mayer expression (see equation (D59))

3.1.3 Summation of Contributions to the Energy of the Unrelaxed Saddle-Point Configuration

This summation is accomplished by combining Coulombic (equations (D25) and (D58)) with Non-Coulombic (equation (D65)) energy terms.

3.2 Energy Decrease Upon Relaxation ($U_2^i - U_2$)

An energy decrease occurs upon relaxation of the lattice around the saddle-point configuration. It is assumed that the lattice distorts itself in a way such that the equilibrium established by relaxation is attained by a maximum energy decrease. Evaluation of this decrease ($\Delta U^i = U_2^i - U_2$) is accomplished by a summation of relaxation-induced changes in interaction energies in the lattice. Such changes in interaction energies are considered in the order outlined below:

3.2.1 Coulomb

3.2.1.1 Monopole

- (1) Coulomb energy between nearest neighbors
- (2) Coulomb energy between saddle-point ion and the nearest neighbors
- (3) Nearest neighbor interaction with the external lattice

3.2.1.2 Polarization

- (1) Of nearest neighbors due to the effective charge on the 2 vacancies and the charge on the saddle-point ion
- (2) Of nearest neighbors due to displacement of nearest neighbors
- (3) Neglect dipole-dipole interactions

3.2.2 Non-Coulomb

- (1) Overlap interactions between saddle ion and the 10 nearest neighbor anions to the 3 defects
- (2) Overlap interactions between nearest neighbors, and between nearest neighbors and their nearest and next nearest neighbors

Note: Born-Mayer-Verwey potential used in 3.2.2 (1) and 3.2.2 (2) for all interactions where separation $\leq r_0$.

These interaction energies are expressed in terms of nearest neighbor relaxation displacements ηr_o and ξr_o shown in figure D2. A trial and error method (making use of a computer) is then used to obtain those corresponding values of ηr_o and ξr_o which maximize the relaxation-induced energy decrease. Formulation of energy terms is by procedures similar to those given earlier in sections 3.1.1 and 3.1.2.

3.2.1 Change in Coulombic Energy Contributions - ΔU_C

3.2.1.1 Monopole Interactions ($\Delta U_C'$)

These interactions may be summarized as follows:

$$\begin{aligned} \Delta U_C' = & \Delta U'_{\text{between 10-n.n. anions}} + \Delta U'_{\text{between saddle cation and 10-n.n. anions}} + \Delta U'_{\text{between anions 1 and 10 and lattice}} \\ & + \Delta U'_{\text{anions 2, 3, 4, and 5 and lattice}} + \Delta U'_{\text{anions 6, 7, 8, and 9 and lattice}} \end{aligned} \quad (D66)$$

3.2.1.1.1 $\Delta U'$ (Between 10-n. n. Anions to the Three Defects)

Inspection of figure D2 indicates that the separation r between displaced n.n. anions #1 and #10 = $\sqrt{2} r_o + 2 \sqrt{2} \xi r_o = r_o \sqrt{2} (1 + 2 \xi)$. The Coulomb interaction energy between these like charges $(-q)$ is thus:

$$(-q)(-q)/[r_o \sqrt{2} (1 + 2 \xi)] = \left(q^2 / r_o \right) \left(1 / [\sqrt{2} (1 + 2 \xi)] \right)$$

Taking into account symmetry around the saddle-point configuration, one obtains interactions between other various pairs of the 10-n.n. anions occurring at the following indicated ionic separations:

<u>No. of Interactions</u>	<u>Ionic Separation r (Units of r_o)</u>
10 (e.g., 4-5, 4-6, 2-3 etc.)	$\sqrt{2} (1 + \eta)$
2 (e.g., 6-9 etc.)	$[2 + (2 + 2\eta)^2]^{1/2}$
2 (e.g., 6-7 etc.)	$2 + 2\eta = 2 (1 + \eta)$
4 (e.g., 1-2 etc.)	$[(1 + \eta - \xi)^2 + (1 + \xi)^2]^{1/2}$

<u>No. of Interactions</u>	<u>Ionic Separation r (Units of r_o)</u>
4 (e.g., 1-3, 10-2, etc.)	$\left[(2 + \eta + \xi)^2 + \xi^2 \right]^{1/2}$
8 (e.g., 1-6, 10-8, etc.)	$\left[(1 + \xi)^2 + \xi^2 + (1 + \eta)^2 \right]^{1/2}$
2 (e.g., 2-4 etc.)	$\left[(3 + 2\eta)^2 + 1 \right]^{1/2}$
2 (e.g., 2-5 etc.)	$\sqrt{2} (2 + \eta)$
8 (e.g., 2-6, 4-8, etc.)	$\left[(2 + \eta)^2 + 1 + (1 + \eta)^2 \right]^{1/2}$

Discrete, Coulombic energy terms may be formulated for these additional 42 anion-anion monopole interactions from the potential energy expression q^2/r , as was done for the #1 - #10 interaction above. Subtraction from such terms of their counterparts appropriate to the unrelaxed saddle-point configuration (i.e., when $\eta = 0$, $\xi = 0$) yields the relaxation energy change with correct sign. This change, $\Delta U'_{10-n.n.}$ (10-n.n. anions), in which 43 interactions have been included is shown as follows:

$$\begin{aligned}
\Delta U'_{10-n.n.} = \frac{q^2}{r_o} \left\{ \frac{1}{\sqrt{2} (1 + 2\xi)} + \frac{10}{\sqrt{2} (1 + \eta)} + \frac{2}{\left[2 + (2 + 2\eta)^2 \right]^{1/2}} + \frac{2}{2 (1 + \eta)} \right. \\
+ \frac{4}{\left[(1 + \eta - \xi)^2 + (1 + \xi)^2 \right]^{1/2}} + \frac{4}{\left[(2 + \eta + \xi)^2 + \xi^2 \right]^{1/2}} \\
+ \frac{8}{\left[(1 + \xi)^2 + \xi^2 + (1 + \eta)^2 \right]^{1/2}} + \frac{2}{\left[(3 + 2\eta)^2 + 1 \right]^{1/2}} \\
+ \frac{2}{\sqrt{2} (2 + \eta)} + \frac{8}{\left[(2 + \eta)^2 + 1 + (1 + \eta)^2 \right]^{1/2}} \\
\left. - \text{appropriate terms where } \eta = 0 \text{ and } \xi = 0 \right\} \quad (D67)
\end{aligned}$$

Although some regrouping of terms in equation (D67) is desirable prior to use, the manner of expression is such as to enable easy identification.

3.2.1.1.2 $\Delta U'$ (Between Saddle Cation and 10-n.n. Anions)

In a manner similar to 3.2.1.1.1 above, one may express the 10, cation-anion interactions between the saddle cation (s) and the 10-n.n. anions to the saddle-point configuration as follows:

$$\Delta U'_{s \text{ and } 10\text{-n.n.}} = -\frac{q^2}{r_o} \left\{ \frac{2}{\sqrt{2} \left(\frac{1}{2} + \xi \right)} + \frac{4}{\left[\frac{1}{4} + \left(\frac{3}{2} + \eta \right)^2 \right]^{1/2}} + \frac{4}{\left[\frac{1}{2} + (1 + \eta)^2 \right]^{1/2}} \right. \\ \left. - \text{terms for } \eta = 0, \xi = 0 \right\} \quad (\text{D68})$$

3.2.1.1.3 $\Delta U'$ (Between n.n. Anions #1 and #10 and External Lattice)

Evaluation of interactions of the n.n. anions with the external lattice may be accomplished by first obtaining the Evjen potential V_E at the appropriate displaced position. Thus for anions #1 and #10 one determines $-V_E(\xi r_o, \xi r_o, 0)$. For anions #2 through #9, inspection of figure D2 reveals that $-V_E(\eta r_o, 0, 0)$ is the potential appropriate to the postulated displacement. Note that in either case the potentials exist at a point displaced from a normal lattice site in a perfect lattice. The negative sign is explicit and denotes dominance of the potential in this case by the adjacent anion (e.g., #1), which under the conditions for evaluating this potential remains at its normal site.

Utilization of $-V_E(\xi r_o, \xi r_o, 0)$ or $-V_E(\eta r_o, 0, 0)$ in connection with the relaxed saddle-point configuration, involving 10 displaced anions, 2 cation vacancies, and 1 saddle ion, requires that they be corrected to reflect changes introduced by these defects and relaxation displacements. The saddle ion makes no contribution to either potential and so introduces no correction.

Confining attention to $-|V_E(\xi r_o, \xi r_o, 0)|$, call $-V_E(\xi)$ for shorthand, one may proceed to describe these required corrections. For the moment call position $1'$ the unrelaxed position of anion #1 and position 1 (shown as $-\xi r_o, \xi r_o, 0$) as the relaxed position. The value of $-V_{E1}(\xi)$ reflects a strong negative contribution by anion #1 at $1'$. Moving anion #1 from $1'$ to 1 (the point at which the potential is to be evaluated) eliminates this contribution. Such elimination greatly reduces the negative value. In fact, because of previous dominance of the potential by ion #1, its removal allows the potential to become positive. This may be inferred by inspecting figure D2 and observing that cationic interactions are now dominant. This relocation (upon relaxation) of anion #1 leads to the correction:

$$- V_{E_1}(\xi) - \frac{(-q)}{r_1} = - V_{E_1}(\xi) + \frac{q}{\sqrt{2} \xi r_o}$$

The correction, involving the term $q/(\sqrt{2} \xi r_o)$, thus amounts to discounting this original contribution of anion #1 to $- V_{E_1}(\xi)$ by adding it back with sign changed. For purposes of calculation this procedure may be simulated by placing a charge of opposite sign (same magnitude) at sites where ions normally contribute to $- V_{E_1}(\xi)$. Contributions to the potential by these "equivalent charges" are then added to $- V_{E_1}(\xi)$ as correction terms.

A further example is the correction for anion #10 missing from its normal position, termed position #10'. An "equivalent charge +q" placed at 10' and separated from 1 by a distance $= r_o [\sqrt{2} \xi + \sqrt{2}]$ thus represents a correction to $V_{E_1}(\xi)$ of $+q / [\sqrt{2} (1 + \xi) r_o]$.

Upon removing a cation, e.g., cation a, the charges of six surrounding anions are partially released and one would infer that $- V_{E_1}(\xi)$ would become even more negative. The correction to $V_{E_1}(\xi)$ is obtained by placing an "equivalent charge -q" at vacancy a. At a separation $r = r_o [(1+\xi)^2 + \xi^2]^{1/2}$, the correction to $V_{E_1}(\xi)$ is thus:

$$- q / \left\{ [(1 + \xi)^2 + \xi^2]^{1/2} r_o \right\}$$

By a procedure similar to that used for the above corrections to $-V_{E_1}(\xi)$, termed for purposes of brevity 1-1', 1-10', and 1-vac.a, one may formulate corrections 1-2', 1-3', and 1-6'. Based on the symmetry of a FCC lattice, these correction terms to be added to $- V_{E_1}(\xi)$ may be grouped as follows:

<u>Source</u>	<u>Correction Term</u>
1 - 1'	$\frac{q}{r_o \sqrt{2} \xi}$
1 - 10'	$\frac{q}{r_o \sqrt{2} (1 + \xi)}$
$\left\{ \begin{array}{l} 1 - \text{vac. a} \\ 1 - \text{vac. b} \end{array} \right\}$	$\frac{- q}{r_o [(1 + \xi)^2 + \xi^2]^{1/2}}$

<u>Source</u>	<u>Correction Term</u>
$\begin{Bmatrix} 1 - 2' \\ 1 - 5' \end{Bmatrix}$	$\frac{q}{r_o \left[(1 - \xi)^2 + (1 + \xi)^2 \right]^{1/2}}$
$\begin{Bmatrix} 1 - 3' \\ 1 - 4' \end{Bmatrix}$	$\frac{q}{r_o \left[(2 + \xi)^2 + \xi^2 \right]^{1/2}}$
$\begin{Bmatrix} 1 - 6', 1 - 7' \\ 1 - 8', 1 - 9' \end{Bmatrix}$	$\frac{q}{r_o \left[(1 + \xi)^2 + \xi^2 + 1 \right]^{1/2}}$

The above tabulation thus accounts for the effect on $-V_{E_1}(\xi)$ of all 10-n.n. anions missing from normal sites and the two cation vacancies. Applying these corrections leads to the following expression for the potential at position 1:

$$\begin{aligned}
 V_1(\xi) = - \left[V_{E_1}(\xi) \right] + \frac{q}{\sqrt{2} \xi r_o} + \frac{q}{\sqrt{2} (1+\xi) r_o} - \frac{2q}{\left[(1+\xi)^2 + \xi^2 \right]^{1/2} r_o} + \frac{2q}{\left[(1-\xi)^2 + (1+\xi)^2 \right]^{1/2} r_o} \\
 + \frac{2q}{\left[(2+\xi)^2 + \xi^2 \right]^{1/2} r_o} + \frac{4q}{\left[(1+\xi)^2 + \xi^2 + 1 \right]^{1/2} r_o} \quad (D69)
 \end{aligned}$$

The energy of interaction of anion #1 with the external lattice is given by the product of its charge $(-q)$ and the potential at position 1. The latter, of course, is given by equation (D69). Note also that, because of symmetry, the corrected potential at position 10 is identical with that at position 1. The energy of interaction $\Delta U'$ (between n.n. anions #1 and #10 and the external lattice) is thus given as follows:

$$\Delta U'_{\text{anions 1 and 10 and lattice}} = 2 (-q) \cdot V_1(\xi)$$

$$= -2 \frac{q^2}{r_o} \left\{ - \left| V_{E_1}(\xi r_o, \xi r_o, 0) \right| \frac{r_o}{|q|} + \frac{1}{\sqrt{2} \xi} + \frac{1}{\sqrt{2} (1+\xi)} \right. \\ - \frac{2}{\left[(1+\xi)^2 + \xi^2 \right]^{1/2}} + \frac{2}{\left[(1-\xi)^2 + (1+\xi)^2 \right]^{1/2}} \\ + \frac{2}{\left[(2+\xi)^2 + \xi^2 \right]^{1/2}} + \frac{4}{\left[(1+\xi)^2 + \xi^2 + 1 \right]^{1/2}} \\ \left. - \left[\text{terms where } \xi = 0 \right] \right\} \quad (D-70)$$

3.2.1.1.4 $\Delta U'$ (Between n.n. Anions #2, 3, 4, and 5 and External Lattice)

Reference to figure D2 reveals that anions #2, #3, #4, and #5 undergo identical interaction with the lattice. Proceeding as in 3.2.1.1.3, corrections to the Evjen potential at any one of these four displaced positions (e.g., position 2) are formulated to yield the potential existing after relaxation about a saddle-point configuration. Multiplication of this potential, for example $V_2(\eta r_o, 0, 0)$, by the charge $(-q)$ on anion #2 and finally by the factor four (to account for the four symmetrical anions mentioned above) yields the following expression for the interaction energy between these ions and the external lattice:

$$\begin{aligned}
\Delta U'_{\text{anions 2, 3, 4, and 5 and lattice}} = & -4 \frac{q^2}{r_o} \left\{ - \left| V_{E_2}(\eta r_o, 0, 0) \right| \frac{r_o}{|q|} + \frac{1}{\eta} + \frac{4}{[1 + (1+\eta)^2]^{1/2}} - \frac{1}{1+\eta} \right. \\
& - \frac{1}{[(2+\eta)^2 + 1]^{1/2}} + \frac{2}{[(2+\eta)^2 + 2]^{1/2}} + \frac{1}{[(2+\eta)^2 + 4]^{1/2}} \\
& + \frac{1}{[(3+\eta)^2 + 1]^{1/2}} + \frac{1}{2+\eta} \\
& \left. - [\text{terms where } \eta = 0] \right\} \quad (D71)
\end{aligned}$$

3.2.1.1.5 $\Delta U'$ (Between n.n. Anions #6, 7, 8, and 9 and External Lattice

Again using procedures shown in 3.2.1.1.3 and noting the symmetry of anions 6, 7, 8, and 9 with respect to the defect structure, one may formulate an interaction energy expression between these four anions and the external lattice as follows:

$$\begin{aligned}
\Delta U'_{\text{anions 6, 7, 8, and 9 and lattice}} = & -4 \frac{q^2}{r_o} \left\{ - \left| V_{E_6}(\eta r_o, 0, 0) \right| \frac{r_o}{|q|} + \frac{1}{\eta} - \frac{1}{1+\eta} - \frac{1}{[(1+\eta)^2 + 2]^{1/2}} \right. \\
& + \frac{4}{[(1+\eta)^2 + 1]^{1/2}} + \frac{2}{[(1+\eta)^2 + 5]^{1/2}} + \frac{1}{2+\eta} \\
& \left. + \frac{1}{[(2+\eta)^2 + 2]^{1/2}} + \frac{1}{(2+\eta)^2} - [\text{terms where } \eta = 0] \right\} \quad (D72)
\end{aligned}$$

3.2.1.1.6 Evaluation of ΔU_C^1

The monopole interaction terms, evaluated separately in equations (D67), (D68), (D70), (D71), and (D72), may be summed according to equation (D66) to yield the decrease in monopole interaction energy resulting from n.n. relaxation about the saddle-point configuration.

3.2.1.2 Polarization (ΔU_P^1)

It will be recalled that, to minimize complexity, polarization of the external lattice is not considered relaxable. Thus only the decrease in polarization energy of the 10-n.n. anions is considered. Referring back to section 3.1.1.2.1 (polarization of the n.n. anions in the unrelaxed configuration), please note equations (D31). For the relaxed condition of anion #1 one may revise these as follows:

$$\left. \begin{aligned} \omega &= \theta = \pi/4 \\ r_a &= r_b = r_o \left[(1 + \xi)^2 + \xi^2 \right]^{1/2} \\ r_s &= r_o \sqrt{2} [1/2 + \xi] \\ q_s &= q_a = q_b = q \text{ (where } z_{\text{cation}} = z_{\text{anion}}) \end{aligned} \right\} \quad (D73)$$

Equation (D30) may be revised to yield the sum of the x-components of the electric fields induced at position 1 by the three defects as follows:

$$\Sigma E_x = -\frac{q_s}{r_s} \frac{\cos \theta}{2} E_{s-(E)} + \frac{q_a}{r_s} \frac{\cos \theta}{2} E_{a-(E)} + \frac{q_b}{r_b} \frac{\cos \theta}{2} E_{b-(E)}$$

$$= -\frac{q}{\left\{ r_o \sqrt{2} \left[\frac{1}{2} + \xi \right] \right\}^2} \cdot \frac{1}{\sqrt{2}} + \frac{q}{\left\{ r_o \left[(1+\xi)^2 + \xi^2 \right]^{1/2} \right\}^2} \cdot \frac{(1+\xi)}{\left[(1+\xi)^2 + \xi^2 \right]^{1/2}}$$

$$+ \frac{q}{\left\{ r_o \left[(1+\xi)^2 + \xi^2 \right]^{1/2} \right\}^2} \cdot \frac{\xi}{\left[(1+\xi)^2 + \xi^2 \right]^{1/2}}$$

$$= \frac{q}{2} \frac{1}{r_o} \left\{ -\frac{1}{2\sqrt{2} (1/2+\xi)^2} + \frac{1+\xi}{\left[(1+\xi)^2 + \xi^2 \right]^{3/2}} + \frac{\xi}{\left[(1+\xi)^2 + \xi^2 \right]^{3/2}} \right\}$$

$$\Sigma E_x = \frac{q}{2} \frac{1}{r_o} \left\{ -\frac{\sqrt{2}}{4(1/2+\xi)^2} + \frac{1+2\xi}{\left[(1+\xi)^2 + \xi^2 \right]^{3/2}} \right\} \quad (D74)$$

This value of ΣE_x may be substituted in equation (D36) to yield the explicit polarization interaction energy term U_P for anion #1 in its displaced position $\xi r_o, \xi r_o, 0$. Since anion #1 and #10 are equivalent in their interactions with the defect fields we may write the following expression for $\Delta U_P'$:

$$\begin{aligned}
 (\Delta U_P')_{\substack{\text{n.n.anions} \\ \#1 \text{ and } \#10}} &= 2 \left[-\frac{1}{2} \alpha_- \left(2 \Sigma E_x^2 \right) \right] \\
 &= -2 \alpha_- \frac{q^2}{r_o^4} \left\{ \frac{\sqrt{2}}{4 (1/2 + \xi)^2} - \frac{1 + 2\xi}{[(1+\xi)^2 + \xi^2]^{3/2}} \right. \\
 &\quad \left. - \left[\text{terms where } \xi = 0 \right] \right\}^2 \tag{D75}
 \end{aligned}$$

Note that the sign change of the first two terms within curly brackets in (D75) is permitted by virtue of the bracket being raised to the power two.

Similar procedures may be used to derive expressions for the group of equivalent anions #2, 3, 4, and 5 and for the remaining group consisting of anions #6, 7, 8, and 9. The following expressions result:

$$\begin{aligned}
 (\Delta U_P')_{\substack{\text{n.n.anions} \\ \#2, 3, 4 \text{ and} \\ 5}} &= -2 \alpha_- \frac{q^2}{r_o^4} \left\{ \left[\frac{1/2}{[(3/2 + \eta)^2 + 1/4]^{3/2}} - \frac{1}{[(2 + \eta)^2 + 1]^{1/2}} \right]^2 \right. \\
 &\quad + \left[\frac{3/2 + \eta}{[(3/2 + \eta)^2 + 1/4]^{3/2}} - \frac{1}{(1 + \eta)^2} - \frac{2 + \eta}{[(2 + \eta)^2 + 1]^{3/2}} \right]^2 \\
 &\quad \left. - \left[\text{terms where } \eta = 0 \right] \right\} \tag{D76}
 \end{aligned}$$

$$\begin{aligned}
(\Delta U'_P)_{\substack{\text{n.n. anions} \\ \#6, 7, 8, \\ \text{and } 9}} = & -2 \alpha - \frac{q^2}{r_o^4} \left\{ 2 \left[\frac{1/2}{[1/2 + (1+\eta)^2]^{3/2}} - \frac{1}{[2 + (1+\eta)^2]^{3/2}} \right]^2 \right. \\
& + \left[\frac{1}{(1+\eta)^2} - \frac{1+\eta}{[1/2 + (1+\eta)^2]^{3/2}} + \frac{1+\eta}{[2 + (1+\eta)^2]^{3/2}} \right]^2 \\
& \left. - [\text{terms where } \eta = 0] \right\} \quad (D77)
\end{aligned}$$

Summation of equations (D75), (D76), and (D77) yields the net change in polarization energy $\Delta U'_P$ resulting from relaxation of all 10-n.n. anions about the saddle-point defect configuration.

3.2.1.3 Summation to Yield ΔU_C

The change in Coulombic energy resulting from relaxation about the saddle-point configuration is obtained by adding the monopole interactions (section 3.2.1.1) with the dipole-defect interactions (section 3.2.1.2) as follows:

$$\Delta U_C = \Sigma U' \text{ (monopole)} + \Sigma U'_P \quad (D78)$$

Note: Dipole-dipole interactions were neglected.

3.2.2 Decrease in Non-Coulombic Energy (ΔU_R)

Similar procedures are used here to evaluate the decrease in overlap repulsive interaction energy as were discussed in section 3.1.2. The B-M expression (designated $U(r)$; see equation (D59)) is used where $r \geq r_o$ and the B-M-V expression (designated $U_{BMV}(r)$; see Equation (D62)) where $r < r_o$.

3.2.2.1 Overlap Interactions Between Saddle Ion and 10-n.n.'s (Cation-Anion)

The terms dominating ΔU_R are those two (identical) expressions describing the overlap repulsion between the saddle ion(s) and anion #1 and anion #10, respectively. At a relaxed separation $r = (\sqrt{2}/2 + \sqrt{2} \xi) r_o$, repulsion interaction s-1 may be expressed as follows:

$$U_R(s-1) = U_{BMV_{+-}} \left[\left(\sqrt{2}/2 + \sqrt{2} \xi \right) r_o \right] \quad (D79)$$

Since interactions s-1 and s-10 are the same we have:

$$U_R(s-1, s-10) = 2 U_{BMV_{+-}} \left[\left(\sqrt{2}/2 + \sqrt{2} \xi \right) r_o \right] \quad (D80)$$

Similarly overlap interactions s-2, s-3, s-4, and s-5 may be expressed by:

$$U_R(s-2 \text{ through } s-5) = 4 U_{+-} \left\{ \left[(3/2+\eta)^2 + 1/4 \right]^{1/2} r_o \right\} \quad (D81)$$

and interactions s-6 through s-9 by the following expression:

$$U_R(s-6 \text{ through } s-9) = 4 U_{+-} \left\{ \left[(1+\eta)^2 + 1/2 \right]^{1/2} r_o \right\} \quad (D82)$$

Summation of the above overlap interactions of the saddle ion with each of the 10-n.n.s and comparison of this sum with that obtained from the appropriate terms when $\eta = 0$, $\xi = 0$ yields:

$$\begin{aligned} \Delta U_R(s \text{ and } 10\text{-n.n.}) = & 2 U_{BMV_{+-}} \left[\left(\sqrt{2}/2 + \sqrt{2} \xi \right) r_o \right] + 4 U_{+-} \left\{ \left[(3/2+\eta)^2 + 1/4 \right]^{1/2} r_o \right\} \\ & + 4 U_{+-} \left\{ \left[(1+\eta)^2 + 1/2 \right]^{1/2} r_o \right\} \\ & - \left[\text{terms where } \xi = 0, \eta = 0 \right] \end{aligned} \quad (D83)$$

3.2.2.2 Overlap Interactions Involving n.n. Anions #1 and #10

Inspection of figure D2 reveals four cations in a nearest neighbor position with respect to anion #1 (two in the plane of the paper, one above and one below), the saddle ion being excluded. A similar relationship prevails at anion #10. The two cations in the plane of the paper are separated from anion #1 by a distance $r = [\xi^2 + (1-\xi)^2]^{1/2} r_o$. The two cations out of the plane of the paper are separated by a distance $r = [2\xi^2 + 1]^{1/2} r_o$. Anion-cation, overlap repulsion for these important interactions (i.e., where $r \leq r_o$) may thus be expressed by the following:

$$U_R(\#1-, \#10\text{-four cation n.n.}) = 4 U_{BMV_{-+}} \left\{ \left[\xi^2 + (1-\xi)^2 \right]^{1/2} r_o \right\} \\ + 4 U_{-+} \left\{ \left[2 \xi^2 + 1 \right]^{1/2} r_o \right\} \quad (D84)$$

Similarly, a single anion will be noted in the plane of the paper located at a next nearest neighbor position with respect to anion #1. Their separation $r = \sqrt{2} (1 - \xi) r_o$. A like geometry prevails for anion #10. Thus we may write the following overlap repulsion term:

$$U_R(\#1-, \#10\text{-one anion next n.n.}) = 2 U_{--} \left[\sqrt{2} (1 - \xi) r_o \right] \quad (D85)$$

Overlap interactions between anions #1 and #10 and the other eight, numbered n.n.'s to the three defects may be expressed as follows:

Anion-Anion Interactants	Overlap Repulsion Energy
1-2, 1-5, 10-3, 10-4	$4 U_{--} \left\{ \left[(1+\xi)^2 + (1+\eta-\xi)^2 \right]^{1/2} r_o \right\}$

(D86)

$\left\{ \begin{array}{l} 1-6, 1-7, 1-8, 1-9 \\ 10-6, 10-7, 10-8, 10-9 \end{array} \right\}$	$8 U_{--} \left\{ \left[\xi^2 + (1+\xi)^2 + (1+\eta)^2 \right]^{1/2} r_o \right\}$
--	---

(D87)

Additionally, an anion-anion interaction term may be written to describe the overlap repulsion between anions #1 and #10 and each of their four, next nearest neighbor anions (out of the plane of the paper). An anion-cation interaction term may also be written for anions #1 and #10 interacting with each of their two, third-nearest-neighbor cations. A total of 12 additional interaction terms involving anions #1 and #10 is thus generated.

Overlap interactions involving anions #1 and #10 thus total 34 and consist of 22 anion-anion and 12 anion-cation interactions. The decrease in energy, upon relaxation, related to these may be expressed as follows:

$$\begin{aligned}
\Delta U_R(\text{n.n.}\#1-, 10-) &= (\text{eq. (D84)}) + (\text{eq. (D85)}) + (\text{eq. (D86)}) + (\text{eq. (D87)}) \\
&+ 8 U_{--} \left\{ \left[(1-\xi)^2 + \xi^2 + 1 \right]^{1/2} r_o \right\} \\
&+ 4 U_{-+} \left\{ \left[1 + 2 (1-\xi)^2 \right]^{1/2} r_o \right\} \\
&- [\text{terms where } \xi = 0, \eta = 0]
\end{aligned} \tag{D88}$$

3.2.2.3 Overlap Interactions Involving n.n. Anions #2 Through #9

Referring to figure D2, an important term is the one describing interaction between each of the eight unaccounted for "n.n." anions (#2 through #9) and one adjoining cation at $r = (1-\eta) r_o$. Four other cations adjoin each of these eight, numbered anions at a separation $r = (1+\eta^2)^{1/2} r_o$. These 40, anion-cation overlap interactions may be expressed as follows:

$$U_R(\text{n.n.2-9})_{-+} = 8 U_{BMV_{-+}} \left[(1-\eta) r_o \right] + 32 U_{-+} \left[(1+\eta^2)^{1/2} r_o \right] \tag{D89}$$

Again referring to figure D2, one observes ten interactions (2-3, 2-8, 2-9, 3-8, 3-9, 4-5, 4-6, 4-7, 5-6, and 5-7) between these eight numbered anions at the separation of next nearest neighbors. Since such separation $r > r_o$, these interactions are obtained from the B-M expression as follows:

$$\Delta U_R(\text{n.n.2-9})_{--} = 10 U_{--} \left[\sqrt{2} (1+\eta) r_o \right] \tag{D90}$$

In addition to the above 50 interactions, 60 more anion-anion terms are pertinent. These involve interactions of anions #2 through #9 with their next nearest neighbor anions. Summing then, one obtains the following:

$$\begin{aligned}
\Delta U_R(n.n.2-9) = & 8 U_{BMV_{-+}} \left[(1-\eta) r_o \right] + 32 U_{-+} \left[(1+\eta^2)^{1/2} r_o \right] + 10 U_{--} \left[\sqrt{2} (1+\eta) r_o \right] \\
& + 32 U_{--} \left\{ \left[1 + (1-\eta)^2 \right]^{1/2} r_o \right\} + 28 U_{--} \left[(2+\eta^2)^{1/2} r_o \right] \\
& - [\text{terms where } \eta = 0]
\end{aligned} \tag{D91}$$

3.2.2.4 Evaluation of ΔU_R

The total decrease in overlap repulsion upon relaxation is obtained by simply adding the interaction expressions (D83), (D88), and (D91). Note that 154 overlap repulsion interaction terms have been included.

3.2.3 Net Energy Decrease Upon Relaxation

The evaluation of the energy decrease upon relaxation ($U_2' - U_2$) detailed above is based on the model (figure D2) that the 10 anions nearest neighbors (numbered) to the three-defect saddle-point configuration undergo relaxation displacement ξr_o and ηr_o as shown. An expression for this energy decrease in terms of ξ and η may be formulated by adding the Coulombic (equation (D78)) and non-Coulombic (equations (D83), (D88), and (D91)) contributions. A trial and error process may be used to maximum the decrease, $U_2' - U_2$. Thus one selects a value of η (the least sensitive of the two unknowns) and scans the summation equation by varying ξ . Successive selection soon yields a pair of values for η and ξ which correspond to a maximum decrease in energy. Such displacement, of course, represents a minimum energy for the distorted saddle-point configuration, the condition for stability.

3.3 Energy of the Relaxed Configuration (U_2)

Subtraction of the equilibrium decrease in energy $U_2' - U_2$ (section 3.2.3) upon relaxation from the energy of the unrelaxed cationic saddle-point configuration U_2' yields the value for the energy of the relaxed configuration U_2 . The value of U_2 in the illustrated calculations above, of course, corresponds to a cation in the saddle-point position. In this simplified case this saddle ion is assumed to lie in the same plane as two nearest neighbor cation vacancies, each a distance of $r_o \sqrt{2}/2$ away from the saddle-ion.

4.0 Energy Barrier for Cation Vacancy Migration (ΔU_r) in an Otherwise Perfect Lattice

It has been demonstrated that the saddle-point energy represents the largest barrier to ion migration. Evaluation of this barrier proceeds now based on the foregoing discussion. For example, take the case of a cation at a normal lattice site $0,0,0$ and a cation vacancy at $1,1,0$, both in an otherwise perfect lattice. The energy of this configuration is U_1 . In attempting to jump to $1,1,0$, the cation at $0,0,0$ must overcome the energy barrier at the saddle position, approximated by $1/2, 1/2, 0$. The energy of this configuration is U_2 . The net energy barrier for cation migration is thus $U_2 - U_1 = \Delta U_r$. Upon satisfying this requirement, the cation may jump over this barrier to fill the vacancy at $1,1,0$. Correspondingly, the vacancy appears to migrate from $1,1,0$ to $0,0,0$.

REFERENCES

1. Ewald, P. P., "The Calculation of Optical and Electrostatic Lattice Potential," *Ann. Physik.* 64, 253 (1921).
2. Evjen, H. M., "On the Stability of Certain Heteropolar Crystals," *Phys. Rev.* 39, 675 (1932).
3. Mott, N. F., and Littleton, M. J., "Conduction in Polar Crystals," *Trans. Faraday Soc.* 34, 485-499 (1938).
4. Guccione, R., Tosi, M. P., and Asdente, M., "Migration Barriers for Cations and Anions in Alkali Halide Crystals," *J. Phys. Chem. Solids* 10, 162-168 (1959).
5. Tosi, M. P., and Fumi, F. G., "The Interaction Between Equilibrium Defects in the Alkali Halides: The Ground State Binding Energy of the Vacancy Pair," *Nuovo Cimento (Series 10)* 7 (No. 1), 95-106 (1958).
6. Bassani, F., and Fumi, F. G., "The Interaction Between Equilibrium Defects in the Alkali Halides: The Ground State Binding Energies Between Divalent Impurities and Vacancies," *Nuovo Cimento (Series 9)* 11 (No. 3), 274-284 (1954).
7. Fumi, F. G. and Tosi, M. P., "Lattice Calculations on Point Imperfections in the Alkali Halides," *Faraday Soc. Discussions* 23, 92-8 (1957).
8. Tosi, M. P., and Doyama, M., "Vacancies and Monovalent Cation Impurities in the Alkali Halides," *Phys. Rev.* 151, 642-8 (1966).
9. Jones, J. E., and Ingham, A. E., "On the Calculation of Certain Crystal Potential Constants and On the Cubic Crystal of Least Potential Energy," *Proc. Royal Soc. Series A107*, 638-40 (1925).
10. Tessman, J. R., Kahn, A. H., and Shockley, W., "Electronic Polarizabilities of Ions in Crystals," *Phys. Rev.* 92, 890-5 (1953).

APPENDIX E

APPROXIMATE SCATTERING RANGE OF SOLAR UV PHOTONS

Attempts to use single particle optical scattering theory, e.g., Mie theory for spherical particles, to predict energy attenuation by scattering in concentrated particulate systems involving multiple scattering have had only limited success. Particle proximity, size distribution effects, and difficulty in defining optical path lengths to be associated with theoretically estimated extinction coefficients constitute three major problems. In an effort to obtain a reasonable estimate of the projected ("straight through") range of a near-UV photon in a compressed pigment powder or a pigmented coating prior to degradation, experimental data has been used.

It is assumed that in pigments of interest the intrinsic photon absorption edge occurs at an energy greater than 6.2 eV. Photon energies of the solar emissions spectrum will be considered as largely ≤ 6.2 eV. The UV "scattering range" will be considered on the basis of the 4.1 eV photon (wavelength in vacuum, $\lambda_{vac} = 0.3\mu$) as the least energetic photon likely to significantly influence exciton generation rates.

The fractional decrease in spectral radiation intensity, from an incident $I_0(\lambda)$ value to $I_x(\lambda)$, after a beam has traversed an actual optical path x is explicitly expressed as follows:

$$I_x(\lambda)/I_0(\lambda) = \exp \left[-x (\sigma_a + \sigma_s) N \right] \quad (E1)$$

where

σ_a = absorption cross-section, cm^2

σ_s = scattering cross-section, cm^2

N = number of scattering and absorbing centers/ cm^3

$S = N (\sigma_a + \sigma_s)$ = discrete extinction coefficient in reciprocal units of actual path, cm^{-1}

While not required in single particle scattering, for the case of interest, namely multiple scattering of "spherical" particles in close proximity, careful distinction between the actual optical path x and the projected path ℓ (i. e., measured normal to the surface) must be made. For a given, uniform particulate dispersion equation (E1) may be approximated by use of a superficial extinction coefficient S' as follows:

$$(I_\ell/I_0)_\lambda \approx \exp [-S' \ell] \quad (E2)$$

The diffuse spectral transmission of a 5.5 mil (0.0139 cm) thick coating prepared by IITRI was measured by Blair¹ (see figure E1). This coating contained ~30 percent volume ZnO pigment particles (average 0.3 μ diameter, type SP-500) treated with K₂SiO₃ and dispersed in a catalyzed, polydimethylsiloxane binder (index of refraction = 1.4). These data demonstrate wavelength-dependent radiant energy attenuation typical of what van de Hulst² called the anomalous diffraction domain. By using only those data well away from the absorption edge, S' values were obtained from equation (2) and extrapolated to $\lambda = 0.21\mu$ ($\lambda_{vac} = 0.3\mu$). For example at $\lambda_{vac} = 0.5\mu$:

$$\lambda \text{ (in silicone medium)} = 0.5\mu / 1.4 = 0.358\mu$$

Taking the \ln of equation (E2) yields:

$$\ln(I_o/I)_\lambda = S' \ell \quad (E3)$$

Neglecting all interface reflectance and taking $I_o = 1.00$ yields:

$$\ln(1.00/0.04) = (1.39 \times 10^{-2} \text{ cm}) S'$$

$$S' = 3.22 / (1.39 \times 10^{-2}) = 230 \text{ cm}^{-1}$$

At $\lambda_{vac} = 0.3\mu$ ($\lambda_{med} = 0.214\mu$), an extrapolated S' value of 400 cm^{-1} is obtained (figure E2). Equation (E3) indicates that at this superficial extinction, 90 percent attenuation of this wavelength would occur in a coating thickness of 58 μ for a coating having similar (a) geometry, (b) particle and medium indexes of refraction and (c) absorption characteristics.

Transmission of visible radiation through compressed and fired polycrystalline Al₂O₃ of varying pore size and porosity is presented by Lee and Kingery.³ These data indicate correlation of scattering coefficients of pores in a medium of alumina as a function of wavelength, pore size, and porosity. Thus in a compact containing a fairly uniform pore radius of 2 μ and 3 percent porosity, a "scattering coefficient" of ~185 cm^{-1} is measured at an extrapolated wavelength of $\lambda_{vac} = 0.3\mu$ ($\lambda_{Al_2O_3} = 0.165\mu$). Transmission measurements indicate that this ~185 cm^{-1} value can be considered equivalent to the superficial extinction coefficient S' considered earlier. On this basis, equation (E3) indicates that 90 percent attenuation of incident, 0.3 μ radiation should occur in a thickness of 125 μ of 3 percent porosity Al₂O₃ containing 2 μ radius pores. Similar attenuation at $\lambda_{vac} = 0.3\mu$ in a 0.25 percent porosity Al₂O₃ containing 0.7 μ radius pores is indicated to occur within a thickness of 230 μ .

Based on the above data, it is concluded that prior to degradation (either UV- or proton-induced) the projected range for UV photons of interest is an order of 100 μ in either pigment-scattering (conventional

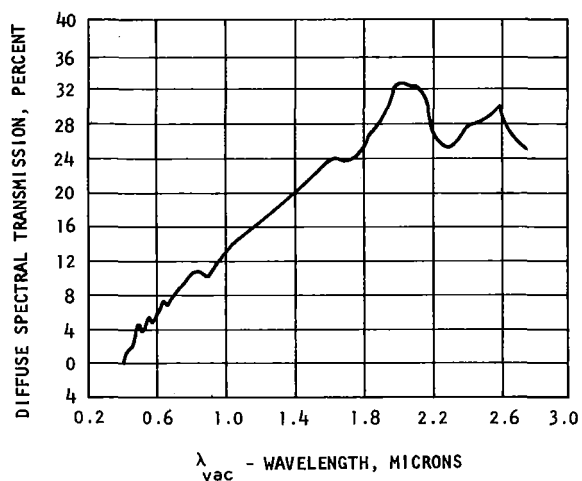


Figure E1. The diffuse spectral transmission of potassium silicate treated zinc oxide-silicone coating (5.5 mils thick).

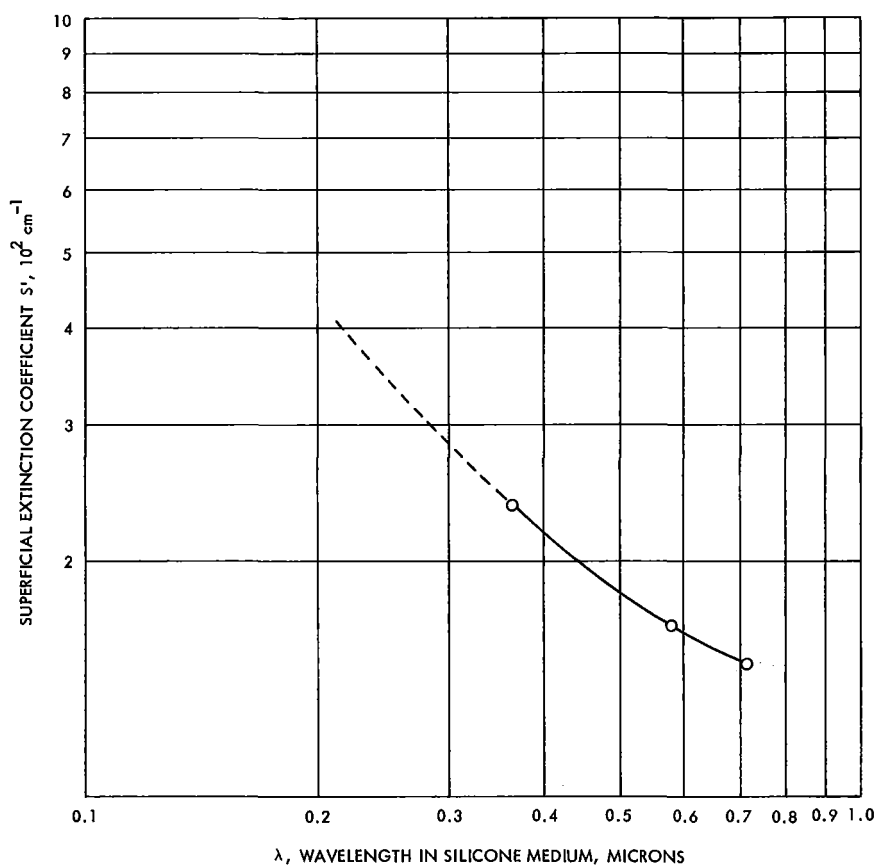


Figure E2. Superficial spectral extinction for K_2SiO_3 -treated ZnO pigment particles (0.3μ diameter) dispersed at ~ 30 percent volume concentration in silicone binder.

pigment content) or void-scattering (pigmentation exceeds CPVC) systems. While admittedly an estimate, this UV range appears sufficiently accurate for present purposes.

REFERENCES

1. Blair, P.M., Jr., "In Situ Evaluation of Several Thermal Control Coatings," Hughes Aircraft Tech. Rept. P67-226, p. 20 (1967) .
2. van de Hulst, H. C. , Light Scattering by Small Particles, John Wiley & Sons, New York, pp. 128-130, 145, 151, 177-8 (1957).
3. Lee, D.W., and Kingery, W.D., "Radiation Energy Transfer and Thermal Conductivity of Ceramic Oxides," J. Am. Ceram. Soc. 43, 598, 600-2 (1960).

